Indra Noer Hamdhan

A Contribution to Slope Stability Analysis with the Finite Element Method

Dissertation

Eingereicht an der Fakultät für Bauingenieurwissenschaften
der Technischen Universität Graz

Begutachter:

Ao.Univ.-Prof. Dipl.-Ing. Dr.techn. Helmut F. Schweiger, M.Sc.
Institute for Soil Mechanics and Foundation Engineering
Graz University of Technology, Austria

Prof. Ir. Masyhur Irsyam, MSE, Ph.D
Departement of Civil Engineering
Bandung Institute of Technology, Indonesia

Graz, June 2012

Acknowledgements

The work presented in this dissertation has been carried out at the Computational Geotechnics Group, Institute for Soil Mechanics and Foundation Engineering in Graz University of Technology under the supervision of Ao.Univ.-Prof. Dipl.-Ing. Dr.techn. Helmut F. Schweiger as the main adviser. I am very grateful to his valuable guidance, discussions and encouragement throughout the study period. All kinds of contributions from him for this study area highly appreciated. Appreciation by words is not sufficient to him who not only encouraged to apply, but also made the study successfully complete.

Appreciation is also due to Univ.-Prof. Dipl.-Ing. Dr.techn. Roman Marte and Em.Univ.-Prof. Dipl.-Ing. Dr.techn. Stephan Semprich, former head of the Institute for Soil Mechanics and Foundation Engineering for making the research facilities of the Institute available to me. I would also like to thank Prof. Ir. Masyhur Irsyam, MSE, Ph.D from the Bandung Institut of Technology (ITB), for reviewing my dissertation.

This study was made possible by the scholarship grant from Directorate General of Higher Education, Ministry of National Education, Republic of Indonesia. A special appreciation goes to Bandung National Institute of Technology (Itenas) and Kopertis IV that supported me to study abroad.

I appreciate the contribution of many of my colleagues especially Ikhya, Franz Tschuchnigg, Bert Schädlich, Dr.techn. Vahid Galavi, Laurentiu Floroiu, Christian Lackner, Gregor Supp, and Viet Nguyen, I enjoyed joining you in such a warm research atmosphere.

I would like to thank my parents for their prayers throughout my life. I would also like to thank my brothers, my sisters, Itenas and IndoGraz colleagues for their support during my study.

Finally, I would like to thank my lovely wife, Venny for her encouragement for the study. Her patience and hardship of taking home responsibility are highly appreciable. Similarly, my sons, Nadhif and Hisyam and my daughter, Shafira are acknowledged for their good understanding about their father's absence and late arrival home.

Graz, June 2012 Indra Noer Hamdhan

Kurzfassung

Ein Beitrag zur Standsicherheitsberechnung von Böschungen mit der Finite Elemente Methode

Das Hauptziel von Böschungsbruchberechnungen ist der Entwurf sicherer und wirtschaftlicher Böschungsbauwerke sowie die Einschätzung der Standsicherheit natürlicher Hänge. Dazu ist es erforderlich, mögliche Versagensmechanismen zu erfassen, die kurz- und langfristige Standsicherheit einzuschätzen sowie den potentiell destabilisierenden Einfluss von Umweltfaktoren zu berücksichtigen.

Die zur Verfügung stehenden Berechnungsmethoden variieren in den zugrunde liegenden theoretischen Annahmen, wodurch sich zwangsläufig eine Variation der Berechnungsergebnisse in Abhängigkeit von der verwendeten Methode ergibt. Das verwendete Berechnungsverfahren sollte daher in der Lage sein, die tatsächlichen Vorgänge innerhalb des Böschungskörpers möglichst realistisch abzubilden. In dieser Arbeit wird hierfür die Finite Elemente Methode verwendet, mit welcher undrainiertes Materialverhalten, Reduzierung der Scherfestigkeit mit akkumulierten Dehnungen, Teilsättigung und die Prozesse bei rascher Absenkung des Wasserspiegels abgebildet werden können. Die Finite Elemente Methode hat sich als praktikables Werkzeug für die Durchführung von Böschungsbruchberechnungen etabliert. Im Gegensatz zu anderen Verfahren wird mit dieser Berechnungsmethode der Versagensmechanismus als Ergebnis der Berechnung erhalten und muss nicht vom Anwender vorgegeben werden.

In dieser Arbeit werden drei verschiedene Ansätze zur Abbildung von undrainiertem Materialverhalten in Berechnungen mit effektiven und totalen Spannungen verwendet. Weiterhin werden die Ergebnisse von numerischen Berechnungen unter Berücksichtigung einer kontinuierlichen Materialentfestigung mit den Ergebnissen bei abrupter Reduzierung der Scherfestigkeit verglichen. Diese Berechnungen wurden mit einem einfachen Mohr-Coulomb Stoffgesetz und einem komplexen Multilaminaten Stoffgesetz durchgeführt.

Für die numerische Simulation eines Hanges mit teilgesättigten Bodenverhältnissen bei Beregnung und Grundwasserabsenkung wird die Verformungsberechnung vollständig mit einer instationären Strömungsberechnung gekoppelt. Der Einfluss der hydraulischen Bodeneigenschaften auf das Verhalten des Hanges wird mit dieser Vorgehensweise berücksichtigt.

Abstract

A Contribution to Slope Stability Analysis with the Finite Element Method

From a practical point of view, the main aim of slope stability analysis is to contribute to the safe and economic design of an engineered slope or natural slopes. Generally, the objectives of slope stability analysis are to investigate the potential of failure mechanism, to assess the stability under short-term and long-term conditions, and to analyze the influence of environmental factors that caused instability of the slope.

Slope stability methods vary in their theoretical background and approach and hence the analysis results vary depending on the used theory. Therefore, the chosen method should be able to identify the real condition of stability of the slope. In this study, slope stability analysis with the finite element method is used, in which undrained behaviour, strain softening behaviour, unsaturated soil behaviour and drawdown conditions have been implemented. The finite element method is a powerfull method for slope stability analysis, which computes failure mechanisms in contrary to limit equilibrium methods, where the shape of the failure mechanism has to be assumed a priori.

Different methods of modelling undrained behavior in slope stability analysis, namely in terms of effective stresses and total stresses are implemented in this study respectively.

Slope stability analysis wih strain softening behaviour and their comparison with the strength reduction approach are presented in this study. The analysis was done using a simple Mohr Coulomb model and an advanced Multilaminate model.

The fully coupled flow-deformation analysis with the finite element method are implemented in the analysis of an unsaturated soil slope with rainfall condition and with water drawdown conditions. The effect of hydraulic characteristics of soils are evaluated to analysis the factor of safety under these conditions.

.

Table of contents

List of symbols and abbreviations

This section lists the definition of used symbols in alphabetical order. They are additionally explained in the text when they first appear. Units are not included in this lists, they will be defined in the text when they are first used.

Small letters

c	cohesion
c'	effective cohesion
c_u	undrained cohesion
c'_{mob}	mobilized effective cohesion
c'_{peak}	effective cohesion at peak strength
c'_{res}	effective cohesion at residual strength
f	yield function
g	plastic potential function
$\underline{g}$	vector of gravitational acceleration
g_a	a fitting parameter that is related to the air entry value of the soil
g_n	a fitting parameter that is a function of the rate of water extraction from the soil once the air entry value has been exceeded
g_c	a fitting parameter which is used in the general Van Genuchten equation
g_l	a fitting parameter that has to be measured for a specific material
$\underline{\underline{k}}$	tensor of permeability
k_{rel}	relative permeability
$\underline{\underline{k}}^{sat}$	saturated permeability matrix
$m_{soft,\varphi}$	rate of friction softening
$m_{soft,c}$	rate of cohesion softening
n	soil porosity
p'	mean effective stress
p_a	pore air pressure
p_w	pore water pressure / suction pore pressure
q	equivalent shear stress / specific discharge
s	Mohr-Coulomb failure envelope
w_i	weighting coefficient of sampling planes i

Capital letters

A_d	parameter controlling relative proportion of distortional and volumetric degradation
D_e	elastic stiffness matrix of the soil mass
E	young modulus
E_u	undrained young modulus
G	shear modulus
H	height of the slope
K_o	coefficient of earth pressure at rest
K_w	bulk modulus of the water
K_u	undrained bulk modulus of the soil as a whole (soil skeleton and water)
K_{air}	bulk modulus of the air
S	degree of saturation
S_e	effective degree of saturation
S_{res}	residual saturation
S_{sat}	saturation when the pores are filled with water
$\boldsymbol{T}_i$	transformation matrix

Small Greek letters

α	switch parameter
β	compressibility of water
β_w	compressibility of pure water
γ	total unit weight of soil
γ_{sat}	saturated soil weight below the phreatic level
γ_{unsat}	unsaturated soil weight above the phreatic level
η	factor of safety
ε	strain
ε^e	elastic strain
ε^p	plastic strain
$\varepsilon_{\mathrm{di}}$	damage strain on the level of sampling plane
$\varepsilon_{\mathrm{di,\ peak}}$	damage strain on the level of sampling plane at peak strength
$\varepsilon_{\mathrm{di,\ res}}$	damage strain on the level of sampling plane at residual strength
ε_n^p	plastic normal strain on sampling plane
ε_γ^p	plastic shear strain on sampling plane
ν	Poisson’s ratio
ν_u	undrained Poisson’s ratio
ρ_w	density of water
σ	total stress

σ'	effective stress
σ_{xx}	total stress in x direction
σ_{yy}	total stress in y direction
σ_{zz}	total stress in z direction
σ'_{xx}	effective stress in x direction
σ'_{yy}	effective stress in y direction
σ'_{zz}	effective stress in z direction
σ_{xy}	total shear stress in x-y direction
σ_{yz}	total shear stress in y-z direction
σ_{zx}	total shear stress in z-x direction
σ'_{xy}	effective shear stress in x-y direction
σ'_{yz}	effective shear stress in y-z direction
σ'_{zx}	effective shear stress in z-x direction
σ_1	minor principal effective stress
σ_3	major principal effective stress
ϕ_p	suction pore pressure head
φ	friction angle
φ'	effective friction angle
φ_u	undrained friction angle
φ'_{mob}	mobilised friction angle
φ'_{peak}	effective friction angle at peak strength
φ'_{res}	effective friction angle at residual strength
ψ	dilation angle
λ	plastic multiplier
χ	matric suction coefficient

Abbreviation:

FE	Finite Element
FEM	Finite Element Method
FOS	Factor of Safety
LEM	Limit Equilibirum Method
MC	Mohr Coulomb Model
ML	Multilaminate Model
SWCC	Soil Water Characteristics Curve

1 Introduction

1.1 Motivation

The development of soil and rock mechanics will influence the development of slope stability analyses in geotechnical engineering. Assessing the stability of engineered and natural slopes is a common challenge to both theoreticians and practitioners. The balance of natural slopes may be interrupted by man or nature causing stability problems. Natural slopes that have been stable for many years may suddenly fail due to changes in topography, seismicity, groundwater flows, loss of shear strength, stress change, and weathering (Abramson *et al.*, 2002).

Increasing of shear stresses or decreasing of shear strengths of the soils will cause slope failures. The factors that cause increasing shear stresses in slopes are removal of support (e.g. cuts, excavations, erosion, drawdown conditions, etc.), overloading (e.g. construction of fill, weight of rains precipitation, etc.), temporary effect (e.g. earthquakes), removal of underlying materials that provided support (e.g. by excavation or mining, etc), and increase in lateral pressure (e.g. by water in cracks and fissures, expansion of clays, etc). The factors that cause decreasing of shear strength in slope are factors inherent in the nature of the material, changes caused by weathering, effect of pore pressures, and changes in structure.

The main aim of slope stability analyses is to contribute to the safe and economic design of an engineered slope or natural slopes (e.g. excavations, embankments, landfills, etc). Generally, the objectives of slope stability analysis are to investigate the potential of failure mechanism, to assess the slope stability under short-term and long-term conditions, and to analyze the influence of environmental factors that caused instability of the slope.

In short-term stability, undrained conditions should be considered in the analysis and generally, the total stress analysis with undrained shear strength parameter is used to calculate the factor of safety. The methods that specify undrained behaviour in an effective stress analysis using effective stress models can be used in the slope stability analysis when numerical methods are employed.

A progressive failure in slope can occur due to a reduction of strength with increasing strain. For a slope in a strain softening material, it cannot be assumed that the factor of safety greater than one based on peak shear strength means stability, because deformations may lead to a local loss of strength, requiring mobilization of additional strength at other points along the slip surface. This mechanism leads to additional movement and further strain softening. Hence, if the peak strength is mobilized anywhere along the failure surface, a slope in strain softening materials is at risk of progressive failure.

The influence of negative pore-water pressure or suction is generally not taken into account in slope stability analysis. The suction will be reduced with rainfall infiltration and therefore it can be assumed that matric suction does not influence the long term stability of the slope. However, to reduce the suction from the soil, the rainfall needs to be sustained over a significant time period and also the rainfall intensity needs to approximate the saturated coefficient of permeability of the soil at the ground surface and stability analysis in unsaturated slope subjected to rainfall infiltration requires fully coupled flow-deformation analysis with time dependent boundary conditions.

Water pressure such as pore-water pressure and surface water pressure have a great influence in slope stability analysis. Pore-water pressures will act as internal force and surface water pressure will act as external force in slope stability analysis. These pressures can change as the water level changes (water drawdown conditions). In practice, the fully slow and the fully rapid drawdown are commonly used in the slope stability analysis considering drawdown conditions. With these conditions, the computed FOS's may under estimate or over estimate the actual FOS. Consequently, the transient drawdown condition is necessary to reflect field conditions.

Slope stability methods vary in their theoretical background and approach and hence the analysis results vary depending on the used theory. Therefore, the chosen method should be able to identify the real condition of stability of the slope. A comparative study of various available programs in slope stability analysis is demonstrated by Alkasawneh *et al*. (2007) and Hammouri *et al*. (2008). Due to uncertainties in some parameters such as shear strength, probabilistic methods could be considered in slope stability analysis. Griffiths and Fenton (2004) investigated the probability of failure of a slope using both simple and more advanced probabilistic analysis methods. However, probabilistic methods are not considered in this study.

1.2 Outline of thesis

The main objective of this research is to carry out different analysis of slope stability using the finite element method. All the finite element analyses were performed utilizing the finite element code PLAXIS (Brinkgreve et al., 2008). The outline of this thesis is the following:

Chapter 2 presents the comparison between two methods of slope stability analyses, one based on limit equilibrium methods and the other based on the finite element method. Some examples of slope stability analyses using the Mohr-Coulomb model are presented in this chapter. The computed factor of safety and failure mechanisms obtained from these two approaches will be discussed.

Slope stability analysis considering undrained behaviour is discussed in Chapter 3. In this chapter, the computed factor of safety and failure mechanisms of a cutting slope obtained from three methods of modelling undrained behaviour will be evaluated. The analysis was performed using a Mohr-Coulomb model.

Chapter 4 presents the comparison between two approaches of slope stability analyses, namely strain softening and strength reduction approach. The failure mechanism of a simple slope obtained by a strain softening and strength reduction approach respectively are described in this chapter. Analysis of slope stability was performed by using a Mohr Coulomb and a Multilaminate model.

Slope stability analysis considering unsaturated soil behaviour is presented in Chapter 5. The effect of hydraulic characteristics of soils, the location of ground water table and rainfall will be evaluated. A simple slope with four different hydraulic characteristic of soil will be analyzed using constant rainfall intensity. The slope stability analysis with rain infiltration was performed by a fully coupled flow-deformation analysis that computes simultaneously deformation and ground-water flow with time dependent boundary conditions. The factor of safety is calculated by means of the shear strength reduction technique. As only ultimate limit states are concerned here, the linear elastic-perfectly plastic Mohr Coulomb constitutive model is employed.

Back analysis of an unsaturated soil slope subjected to rainfall infiltration will be discussed in Chapter 6. This chapter presents results from the back analysis of a well instrumented and monitored 11-m high cut slope in Zaoyang, Hubei, China in order to get a better understanding of the complex soil water interaction in an unsaturated soil slope subjected to rainfall infiltration.

Chapter 7 describes slope stability analysis during drawdown conditions. Three drawdown conditions namely fully slow drawdown, fully rapid drawdown, and transient drawdown will be discussed in this chapter. The influence of hydraulic characteristics of the soil with different drawdown rates and drawdown ratio in a simple slope will be evaluated. The computed factor of safety and failure mechanism in all drawdown conditions will be compared.

Finally, the main findings on the slope stability evaluations are summarized in Chapter 8, including recommendations for further research.

2 Limit Equilibrium vs. Finite Element Method in slope stability

In the evaluation of slopes, the factor of safety values still remain the main indexes for finding out how close or far slopes are from failure. The evaluation can be done my means of conventional slip circle analysis (the limit equilibrium methods) or by means of numerical methods such as the finite element method.

Duncan (1996) illustrated that the finite element method can be used to analyze the stability and deformations of slopes. Griffiths and Lane (1999) illustrated that the finite element method represents a powerful alternative method for slope stability analysis which is accurate, adaptable and requires less assumptions, especially concerning the failure mechanism. The failure mechanisms in the finite element method develop naturally through the regions wherein the shear strength of the soil is not sufficient to resist the shear stresses.

The main objective of this section is to evaluate and to compare the methods of slope stability analysis between limit equilibrium and finite element method by assuming a Mohr-Coulomb failure criterion.

2.1 Limit Equilibrium Methods

Limit equilibrium methods are the most commonly used approaches in slope stability analysis. The fundamental assumption in these methods is that failure occurs through sliding of a mass along a slip surface. The reputation of the limit equilibrium methods is principally due to their relative simplicity, the ability to evaluate the sensitivity of stability to various input parameters, and the experience geotechnical engineer have acquired over the years in calculating the factor of safety.

The assumptions in the limit equilibrium methods are that the failing soil mass can be divided into slices and that forces act between the slices whereas different assumptions are made with respect to these forces in different methods. Some common features and limitation for equilibrium methods in slope stability analysis are summarized in Table 1. All methods use the same definition of the factor of safety:

$$FOS = \frac{Shear\ strength\ of\ soil}{Shear\ stress\ required\ for\ equilibrium} \qquad (1)$$

The factor of safety is the factor by which the shear strength of the soil would have to be divided to carry the slope into a state of barely stable equilibrium.

Tab. 1: Features and Limitation for Traditional Equilibrium Methods in Slope Stability Analysis (Duncan and Wright, 1980)

Method	Features and Limitation
Slope Stability Charts (Janbu, 1968, Duncan *et al*, 1987)	- Accurate enough for many purposes. - Faster than detailed computer analysis.
Ordinary Method of Slices (Fellenius, 1927)	- Only for circular slip surfaces. - Satisfies moment equilibrium. - Does not satisfy horizontal or vertical force equilibrium.
Bishop's Modified Method (Bishop, 1955)	- Only for circular slip surfaces. - Satisfies moment equilibrium. - Satisfies vertical force equilibrium. - Does not satisfy horizontal force equilibrium.
Force Equilibrium Methods (e.g. Lowe and Karafiath, 1960, Army Corps of Engineers, 1970)	- Any shape of slip surfaces. - Does not satisfy moment equilibrium. - Satisfies both vertical and horizontal force equilibrium.
Janbu's Generalized Procedure of Slices (Janbu, 1968)	- Any shape of slip surfaces. - Satisfies all conditions of equilibrium. - Permit side force locations to be varied. - More frequent numerical problems than some other methods.
Morgenstern and Price's Method (Morgenstern and Price, 1965)	- Any shape of slip surfaces. - Satisfies all conditions of equilibrium. - Permit side force orientations to be varied.
Spencer's Method (Spencer, 1967)	- Any shape of slip surfaces. - Satisfies all conditions of equilibrium. - Side forces are assumed to be parallel.

The findings related to the accuracy of the limit equilibrium methods can be reviewed as follows:

1) For effective stress analysis of flat slopes, the ordinary method of slices is highly inaccurate. The computed factor of safety is too low. This method is accurate for $\phi = 0$ analysis, and fairly accurate for any type of total stress analysis using circular slip surfaces.
2) For most conditions, the Bishop's modified method is reasonably accurate. Because of numerical problems, sometimes encountered, the computed factor

of safety using the Bishop's modified method is different from the factor of safety for the same circle calculated using the ordinary method of slices.

3) Computed factor of safety using force equilibrium methods are sensitive to the assumption of the inclination of side forces between slices. A bad assumption concerning side force inclination will result in an inaccurate factor of safety.
4) Janbu's, Morgenstern and Prices's and Spencer's method that satisfy all conditions of equilibrium are accurate for any conditions. All of these methods have numerical problems under some conditions.

The limitation of limit equilibrium method in slope stability analysis has been demonstrated by Krahn (2003). This limitation is caused by the absence of a stress-strain relationship in the method of analysis. The limit equilibrium method lacks a suitable procedure for slope stability analysis under rapid loading condition as illustrated by Baker *et al.* (1993).

2.2 Finite Element Method

In the finite element method, the latter analysis, the so-called shear strength reduction (SSR) technique (Matsui & San 1992, Dawson *et al.* 1999) can be applied. The angle of dilatancy, soil modulus or the solution domain size are not critical parameters in this technique (Cheng, 1997). The safety factor can be obtained, assuming a Mohr-Coulomb failure criterion, by reducing the strength parameters incrementally, starting from unfactored values $\varphi_{available}$ and $c_{available}$, until no equilibrium can be found in the calculations. The corresponding strength parameters can be denoted as $\varphi_{failure}$ and $c_{failure}$ and the safety factor η_{fe} is defined as:

$$\eta_{fe} = \frac{\tan \varphi_{available}}{\tan \varphi_{failure}} = \frac{c_{available}}{c_{failure}} \qquad (2)$$

There are two possibilities to arrive at the factor of safety as defined above.

Method 1: An analysis is performed with unfactored parameters modelling all construction stages required. The results represent the behaviour for working load conditions at the defined construction steps. This analysis is followed by an automatic reduction of strength parameters of the soil until equilibrium can be no longer achieved in the calculation. The procedure can be invoked at any construction step. This approach is sometimes referred to as φ/c-reduction technique.

Method 2: The analysis is performed with factored parameters from the outset, i.e. strength values are reduced, again in increments, but a new analysis for all construction stages is performed for each set of parameters. If sufficiently small increments are used the factor of safety is again obtained from the calculation where equilibrium could not be achieved.

Both methods are straightforward to apply when using a standard Mohr-Coulomb failure criterion.

In the finite element method, failure occurs naturally through the zones within the soil mass wherein the shear strength of the soil is not capable to resist the applied shear stress, so there is no need to make assumption about the shape or location of the failure surface.

2.3 Mohr-Coulomb Failure Criterion

The Mohr-Coulomb failure criterion is commonly used to describe the strength of soil. The relationship between shear strength and the principal stresses active on a mass of soil can be represented in terms of the Mohr circle of stress where the limits on the principal stress axis represent the major and minor principal stresses, σ_1 and σ_3. Mohr-Coulomb's failure criterion (Figure 1) is a line forming a tangent to the circle at point *a*. The slope of this line is the friction angle, φ, and the line intercepts the shear stress axis at the value of the soil's cohesion, *c*.

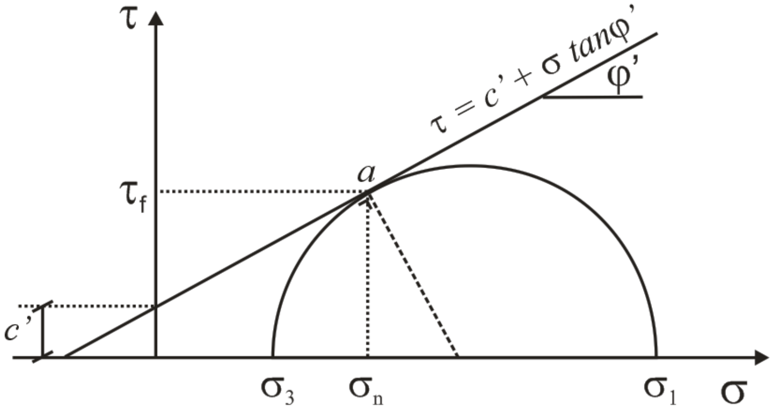

Fig. 1: Mohr-Coulomb failure criterion

So, the Mohr-Coulomb failure envelope may be described by:

$$\tau = c' + \sigma' \tan \varphi' \tag{3}$$

Alternatively the Mohr-Coulomb criterion can be formulated in terms of principal stresses as follows:

$$f_{1a} = \tfrac{1}{2}(\sigma'_2 - \sigma'_3) + \tfrac{1}{2}(\sigma'_2 + \sigma'_3)\sin\varphi - c\cos\varphi \le 0 \tag{4}$$

$$f_{1b} = \tfrac{1}{2}(\sigma'_3 - \sigma'_2) + \tfrac{1}{2}(\sigma'_3 + \sigma'_2)\sin\varphi - c\cos\varphi \le 0 \tag{5}$$

$$f_{2a} = \tfrac{1}{2}(\sigma'_3 - \sigma'_1) + \tfrac{1}{2}(\sigma'_3 + \sigma'_1)\sin\varphi - c\cos\varphi \le 0 \tag{6}$$

$$f_{2b} = \tfrac{1}{2}(\sigma'_1 - \sigma'_3) + \tfrac{1}{2}(\sigma'_1 + \sigma'_3)\sin\varphi - c\cos\varphi \le 0 \tag{7}$$

$$f_{3a} = \tfrac{1}{2}(\sigma'_1 - \sigma'_2) + \tfrac{1}{2}(\sigma'_1 + \sigma'_2)\sin\varphi - c\cos\varphi \le 0 \tag{8}$$

$$f_{3b} = \tfrac{1}{2}(\sigma'_2 - \sigma'_1) + \tfrac{1}{2}(\sigma'_2 + \sigma'_1)\sin\varphi - c\cos\varphi \le 0 \tag{9}$$

Figure 2 illustrates a fixed hexagonal cone in principal stress space with the condition $f_i = 0$ for all yield function.

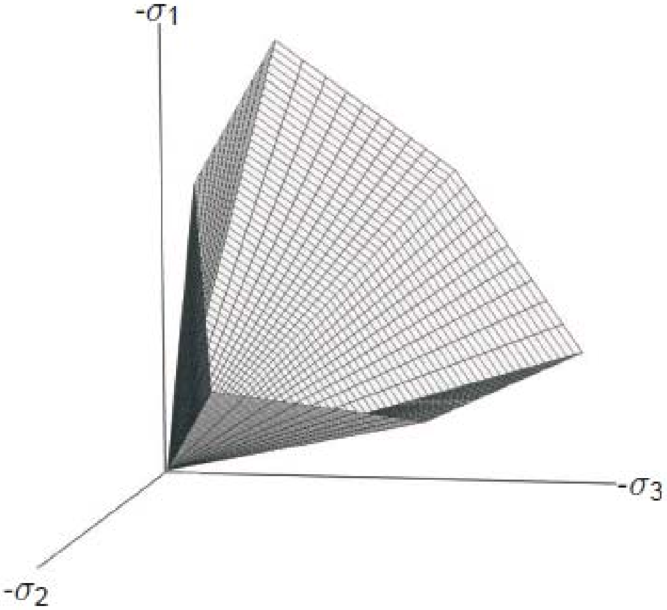

Fig. 2: The Mohr-Coulomb yield surface ($c = 0$) (Brinkgreve *et al*, 2010)

The Mohr-Coulomb plastic potential functions that contain a third plasticity parameter, the so-called dilatancy angle ψ are given by:

$$g_{1a} = \tfrac{1}{2}(\sigma'_2 - \sigma'_3) + \tfrac{1}{2}(\sigma'_2 + \sigma'_3)\sin\psi \tag{10}$$

$$g_{1b} = \tfrac{1}{2}(\sigma'_3 - \sigma'_2) + \tfrac{1}{2}(\sigma'_3 + \sigma'_2)\sin\psi \tag{11}$$

$$g_{2a} = \tfrac{1}{2}(\sigma'_3 - \sigma'_1) + \tfrac{1}{2}(\sigma'_3 + \sigma'_1)\sin\psi \tag{12}$$

$$g_{2b} = \tfrac{1}{2}(\sigma'_1 - \sigma'_3) + \tfrac{1}{2}(\sigma'_1 + \sigma'_3)\sin\psi \tag{13}$$

$$g_{3a} = \tfrac{1}{2}(\sigma'_1 - \sigma'_2) + \tfrac{1}{2}(\sigma'_1 + \sigma'_2)\sin\psi \tag{14}$$

$$g_{3b} = \tfrac{1}{2}(\sigma'_2 - \sigma'_1) + \tfrac{1}{2}(\sigma'_2 + \sigma'_1)\sin\psi \tag{15}$$

Generally, the linear perfectly-plastic Mohr-Coulomb model requires five parameter. These parameters are the Young's modulus (E), Poisson's ratio (ν), cohesion (c), friction angle (φ), and dilatancy angle (ψ).

2.4 Slope stability examples

In this section, five examples of slope stability analysis from Griffiths and Lane (1999) will be discussed. These examples will be analyzed by the finite element method and will be compared with the limit equilibrium methods. The analysis was performed by utilizing PLAXIS for the finite element method and Slope/W for the limit equilibrium methods. The soil model used in the analysis is the Mohr-Coulomb failure criterion.

2.4.1 Homogeneous slope with no foundation layer

The height of the homogeneous slope is 10 m and the gradient (horizontal to vertical) is 2:1. Figure 3 illustrates the geometry and the two dimensional finite element meshes consisting of 390 15-noded elements.

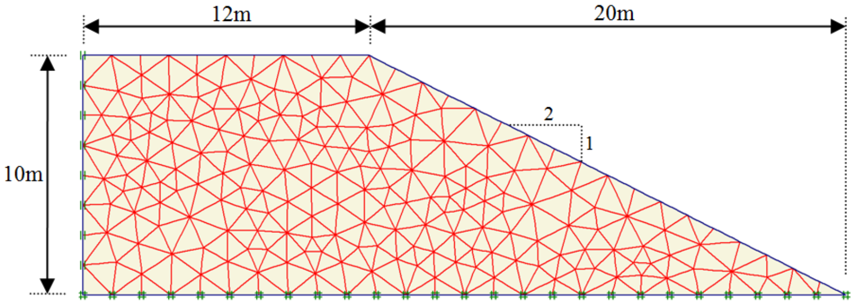

Fig. 3: Geometry and mesh for a homogeneous slope with no foundation layer

The soil parameters for this example are given in Table 2.

Tab. 2: Soil Parameters for Example 1 with Mohr Coulomb Model

Description	Symbol	Unit	Value
Unit weight	γ	[kN/m^3]	20
Effective young's modulus	E'	[kPa]	100000
Effective poisson's ratio	ν'	[-]	0.3
Cohesion (effective shear strength)	c'	[kPa]	10
Friction angle (effective shear strength)	ϕ'	[°]	20

In Figure 4 the failure mechanism for this example is presented for the finite element method. The result of the slope stability analysis using a limit equilibrium method is presented in Figure 5.

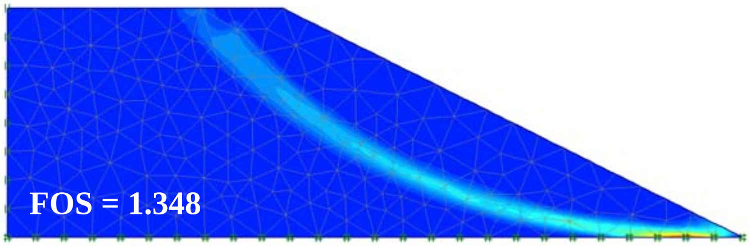

Fig. 4: Failure mechanism for a homogeneous slope with no foundation using the finite element method

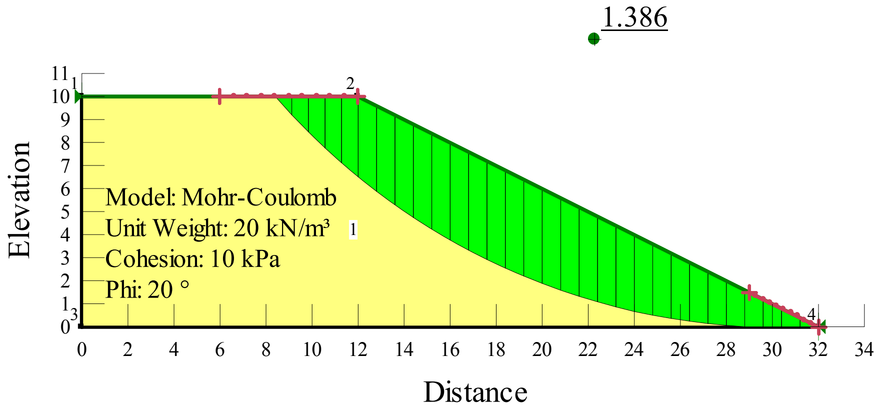

Fig. 5: Morgenstern and Price Method for a homogeneous slope with no foundation

The difference of factor of safety between the finite element method and limit equilibrium methods is only 2.8% and the failure mechanism are similar.

2.4.2 Homogeneous slope with a foundation layer

The homogeneous slope has a foundation layer with the thickness of half of the slope height in this example. The height of the slope is 10 m and the gradient (horizontal to vertical) is 2:1. Figure 6 shows the geometry and the two dimensional finite element mesh consisting of 309 15-noded elements.

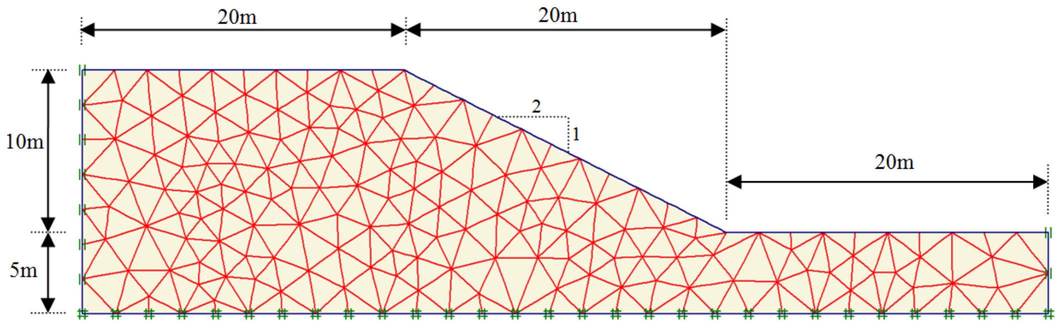

Fig. 6: Geometry and mesh for a homogeneous slope with a foundation layer

The soil parameters used for this example are the same as given in Table 2. In Figure 7 the failure mechanism is presented for the finite element method and the result of the analysis using a limit equilibrium method is presented in Figure 8.

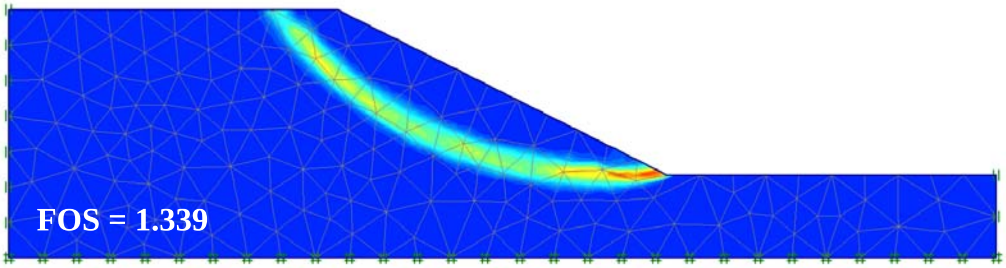

Fig. 7: Failure mechanism for a homogeneous slope with a foundation layer using the finite element method

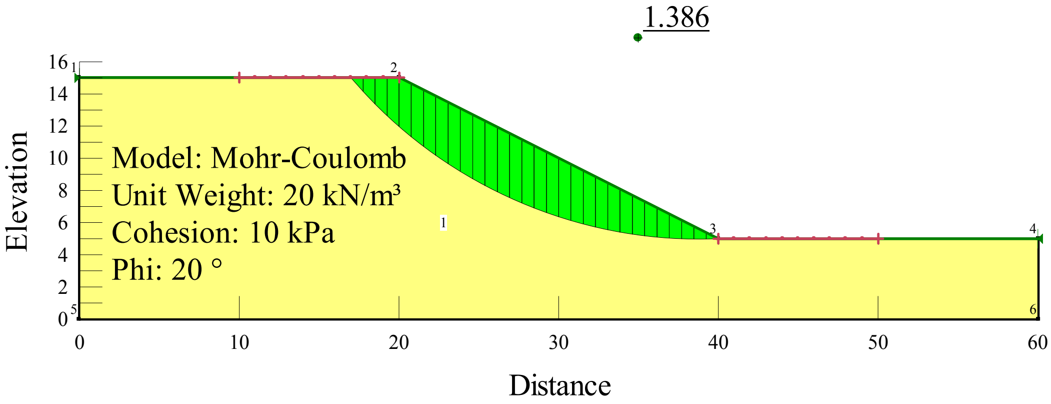

Fig. 8: Morgenstern and Price Method for a homogeneous slope with a foundation layer

The difference of factor of safety between the finite element method and limit equilibrium methods is only 3.5% and the computed failure mechanism are similar.

2.4.3 An undrained clay slope with a thin weak layer

Figure 9 shows the geometry and the two dimensional finite element mesh of the example of an undrained clay slope with a thin weak layer. The height of the slope is 10 m and the slope is inclined at an angle of 26.57^{o} (2:1) to the horizontal. The mesh consist of 562 15-noded elements.

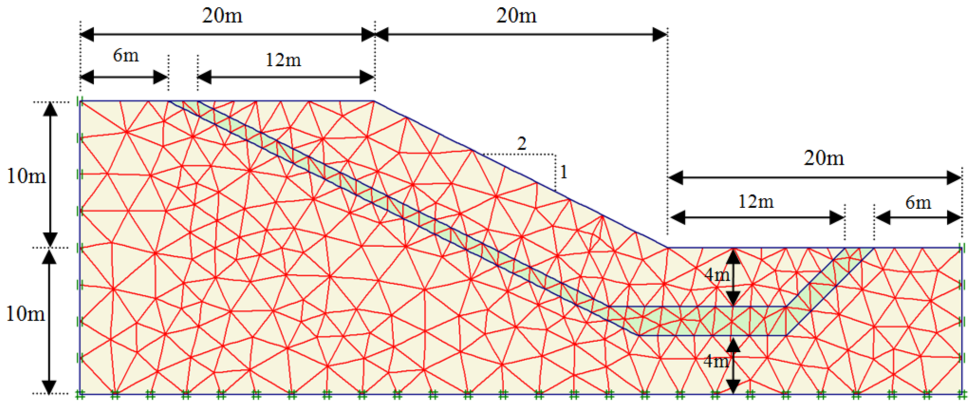

Fig. 9: Geometry and mesh for an undrained clay slope with a thin weak layer

The soil parameters for this example are given in Table 3. The analyses are carried out using a constant value of undrained shear strength of the soil (c_{u1}) and five different values of undrained shear strength of the thin layer (c_{u2}) with ratios c_{u2}/c_{u1} equal to 1, 0.8, 0.6, 0.4, and 0.2.

Tab. 3: Soil Parameters for Example 3 with Mohr Coulomb Model

Description	Symbol	Unit	Value
Unit weight	γ	[kN/m^3]	20
Effective young's modulus	E’	[kPa]	100000
Effective poisson's ratio	ν'	[-]	0.3
Cohesion (undrained shear strength)	c_{u1}	[kPa]	50
Friction angle (undrained shear strength)	ϕ_u	[^{o}]	0

In Figure 10 computed failure mechanisms for this example are presented for the finite element method with different ratios c_{u2}/c_{u1} and the result of the analysis using a limit equilibrium method is presented in Figure 11.

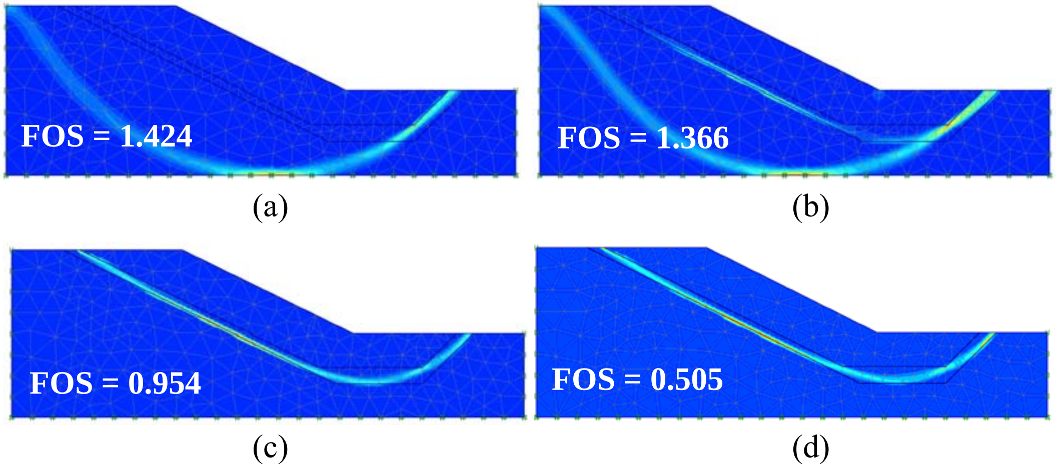

(a) (b)

(c) (d)

Fig. 10: Failure mechanism for an undrained clay slope with a thin weak layer using Finite Element Method; (a) $c_{u2}/c_{u1} = 0.8$; (b) $c_{u2}/c_{u1} = 0.6$; (c) $c_{u2}/c_{u1} = 0.4$; (d) $c_{u2}/c_{u1} = 0.2$

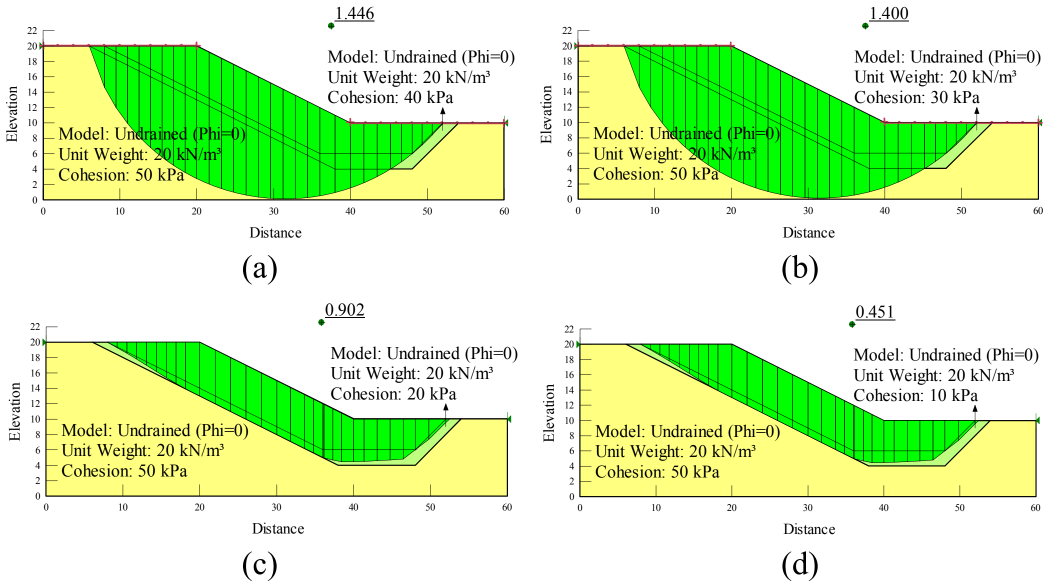

(a) (b)

(c) (d)

Fig. 11: Morgenstern and Price Method for an undrained clay slope with a thin weak layer; (a) $c_{u2}/c_{u1} = 0.8$; (b) $c_{u2}/c_{u1} = 0.6$; (c) $c_{u2}/c_{u1} = 0.4$; (d) $c_{u2}/c_{u1} = 0.2$

The factor of safety obtained using the finite element and limit equilibrium methods for this example are summarised in Table 4 and illustrated in Figure 12.

Tab. 4: Computed factor of safety for Example 3

c_{u2}/c_{u1}	FOS	
	Finite Element Method	Morgenstern and Price Method
1.0	1.451	1.448
0.8	1.424	1.446
0.6	1.366	1.400
0.4	0.954	0.902
0.2	0.505	0.451

The computed factor of safety with the ratio $c_{u2}/c_{u1} > 0.6$ using the finite element method are close to the Morgenstern and Price method and the failure mechanisms of these methods are similar. With these ratios, the strength of the thin weak layer does not affect the safety factor of the slope and generate a circular (base) mechanism of failure. When the ratio c_{u2}/c_{u1} reduced to 0.6, the finite element method produce two failure mechanisms. The first failure mechanism is a base mechanism combined with the weak layer beyond the slope toe and the second failure mechanism is a non-circular mechanism closely following the geometry of the thin weak layer. This is shown in Figure 10. With this ratio, the Morgenstern and Price method only produce one failure mechanism, the so-called circular (base) mechanism. When the ratio c_{u2}/c_{u1} is reduced to 0.4 and 0.2, the failure mechanism of the slope shows a non-circular mechanism closely following the geometry of the thin weak layer. However, with the ratio $c_{u2}/c_{u1} \leq 0.6$, there is no significant difference of factor of safety between the finite element method and the Morgenstern and Price method.

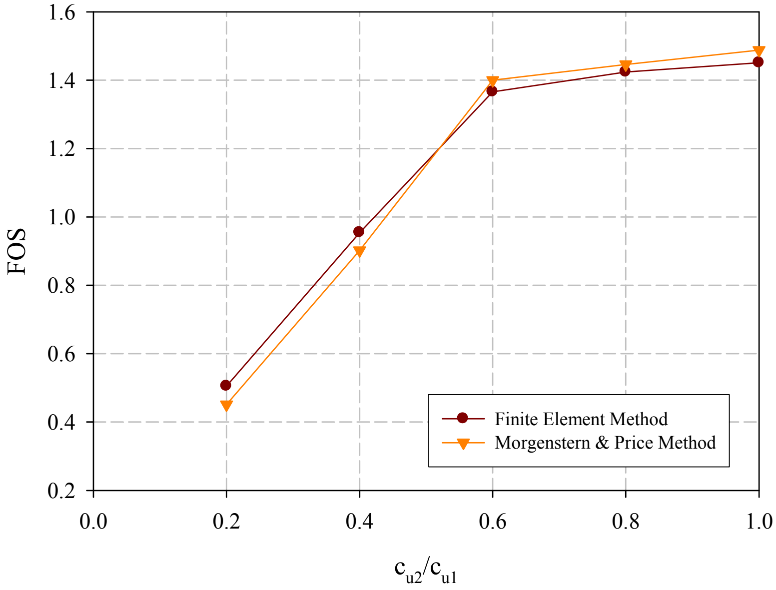

Fig. 12: Computed FOS for an undrained clay slope with a thin weak layer with variations of c_{u2}/c_{u1}

2.4.4 An undrained clay slope with a weak foundation layer

In this example analysis of an undrained clay slope of 10m height and a 10m thick foundation layer is carried out. The slope is inclined at an angle of 26.57^o (2:1) to the horizontal. Figure 13 shows the geometry and the two dimensional finite element mesh consisting of 562 15-noded elements.

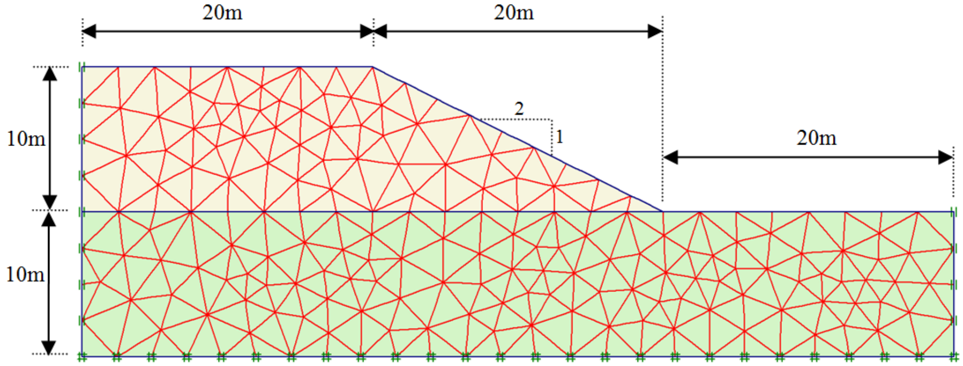

Fig. 13: Geometry and mesh for an undrained clay slope with a weak foundation layer

The soil parameters used for this example are given in Table 3. The analysis are carried out using a constant value of undrained shear strength of soil (c_{u1}) and six different values of undrained shear strength of the foundation layer (c_{u2}) with ratios c_{u2}/c_{u1} equal to 0.5, 1.0, 1.5, 1.75, 2.0 and 2.5.

In Figure 14 computed failure mechanisms for this example are presented for the finite element method and the results of slope stability analysis using limit equilibrium methods are presented in Figure 15.

The factor of safety obtained using the finite element and limit equilibrium methods for this example are summarised in Table 5 and illustrated in Figure 16. The average difference of factor of safety between the finite element method and limit equilibrium methods is only 2.2% and the failure mechanisms of these methods are similar except when the ratio c_{u2}/c_{u1} = 1.5. When the ratio c_{u2}/c_{u1} =1.5, the finite element method generates two failure mechanisms, namely a base mechanism and a toe mechanism. It represents the transition between these two fundamental mechanisms. However, with this ratio, the Morgenstern and Price Method only generates one failure mechanism, the so-called toe mechanism.

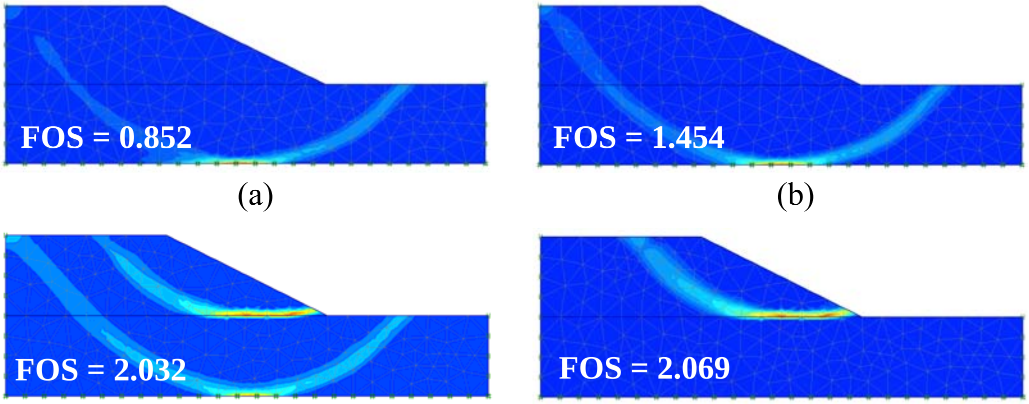

(a) (b)

(c) (d)

Fig. 14: Failure mechanism for an undrained clay slope with a weak foundation layer using the finite element method; (a) $c_{u2}/c_{u1} = 0.5$; (b) $c_{u2}/c_{u1} = 1.0$; (c) $c_{u2}/c_{u1} = 1.5$; (d) $c_{u2}/c_{u1} = 1.75$

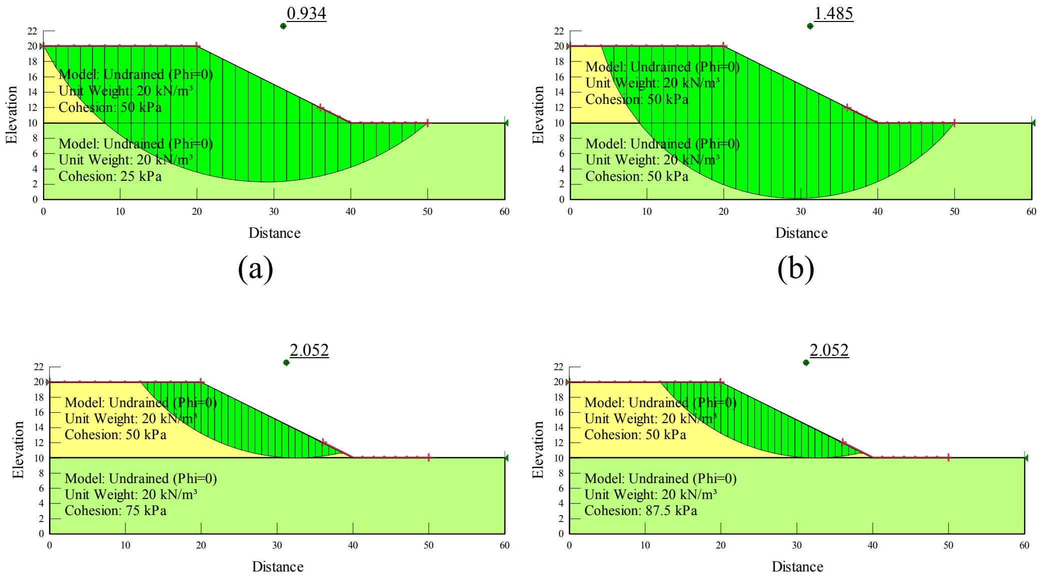

(a) (b)

(c) (d)

Fig. 15: Morgenstern and Price Method for an undrained clay slope with a weak foundation layer; (a) $c_{u2}/c_{u1} = 0.5$; (b) $c_{u2}/c_{u1} = 1.0$; (c) $c_{u2}/c_{u1} = 1.5$; (d) $c_{u2}/c_{u1} = 1.75$

Tab. 5: Computed factor of safety for Example 4

c_{u2}/c_{u1}	FOS	
	Finite Element Method	Morgenstern and Price Method
0.50	0.852	0.934
1.00	1.454	1.485
1.50	2.032	2.052
1.75	2.069	2.052
2.00	2.076	2.064
2.50	2.069	2.064

Figure 16 shows that at $c_{u2}/c_{u1} = 1.5$ the factor of safety remains constant for both methods.

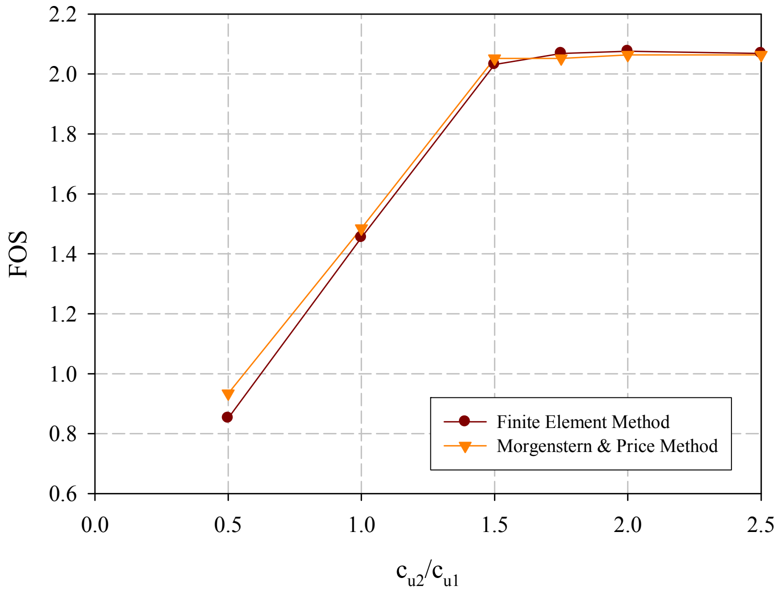

Fig. 16: Computed FOS for an undrained clay slope with a weak foundation layer with variations of c_{u2}/c_{u1}

2.4.5 Homogeneous slope with water level

The geometry, the two dimensional finite element mesh and the soil parameters of this example are the same as the slope analysed in Example 1, combined with a water level at a depth *L* below the crest of the slope (Figure 17).

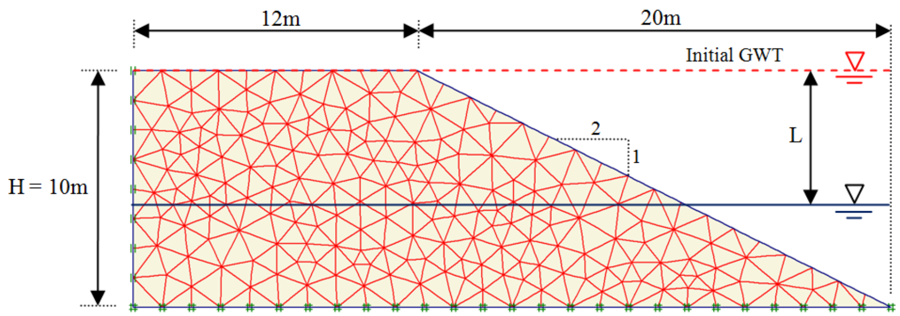

Fig. 17: Geometry and mesh for homogeneous slope with water level

In this analysis, a slope with different drawdown ratios L/H, which has been varied from 0.0 (slope completely submerged with water level at the crest of the slope) to 1.0 (water level at the toe of the slope) is considered. This example is the so-called slow drawdown problem wherein a reservoir, initially at the crest of the slope, is slowly lowered to the base, with the water level within the slope maintaining the same level.

Figure 18 shows the computed failure mechanisms for this example using the finite element method and Figure 19 illustrates the results of slope stability analysis using limit equilibrium methods.

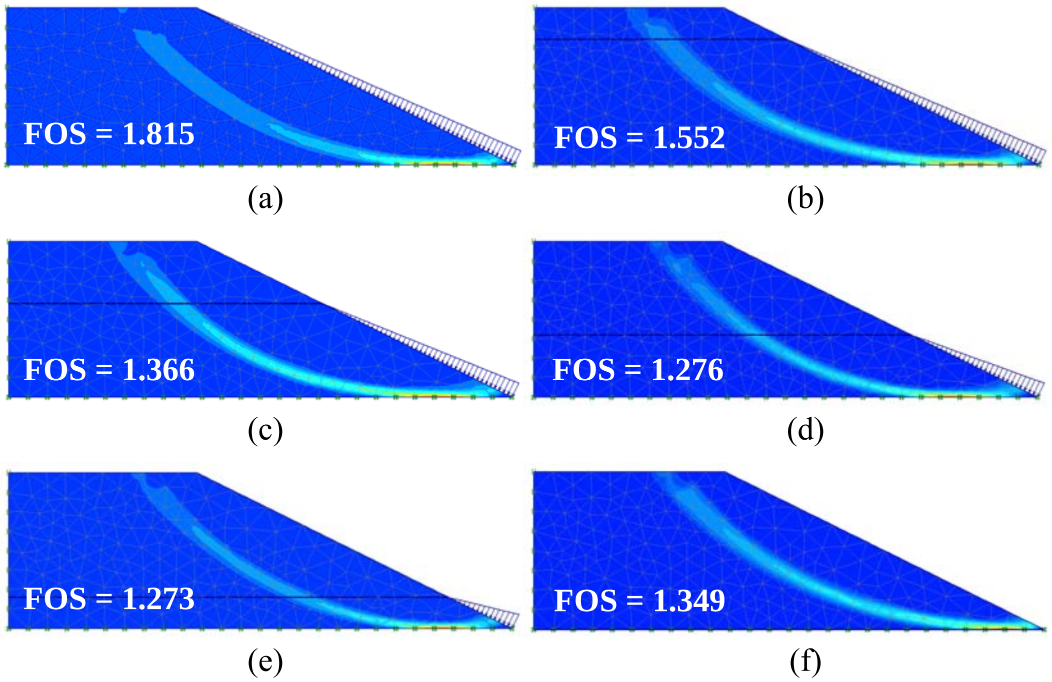

Fig. 18: Failure mechanism for homogeneous slope with water level using the finite element method; (a) L/H = 0.0; (b) L/H = 0.2; (c) L/H = 0.4; (d) L/H = 0.6; (e) L/H = 0.8; (f) L/H = 1.0

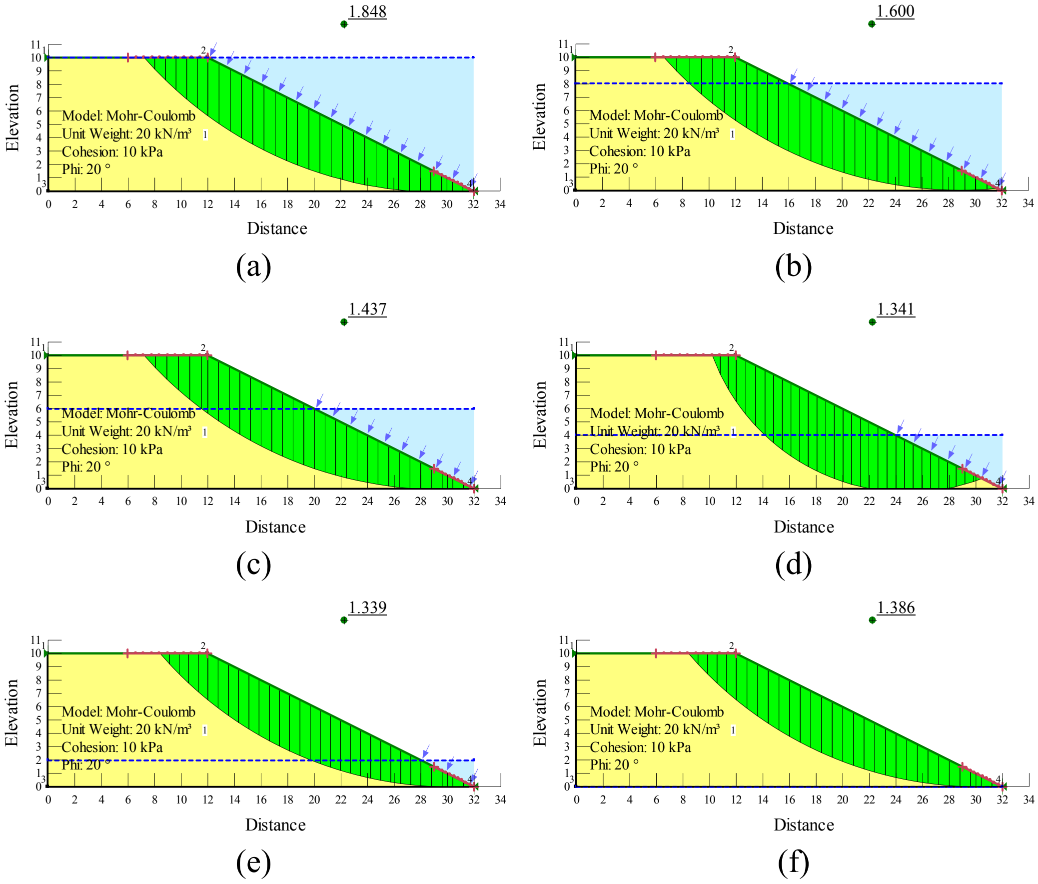

(a) (b) (c) (d) (e) (f)

Fig. 19: Morgenstern and Price Method for homogeneous slope with horizontal water level (L/H = 1.0); (a) L/H = 0.0; (b) L/H = 0.2; (c) L/H = 0.4; (d) L/H = 0.6; (e) L/H = 0.8; (f) L/H = 1.0

The factor of safety obtained using the finite element and limit equilibrium methods for this example are summarised in Table 6 and illustrated in Figure 20. The average difference of factor of safety between the finite element method and limit equilibrium methods is only 3.7% and the failure mechanisms of these methods are similar.

In fully slow drawdown conditions, the factor of safety reaches a minimum when L/H = 0.7 and the fully submerged slope (L/H = 0) is more stable than the dry slope (L/H = 1) as indicated by a higher factor of safety, which has been also demonstrated by Lane and Griffith (2000). The most severe condition is not when the water level was lowered to a minimum. It was observed that the movement near the toe was significantly upward and the failure mechanism changed when the water level was lowered to the base.

Tab. 6: Computed factor of safety for Example 5

L/H	FOS	
	Finite Element Method	Morgenstern and Price Method
-0.1	1.815	1.847
0.0	1.815	1.858
0.1	1.685	1.715
0.2	1.552	1.600
0.3	1.449	1.507
0.4	1.366	1.437
0.5	1.308	1.378
0.6	1.276	1.341
0.7	1.259	1.331
0.8	1.273	1.339
0.9	1.305	1.356
1.0	1.349	1.386

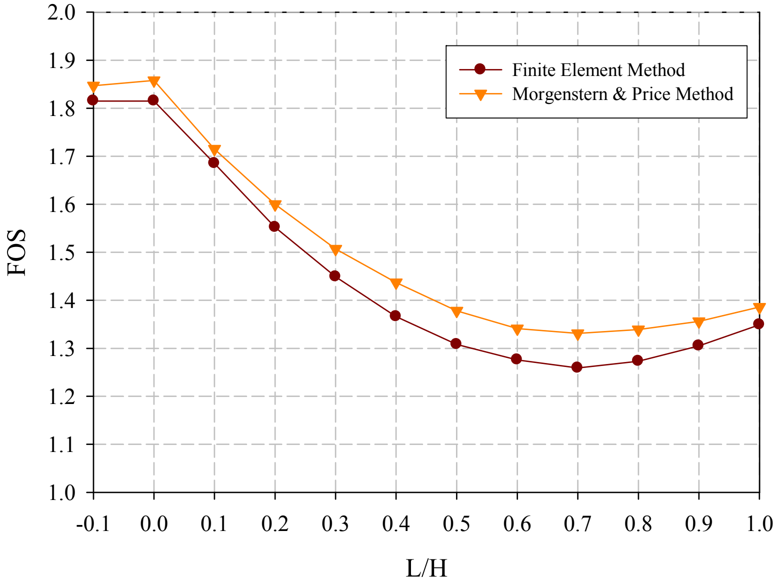

Fig. 20: Computed FOS for homogeneous slope with variations of L/H

2.5 Summary

The two approaches of slope stability analyses, one based on limit equilibrium methods and the other based on the finite element method are widely used in geotechnical engineering. The finite element method in combination with an elastic-perfectly plastic (Mohr-Coulomb) model has been shown to be suitable for slope stability analysis.

In simple cases similar factors of safety and failure mechanism are obtained as in limit equilibrium analysis, however under more complex conditions the finite element method is more versatile because no a priori assumptions on the shape of the failure mechanism has to be made.

3 Slope stability analysis considering undrained behaviour

In general, undrained analysis is appropriate when the permeability of the soil is low and the rate of loading is high. In this analysis, short-term behaviour has to be assessed.

Generally, in short-term stability conditions, a total stress analysis with undrained shear strength parameters is used to calculate the factor of safety. However, when numerical methods are employed an effective stress analysis using effective model parameters can be used for undrained analysis.

The main objective of this section is to evaluate and to compare the computed safety factor and failure mechanism of a simple slope obtained by three methods of modelling undrained behaviour.

3.1 Principle of effective stress

A saturated soil mass consists of two phases: the soil skeleton and the water filled pores between the soil particles. Any stresses forced on such a soil will be maintained by the soil skeleton as effective stress and the pore water as pore-water pressure.

Based on Terzaghi's principle, the effective stress σ' acting any plane within the soil mass is defined by:

$$\sigma'_{xx} = \sigma_{xx} - p_w \tag{16}$$

$$\sigma'_{yy} = \sigma_{yy} - p_w \tag{17}$$

$$\sigma'_{zz} = \sigma_{zz} - p_w \tag{18}$$

where σ is the total stress and p_w is pore water pressure.

The water is assumed not to maintain any shear stress and consequently the effective shear stresses (σ'_{xy}, σ'_{yz}, σ'_{zy}) is equal to total shear stresses (σ_{xy}, σ_{yz}, σ_{zy}):

$$\sigma'_{xy} = \sigma_{xy} \tag{19}$$

$$\sigma'_{yz} = \sigma_{yz} \tag{20}$$

$$\sigma'_{zx} = \sigma_{zx} \tag{21}$$

Since the shear stresses at the particle contact are frictional, the strength is directly controlled by the effective stresses. This shear strength of a soil is implemented via the Mohr-Coulomb failure envelope.

Two useful stress invariants are defined by:

$$p' = \frac{1}{3}\left(\sigma'_{xx} + \sigma'_{yy} + \sigma'_{zz}\right) \tag{22}$$

$$q = \sqrt{\frac{1}{2}\left(\left(\sigma'_{xx} - \sigma'_{yy}\right)^2 + \left(\sigma'_{yy} - \sigma'_{zz}\right)^2 + \left(\sigma'_{zz} - \sigma'_{xx}\right)^2 + 6\left(\sigma_{xy}^2 + \sigma_{yz}^2 + \sigma_{zx}^2\right)\right)} \tag{23}$$

where *p’* is the mean effective stress, and *q* is the equivalent shear stress.

3.2 Effective and total stress analysis

The shear strength of the soil along the failure surface is governed by the effective stress. The effective stress can be calculated when the pore-water pressures are known. In granular soils, excess pore-water pressures tend to dissipate quickly during construction and therefore only drained analyses must be considered. However, in fine-grained soils, excess pore-water pressures dissipate slowly and undrained conditions have to be considered.

In short-term stability conditions, generally a total stress analysis with the strength parameter $\varphi_u = 0^o$ and c_u (undrained strength) is used to calculate the factor of safety. Otherwise, in long-term stability conditions, the effective stress analysis with the strength parameter φ' and c' is used. Figures 21 and 22 describe the explanation for choosing a total or effective stress analysis in design of an embankment and an excavation.

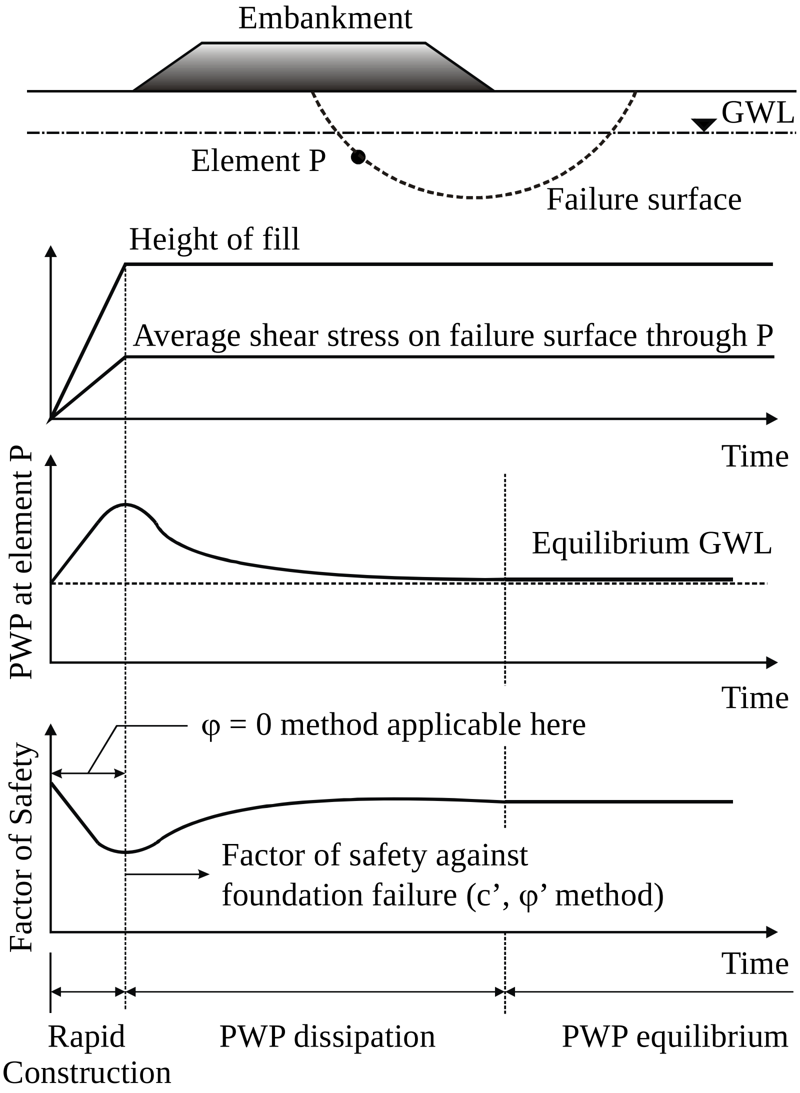

Fig. 21: Changes in pore-water pressure and factor of safety of an embankment on soft clay during and after construction (After Bishop and Bjerrum, 1960)

During an embankment construction, the increase of pore-water pressure at point P in a fine-drained soil is difficult to predict at all locations along the failure surface, therefore the total stress analysis with undrained shear strength parameters will be used to calculate the safety of the slope during and immediately after construction. When the pore-water pressure reach the highest value at the end of construction, the critical minimum factor of safety will be obtained. These explanations illustrate the short-term stability conditions. However, when pore-water pressures are monitored during the construction, the effective stress analysis can be carried out using drained shear strength parameters.

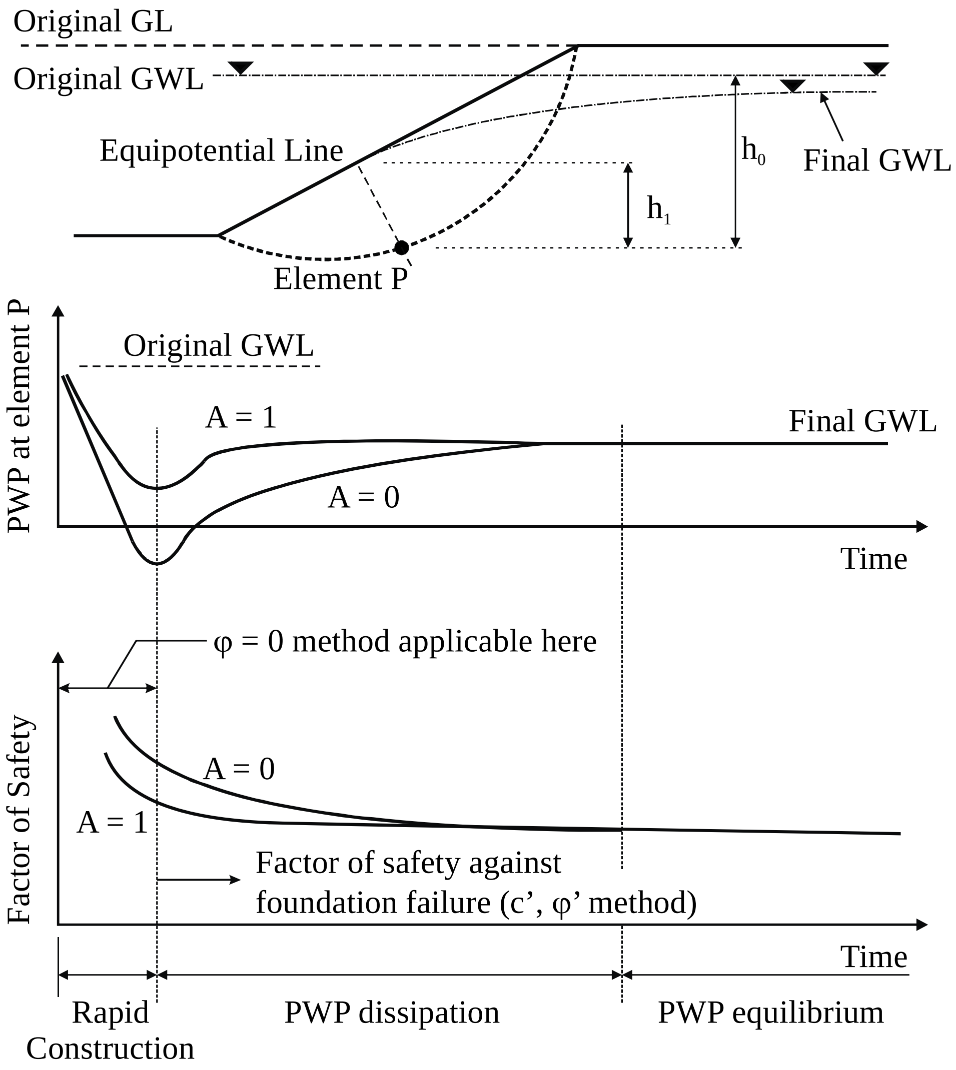

Fig. 22: Changes in pore-water pressure and factor of safety of an excavation on soft clay during and after construction (After Bishop and Bjerrum, 1960)

During an excavation the generation of negative excess pore pressures will increase the effective stresses. When construction is finished, the negative pore pressure will dissipate with time and will decrease the effective stresses. The effective stress analysis can be carried out using drained shear strength parameters to calculate the factor of safety of the slope. When the negative pore-water pressures have completely dissipated, the critical minimum factor of safety will be obtained, defining the long-term stability conditions. For temporary excavation, undrained condition should be considered in the analysis.

Different methods are possible to model undrained soil behaviour. They are called Method A, Method B, and Method C in the following. These methods differ in the use of shear strength and stiffness parameters. Method A and B specify undrained behaviour in an effective stress analysis using effective model parameters, however the Method C performs a total stress analysis with undrained parameters. In the following section a detail description of these methods will be given.

3.2.1 Undrained effective stress analysis

In Method A, undrained effective stress analysis is used in combination with effective strength parameters φ' and *c'* to model the undrained shear strength of the material. In this method, changes in pore pressures play an important role in evaluating the proper effective stress path that causes failure at a value of undrained shear strength which is governed by the constitutive model used. The effective stiffness parameters *E'* and ν' are used in this method.

If undrained shear strength data is available, Method B can be applied. In this method, an undrained shear strength ($c = c_u$ and $\varphi = \varphi_u = 0^o$) and effective stiffness parameters (*E'* and ν') are used in the analysis.

The inverted form of Hooke's law in terms of the effective stress rate and the effective stiffness *E'* and ν' can be written as:

$$\begin{bmatrix} \dot{\varepsilon}^e_{xx} \\ \dot{\varepsilon}^e_{yy} \\ \dot{\varepsilon}^e_{zz} \\ \dot{\varepsilon}^e_{xy} \\ \dot{\varepsilon}^e_{zx} \end{bmatrix} = \frac{1}{E'} \begin{bmatrix} 1 & -\nu' & -\nu' & 0 & 0 & 0 \\ -\nu' & 1 & -\nu' & 0 & 0 & 0 \\ -\nu' & -\nu' & 1 & 0 & 0 & 0 \\ 0 & 0 & 0 & 2+2\nu' & 0 & 0 \\ 0 & 0 & 0 & 0 & 2+2\nu' & 0 \\ 0 & 0 & 0 & 0 & 0 & 2+2\nu' \end{bmatrix} \begin{bmatrix} \dot{\sigma}_{xx} - \dot{p}_w \\ \dot{\sigma}_{yy} - \dot{p}_w \\ \dot{\sigma}_{zz} - \dot{p}_w \\ \dot{\sigma}_{xy} \\ \dot{\sigma}_{yz} \\ \dot{\sigma}_{zx} \end{bmatrix} \tag{24}$$

Considering slightly compressible water, the rate of excess pore pressure is defined by:

$$\dot{p}_w = \frac{K_w}{n}\left(\dot{\varepsilon}^e_{xx} + \dot{\varepsilon}^e_{yy} + \dot{\varepsilon}^e_{zz}\right) \tag{25}$$

wherein K_w is the bulk modulus of the water and *n* is the soil porosity.

In Method A and B, the bulk modulus of water is given by:

$$\frac{K_w}{n} = \frac{3(\nu_u - \nu')}{(1-2\nu_u)(1+\nu')}K' = 300\frac{0.495-\nu'}{1+\nu'}K' > 30K' \tag{26}$$

In Methods A and B, an undrained bulk modulus K_u for the soil as a whole (soil skeleton and water) is assumed and a distinction between total stresses, effective stresses and excess pore pressures is made. The undrained bulk modulus is calculated using Hooke's law of elasticity:

$$K_u = \frac{2G(1+\nu_u)}{3(1-2\nu_u)} \tag{27}$$

$$G = \frac{E'}{2(1+\nu')} \tag{28}$$

where G is the shear modulus and ν_u is the undrained Poisson's ratio. If an undrained Young's modulus (E_u) is available, based on the Hooke's law, the effective Young's modulus is defined by:

$$E' = \frac{2(1+\nu')}{3} E_u \tag{29}$$

3.2.2 Undrained total stress analysis

Method C performs undrained behaviour using a total stress analysis with undrained parameters. In this method, strength is modelled using an undrained shear strength ($c = c_u$ and $\varphi = \varphi_u = 0^o$) and stiffness is modelled using an undrained Young's modulus E_u and an undrained Poisson's ratio ν_u. Normally the undrained Poisson ratio has a value close to 0.5 (between 0.495 and 0.499). It is not possible to use a value 0.5 as an undrained Poisson ratio, because this would lead to singularity of the stiffness matrix.

The disadvantage of the Method C is that no distinction is made between effective stresses and pore pressures. Therefore, all result should be interpreted as total stresses and all pore pressures are equal to zero.

In terms of the total stress rates and the undrained stiffness parameters E_u and ν_u, the inverted form of Hooke's law can be written as:

$$\begin{bmatrix} \dot{\varepsilon}^e_{xx} \\ \dot{\varepsilon}^e_{yy} \\ \dot{\varepsilon}^e_{zz} \\ \dot{\varepsilon}^e_{xy} \\ \dot{\varepsilon}^e_{zx} \end{bmatrix} = \frac{1}{E_u} \begin{bmatrix} 1 & -\nu_u & -\nu_u & 0 & 0 & 0 \\ -\nu_u & 1 & -\nu_u & 0 & 0 & 0 \\ -\nu_u & -\nu_u & 1 & 0 & 0 & 0 \\ 0 & 0 & 0 & 2+2\nu_u & 0 & 0 \\ 0 & 0 & 0 & 0 & 2+2\nu_u & 0 \\ 0 & 0 & 0 & 0 & 0 & 2+2\nu_u \end{bmatrix} \begin{bmatrix} \dot{\sigma}^{'}_{xx} \\ \dot{\sigma}^{'}_{yy} \\ \dot{\sigma}^{'}_{zz} \\ \dot{\sigma}^{'}_{xy} \\ \dot{\sigma}^{'}_{yz} \\ \dot{\sigma}^{'}_{zx} \end{bmatrix} \tag{30}$$

where:

$$E_u = 2G(1+\nu_u) \tag{31}$$

$$\nu_u = \frac{\nu' + \mu(1+\nu')}{1+2\mu(1+\nu')} \tag{32}$$

$$\mu = \frac{1}{3n}\frac{K_w}{K'} \tag{33}$$

$$K' = \frac{E}{3(1-2\nu')} \tag{34}$$

3.2.3 Undrained shear strength

Evaluation of undrained shear strength from a Mohr Circle is described in Figure 23. Assuming elastic material behaviour below the failure surface, the undrained shear strength is given by:

$$c_u = \tfrac{1}{2}\left(\sigma^{'o}_{xx} + \sigma^{'o}_{yy}\right)\sin\varphi' + c'\cos\varphi' \tag{35}$$

$$c_u = \tfrac{1}{2}\left(K_o + 1\right)\sigma^{'o}_{yy}\sin\varphi' + c'\cos\varphi' \tag{36}$$

where *c'* is effective cohesion, *φ'* is effective soil friction angle, c_u is undrained cohesion and K_o is coefficient of earth pressure at rest.

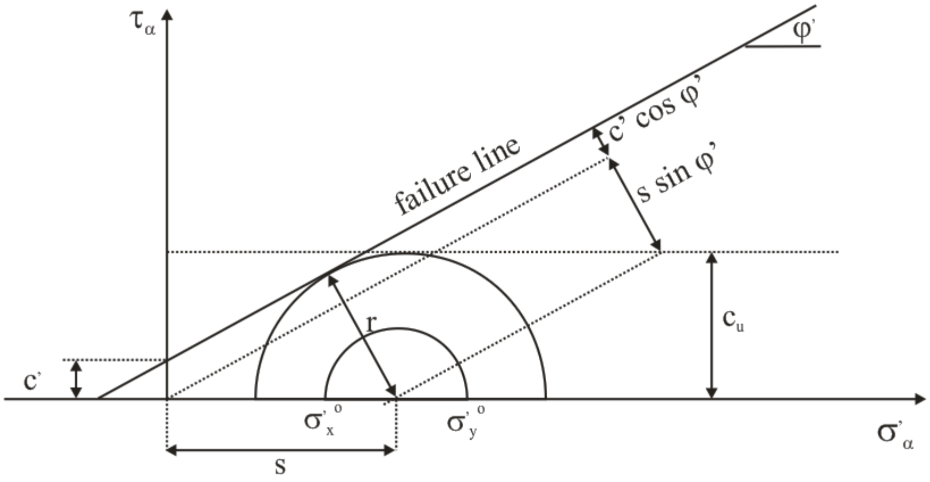

Fig. 23: Mohr Circle for evaluating undrained shear strength

3.3 Numerical model

In this section, three methods of modelling undrained behaviour in slope stability analysis will be evaluated. A simple case, which consists of a cutting slope in a homogeneous fully saturated soil has been chosen.

3.3.1 Geometry, finite element mesh and material properties

The slope is 10 m high and has a 1:2 gradient (horizontal to vertical). The geometry and finite element mesh used are shown in Figure 24. 458 15-noded elements have been used.

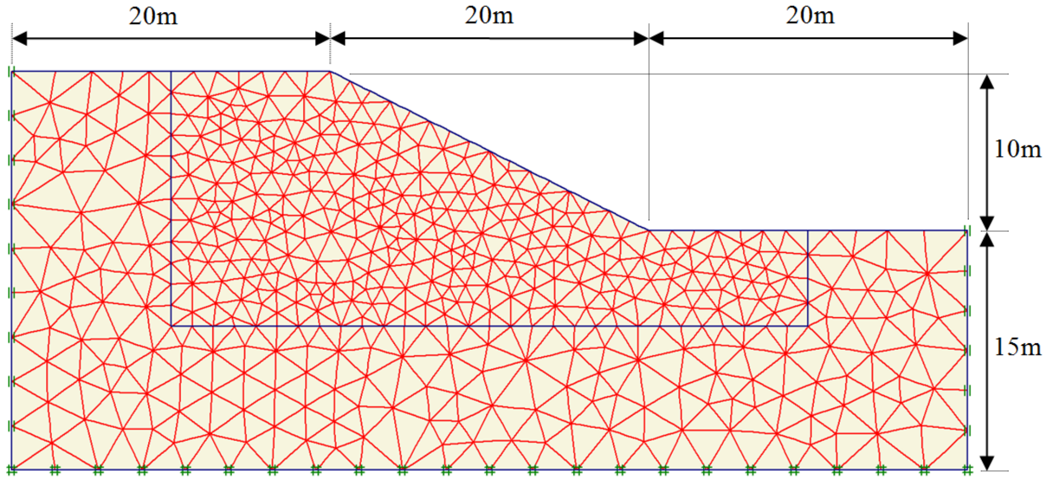

Fig. 24: Geometry and finite element mesh of slope.

The soil parameters for Method A, Method B, and Method C are given in Table 7, 8, and 9 respectively.

Tab. 7: Soil Parameters for Method A using the Mohr Coulomb Model

Description	Symbol	Unit	Value
Unit weight	γ	[kN/m^3]	20
Effective young's modulus	E'	[kPa]	7500
Effective poisson's ratio	ν'	[-]	0.35
Cohesion (effective shear strength)	c'	[kPa]	20
Friction angle (effective shear strength)	ϕ'	[^{o}]	20

Tab. 8: Soil Parameters for Method B using the Mohr Coulomb Model

Description	Symbol	Unit	Value
Unit weight	γ	[kN/m^3]	20
Effective young's modulus	E'	[kPa]	7500
Effective poisson's ratio	ν'	[-]	0.35
Cohesion (undrained shear strength)	c_u	[kPa]	18.79 *) with Δc = 5.67
Friction angle (undrained shear strength)	ϕ_u	[kPa]	0

*) Calculated from Equation 35

Tab. 9: Soil Parameters for Method C using the Mohr Coulomb Model

Description	Symbol	Unit	Value
Unit weight	γ	[kN/m^3]	20
Effective young's modulus	E_u	[kPa]	9375
Effective poisson's ratio	ν'	[-]	0.495
Cohesion (undrained shear strength)	c_u	[kPa]	18.79 *) with Δc = 5.67
Friction angle (undrained shear strength)	ϕ_u	[kPa]	0

*) Calculated from Equation 35

3.3.2 Calculation procedure

The calculations consist of three phases, the first phase is gravity loading, the second phase is staged construction (cutting the slope) and the third phase is phi-c-reduction. In the first phase, calculation of initial stress is carried out by using a plastic calculation and the weight multiplier is set from 0.0 to 1.0.

3.3.3 Results

Table 10 shows the calculated factors of safety (FOS) for all methods of undrained behaviour using the input parameters above. Figures 25 to 27 illustrate the computed failure mechanism for the three different cases and there are only marginal differences.

Tab. 10: Safety Factor obtained

Methods of Undrained Behaviour	FOS
Method A	2.47
Method B	2.36
Method C	2.35

From Table 10 it can be seen that the factors of safety for the cutting slope for all methods of modelling undrained behaviour are similar, however Method A delivers the highest factor of safety.

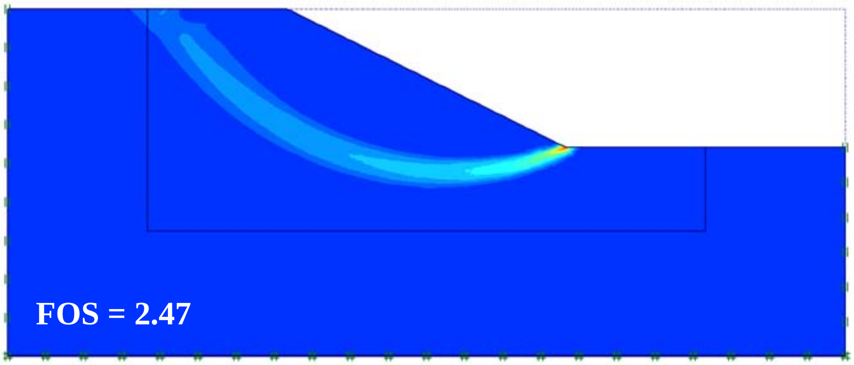

Fig. 25: Failure mechanism for Method A

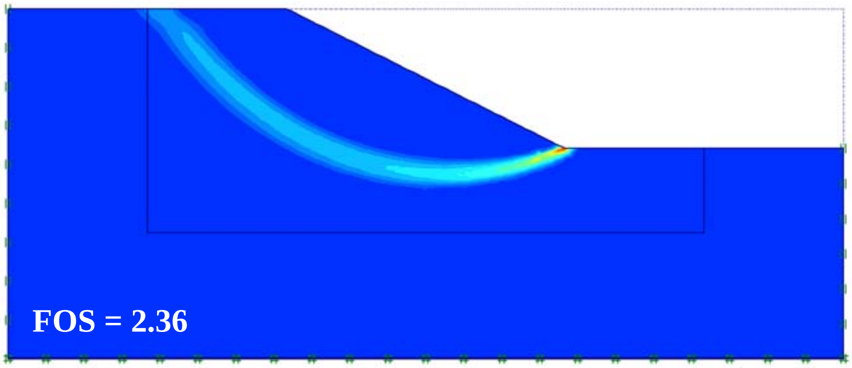

Fig. 26: Failure mechanism for Method B

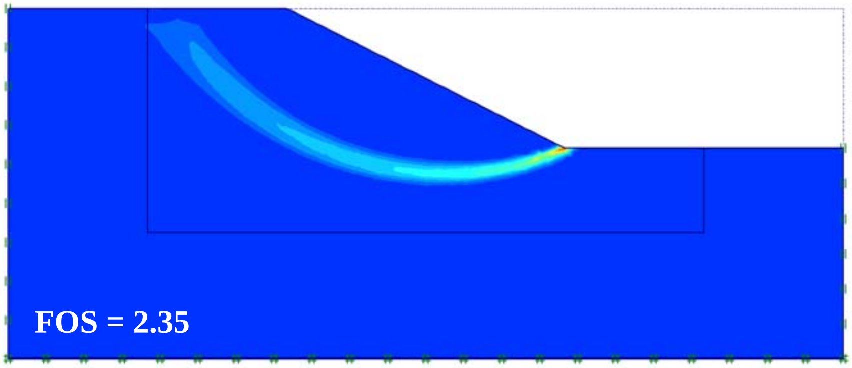

Fig. 27: Failure mechanism for Method C

Figure 28, 29 and 30 show the changes of the mean effective stress *p'* and the deviatoric stress *q* at three points of J, K, and L during the calculation for Method A, B, and C respectively. These points have a depth 2.65m, 4.28m, and 8.60m below surface. The deviatoric stresses at these points increase during cutting phase of the slope. During phi-c-reduction phase, these deviatoric stresses decrease until they reach constant values. In the Methods A and B, the mean effective stress at these points remain constant during cutting of the slope and phi-c-reduction phase. However, in the Method C, the mean stresses increase during cutting phase of the slope and decrease until reaching constant values during phi-c-reduction phase.

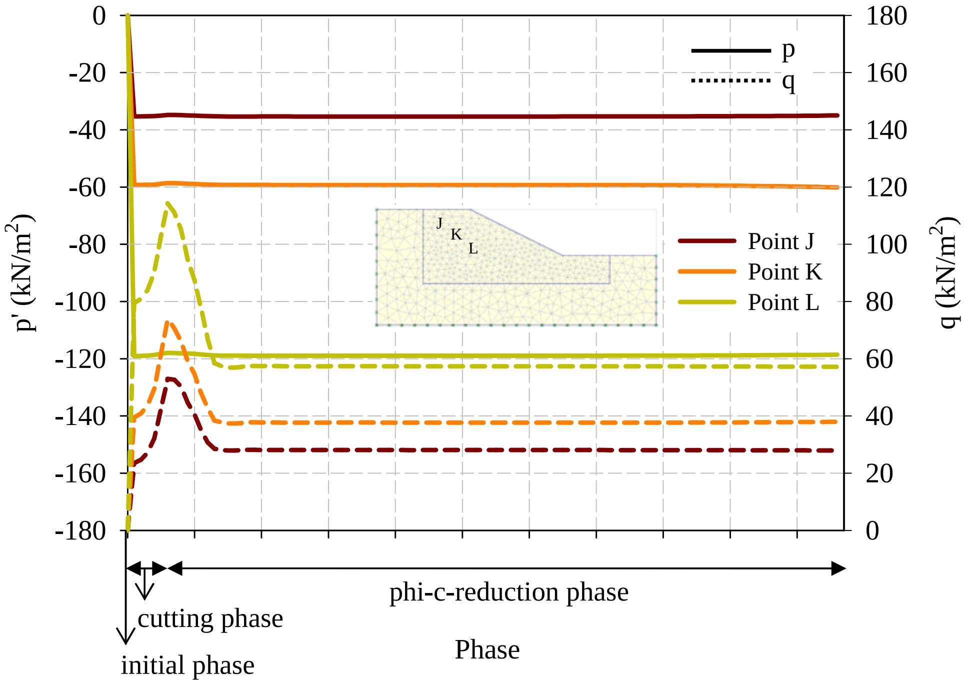

Fig. 28: The mean effective stress and the deviatoric stress during calculation (Method A)

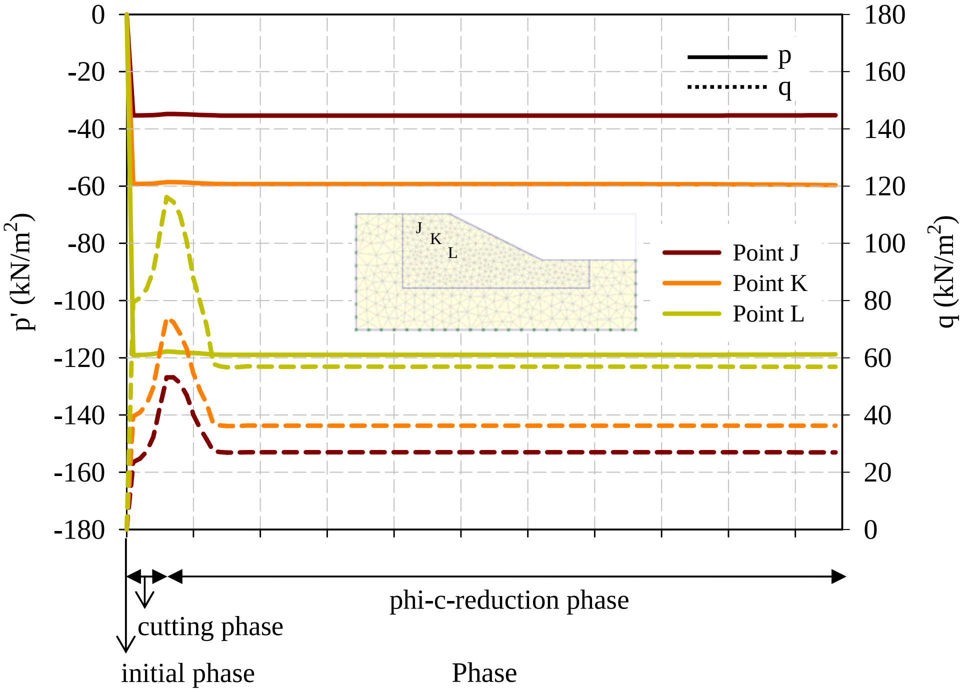

Fig. 29: The mean effective stress and the deviatoric stress during calculation (Method B)

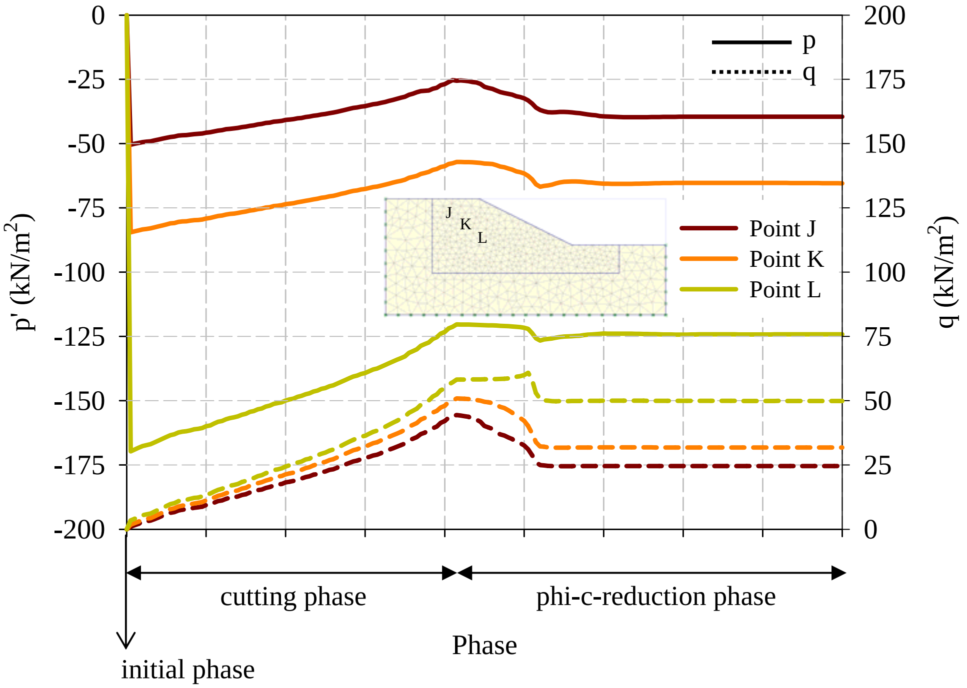

Fig. 30: The mean stress and the deviatoric stress during calculation (Method C)

The change of Mohr circles at points J, K, and L during calculation for Method A, B, and C are illustrated in Figures 31, 32, and 33 respectively. The Mohr circles grow during the cutting phase of the slope and shrink during phi-c-reduction phase until they remain constant at failure. It means that the effective horizontal stresses (σ'_{xx}) decreases and the effective vertical stresses (σ'_{yy}) increases during cutting of the slope. The effective horizontal stresses (σ'_{xx}) increase and the effective vertical stresses (σ'_{yy}) decrease during cutting of the slope.

The Mohr Coulomb line based on equation (3) with soil parameters c' = 20 kPa and φ' = 20^{o} is given by $\tau = 20 + \sigma' \tan 20^{o}$. This line will be tangent to the Mohr circle after cutting phase for Method A and B. This line is plotted in Figure 31, 32, and 33. Based on equation (35), the undrained cohesion (c_u) at point J, K, and L with these soil parameters are 32.73 kPa, 41.31 kPa, and 64.04 kPa respectively. These values are plotted in Figure 32 (Method B) and are equal to the diameter of the Mohr circles.

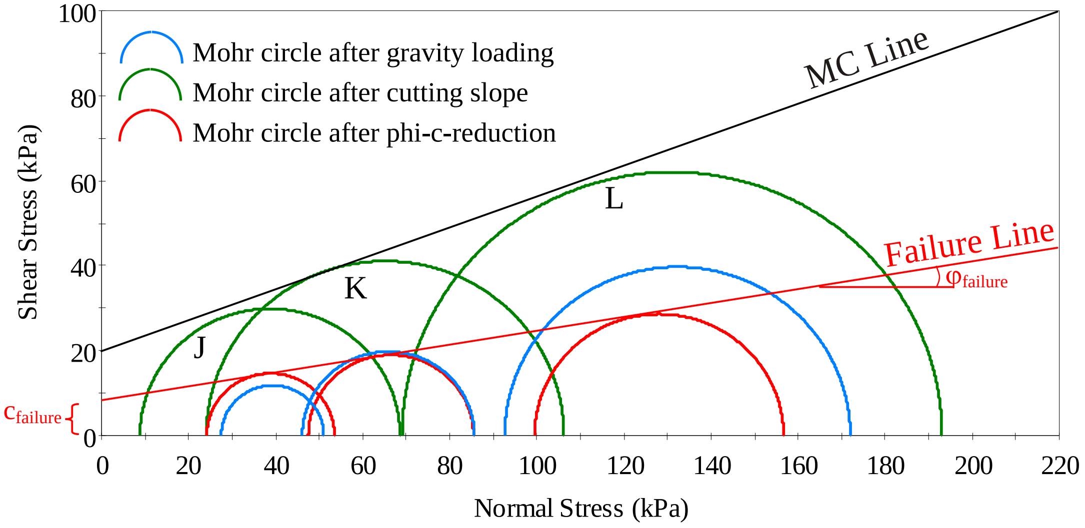

Fig. 31: Mohr circles during calculation for Method A

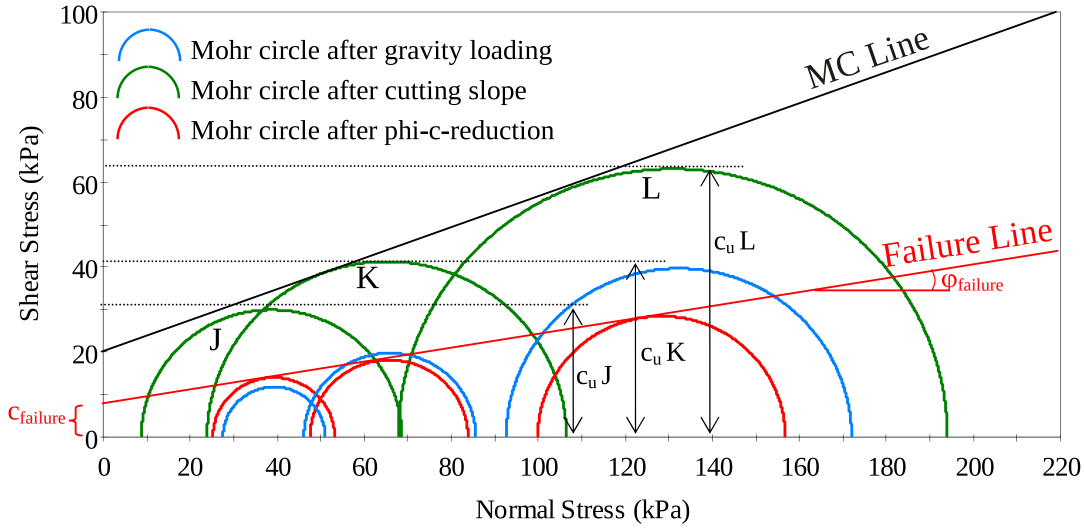

Fig. 32: Mohr circles during calculation for Method B

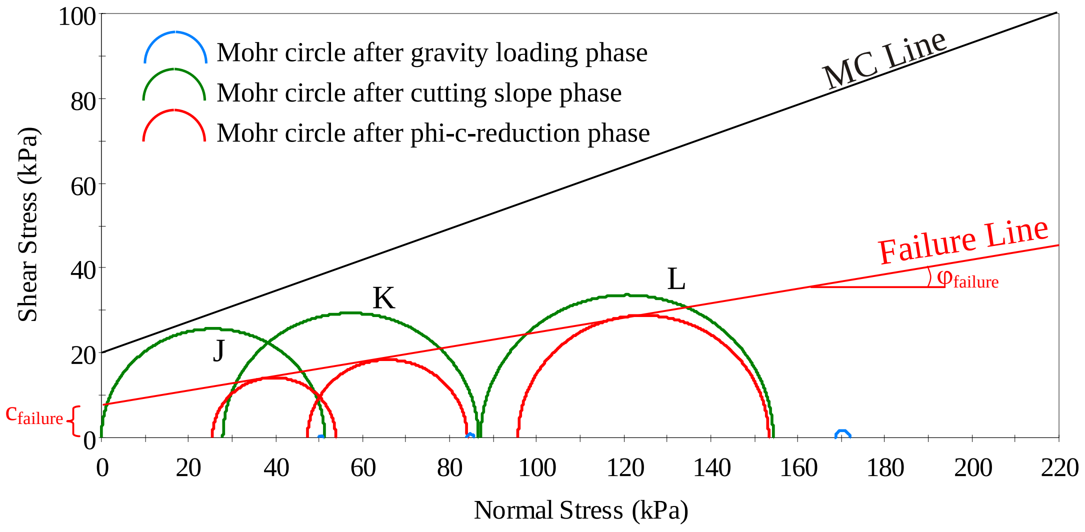

Fig. 33: Mohr circles during calculation for Method C

3.4 Summary

Three methods of modelling undrained behaviour (Method A, Method B and Method C) have been applied in analysing the factor of safety of a cutting slope. Obtained factors of safety are similar, but Method A delivers slightly higher factors.

4 Slope stability analysis considering strain softening behaviour

Generally, in slope stability analysis, a progressive failure can occur due to a reduction of strength with increasing strain. For strain softening materials, it cannot be assumed that the safety factor (FOS) greater than one based on peak shear strength means stability, because deformations may lead to a local loss of strength, requiring mobilization of additional strength at other points along the slip surface. This mechanism leads to additional movement and further strain softening. Therefore, if the peak strength is mobilized anywhere along the failure surface, a slope in strain softening materials is at risk of progressive failure.

Trancone (2005) employed an elasto-plastic constitutive model associated with a Mohr-Coulomb criterion considering the softening behaviour for the progressive reduction of the strength parameters with accumulated deviatoric plastic strain. The result showed that a progressive failure occurred due to excavation carried out at the toe of the slope.

A simplified method was developed by Zhang and Zhang (2007) to evaluate the stability level of a strain softening slope. The method was developed from the traditional methods of slices proposing a simplified strain compatibility equation. The result showed that the stability of a strain softening homogeneous slope is dependent on the strength parameters and the stress-strain relationship of the soil. The computed safety factor and the critical slip surface are between the ones calculated using the traditional slice method with the peak and the residual strength parameters, respectively.

A non-local elastoviscoplastic constitutive model within the finite element method framework is used by Conte et al. (2010) to analysis slope stability with strain softening behaviour. In this model, the Mohr-Coulomb yield function is adopted and the strength parameters are reduced with increasing deviatoric plastic strain to develop strain softening behaviour. With this model, the development of the shear zone of the slope at pre- and post-peak strength is generated by the deformation process.

This chapter examines slope stability analysis with strain softening behaviour and their comparison with the strength reduction approach. Analysis of slope stability was done by the finite element method using the Mohr Coulomb failure criterion and an advanced Multilaminate model. In this study, the Multilaminate model for soil, enhanced with a non-local formulation as regularisation method, and a simple Mohr Coulomb model in invariant formulation are compared.

The main objective of this section is to evaluate and to compare the failure mechanism of a simple slope obtained by a strain softening and strength reduction approach respectively and to check the influence of the stress path followed on the calculated factor of safety.

4.1 Multilaminate framework

4.1.1 General concept

In the multilaminate framework, it is assumed that the overall deformation of a soil body can be obtained from deformation on so-called sampling planes. By considering the balance between computational effort and calculation accuracy, 2x33 symmetric sampling planes are employed for all studies presented in this chapter.

Based on theory of plasticity, the plastic strain increment $\mathbf{d\varepsilon}_i^p$ is proportional to the derivative of the plastic potential function with respect to the stresses. The global plastic strain increment $\mathbf{d\varepsilon}^p$ can be obtained from the contributions of all sampling planes by transformation of the micro level plastic strain increment and the summation of the weighting coefficient of all sampling planes w_i:

$$\mathbf{d\varepsilon}^p = \sum_{i=1}^{n_{SP}} \mathbf{T}_i \mathbf{d\varepsilon}_i^p w_i \tag{37}$$

$\mathbf{T}_i$ is the transformation matrix of the sampling planes i and n_{SP} is the number of sampling planes on which the summation is taken.

The general concept of the multilaminate model in the framework of the finite element method is illustrated in Figure 34.

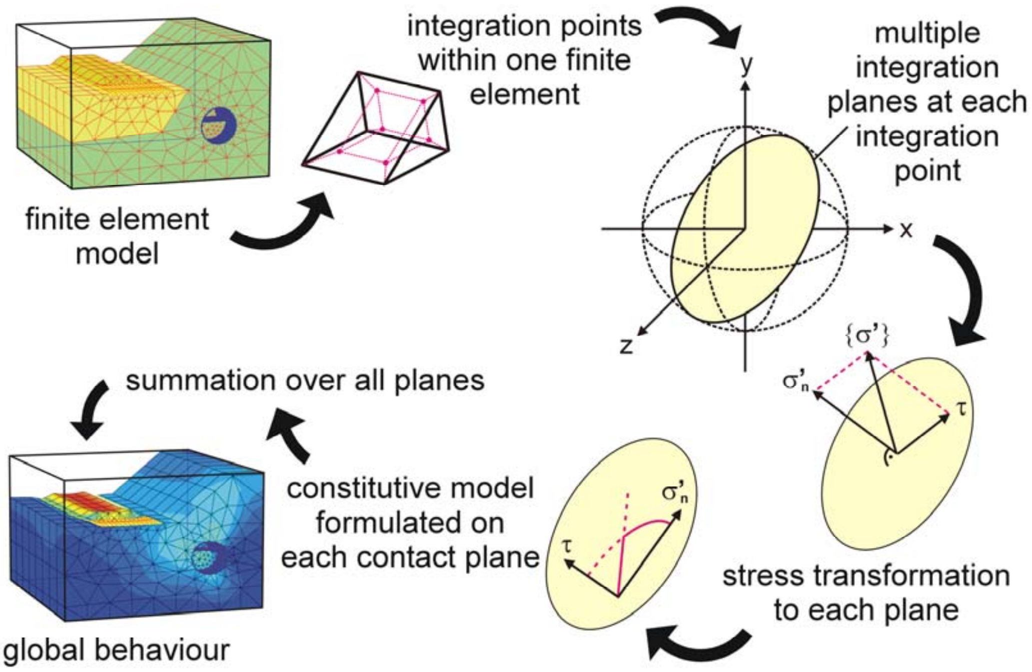

Fig. 34: General concept of Multilaminate models (Wiltafsky, 2003)

4.1.2 Non-local formulation for strain softening analysis

The basic model of the Multilaminate Model developed by Wiltafsky (2003) has been modified by Galavi (2007) considering a linear strain softening formulation. In this formulation, the peak strength on a plane is reached at a certain strain level ($\varepsilon_{di,\,peak}$) followed by softening to a residual value $\varepsilon_{di,\,res}$ (Figure 35).

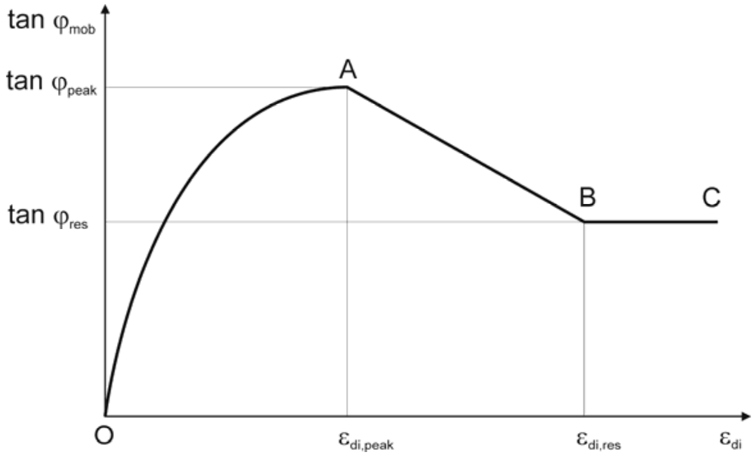

Fig. 35: Relation between mobilized friction angle and damage strain on each sampling plane

The accumulated damage strain on the sampling plane where the friction angle is fully mobilized, is represented by $\varepsilon_{di,\,peak}$ with the strength parameters φ'_{peak} and c'_{peak} (Figure 36)

The damage strain ε_{di} is a scalar quantity and a function of both plastic normal strain and plastic shear strain:

$$\varepsilon_{di} = (1 - A_d)\varepsilon_n^p + A_d \varepsilon_\gamma^p \tag{38}$$

where A_d is a non dimensional scaling parameter to control the relative proportion of distortional and volumetric contribution, ε_n^p is the plastic normal strain on a sampling plane and ε_γ^p is the plastic shear strain on sampling plane.

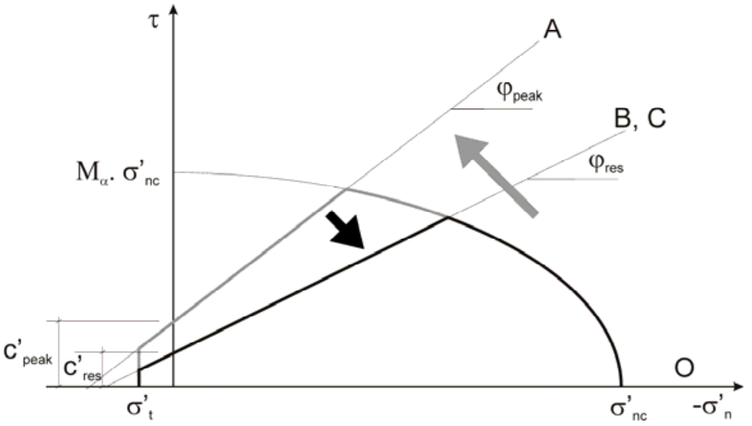

Fig. 36: Deviatoric hardening and softening on a sampling plane

Linear softening on integration planes is defined as:

$$\tan\varphi'_{mob} = -m_{soft,\varphi}\left(\varepsilon_{di} - \varepsilon_{di,peak}\right) + \tan\varphi'_{peak} \tag{39}$$

$$c'_{mob} = -m_{soft,c}\left(\varepsilon_{di} - \varepsilon_{di,peak}\right) + c'_{peak} \tag{40}$$

m_{soft} is the softening rate parameter that governs the reduction of the strength parameters on the sampling plane whereas in general cohesion degrades faster than the friction angle, which reaches residual values after significant plastic deformation. Consequently, two independent softening rate parameters for cohesion ($m_{soft,c}$) and friction angle ($m_{soft,\varphi}$) have been introduced into the model.

The relationship between these two softening rate parameters is given by:

$$m_{soft,\varphi} = \frac{\tan\varphi'_{peak} - \tan\varphi'_{mob}}{c'_{peak} - c'_{mob}} m_{soft,c} \tag{41}$$

4.1.3 Mesh dependency

Vahid and Schweiger (2010) evaluated the performance of the non-local Multilaminate model for strain softening analysis with respect to mesh dependency of results. In this evaluation, numerical simulation of two biaxial tests with friction and cohesion softening has been carried out. The evaluation revealed that the force-displacement curves obtained from the simulation of biaxial tests with different number of elements are very similar and the maximum difference between them is only 2.5% and 0.5% for friction softening and cohesion softening, respectively.

4.2 Numerical model

In this section, slope stability analyses will be carried out using four different methods to calculate the factor of safety (FOS):

1) Analysis with strain softening behaviour.
   In this method, slope stability analysis is carried out using the Multilaminate model with two different ratios between peak and residual strength (ratio of 1.1 and 1.3).

2) Analysis with reduced strength.
   In this method, slope stability analysis is carried out using the Multilaminate model with reduced strength from the start of analysis. This reduced strength is obtained from two different ratios between peak and residual strength (ratio of 1.1 and 1.3)

3) Analysis with strength reduction in a single step to residual.
   In this method, slope stability analysis is carried out using the Multilaminate model with peak strength in the beginning of calculation. After the limit state strength is reached, the material is changed to reduced strength. This leads to a stress state violating the strength criterion and thus to a redistribution of stresses. This reduced strength is also obtained from two different ratios between peak and residual strength (ratio of 1.1 and 1.3)

4) Analysis with “standard” strength reduction technique.
   In this method, slope stability analysis is carried out using the Mohr Coulomb model with the load obtained from the analysis with strain softening behaviour. The factor of safety is calculated by means of a phi-c-reduction.

4.2.1 Geometry, finite element mesh and material properties

A simple geometry of a slope with homogeneous soil has been chosen. The slope is 10 m high and has a 1:2 gradient (horizontal to vertical). The geometry and finite element mesh used are shown in Figure 37. 458 15-noded elements have been used.

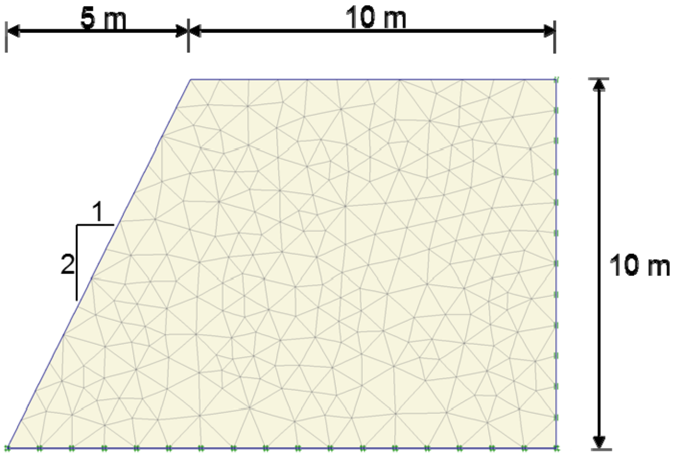

Fig. 37: Geometry and finite element mesh of slope (Conte *et al.*, 2010)

The soil parameters for the Mohr Coulomb and the Multilaminate model are given in Table 11 and Table 12.

Tab. 11: Soil Parameters for Mohr Coulomb Model

Description	Symbol	Unit	Value
Unit weight	γ	[kN/m^3]	20
Elasticity modulus	E’	[kPa]	10000
Poisson's ratio	ν'	[-]	0.35
Cohesion	c'	[kPa]	30
Friction angle	ϕ'	[^{o}]	35

Tab. 12: Soil Parameters for Multilaminate Model

Description	Symbol	Unit	Value
Unit weight	γ	[kN/m^3]	20
Reference oedometer modulus	$E_{oed_{ref}}$	[kPa]	10000
Reference young modulus for unloading and reloading	$E_{ur_{ref}}$	[-]	30000
Poisson's ratio	ν'	[-]	0.25
Peak cohesion	c'_{peak}	[kPa]	30
Peak friction angle	φ'_{peak}	[^{o}]	35
Reduced cohesion (ratio of 1.1)	$c'_{res1.1}$	[kPa]	27.27
Reduced friction angle (ratio of 1.1)	$\varphi'_{res1.1}$	[^{o}]	32.48
Reduced cohesion (ratio of 1.3)	$c'_{res1.3}$	[kPa]	23.08
Reduced friction angle (ratio of 1.3)	$\varphi'_{res1.3}$	[^{o}]	28.31
Softening rate parameter for cohesion	$m_{soft,\, c}$	[-]	2.75
Softening rate parameter for friction angle	$m_{soft,\, \varphi}$	[-]	0.064

4.2.2 Boundary conditions

In the analysis with the Multilaminate model, a prescribed displacement of 4 m width with a constant rate was imposed on the top of the slope. In Mohr Coulomb analysis, a load is imposed on the top surface (Figure 38). The amount of loading is obtained from the residual force of the result of the Multilaminate model considering strain softening behaviour.

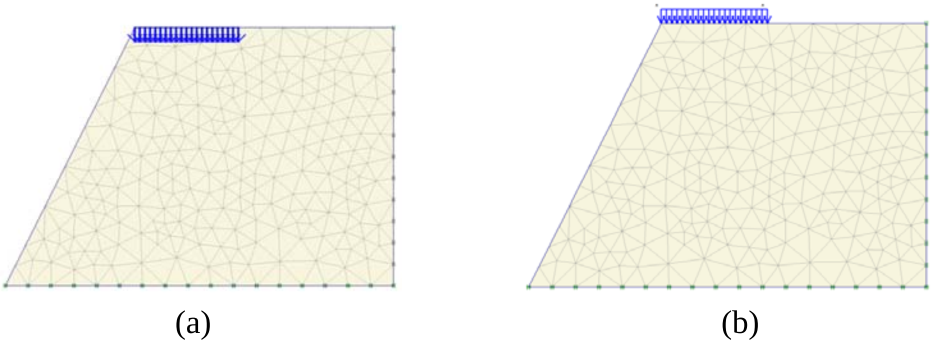
(a) (b)

Fig. 38: Loading conditions for the slope; (a) prescribed displacement input in Multilaminate Model; (b) load input in Mohr Coulomb Model

4.2.3 Calculation procedure

The calculation of slope stability using the Multilaminate model with strain softening consists of three phases. The first calculation phase is to generate the initial stress. The K0-procedure of PLAXIS cannot be used to generate initial stresses, because the geometry contains a non-horizontal soil surface. So the calculation of initial stress is performed by applying gravity. The second calculation phase is the activation of prescribed displacements by plastic calculation with staged construction. In the third calculation phase the total multiplier is set to reach a certain value of deformation.

The calculation of slope stability using the Mohr Coulomb model also consists of three phases. The first calculation phase is to generate the initial stress applying gravity. The second calculation phase is activation of the load. The third calculation phase is to calculate the safety factors in drained conditions which is carried out using the phi-c-reduction technique.

4.2.4 Results

Analysis with strain softening behaviour

Figure 39 shows that the computed force-displacement curves at all control points (A, B, C) are identical. Analysis with strain softening analysis using ratio 1.1 show that the peak strength is reached at the total displacement 0.24m. During strain softening, the mobilised friction angle φ'_{mob} decreases until the residual state is reached at approximately 0.4m of total displacement. The average residual force at the surface of the slope is equal to 370.4 kN/m or 92.6 kN/m^2 (along 4m at the surface).

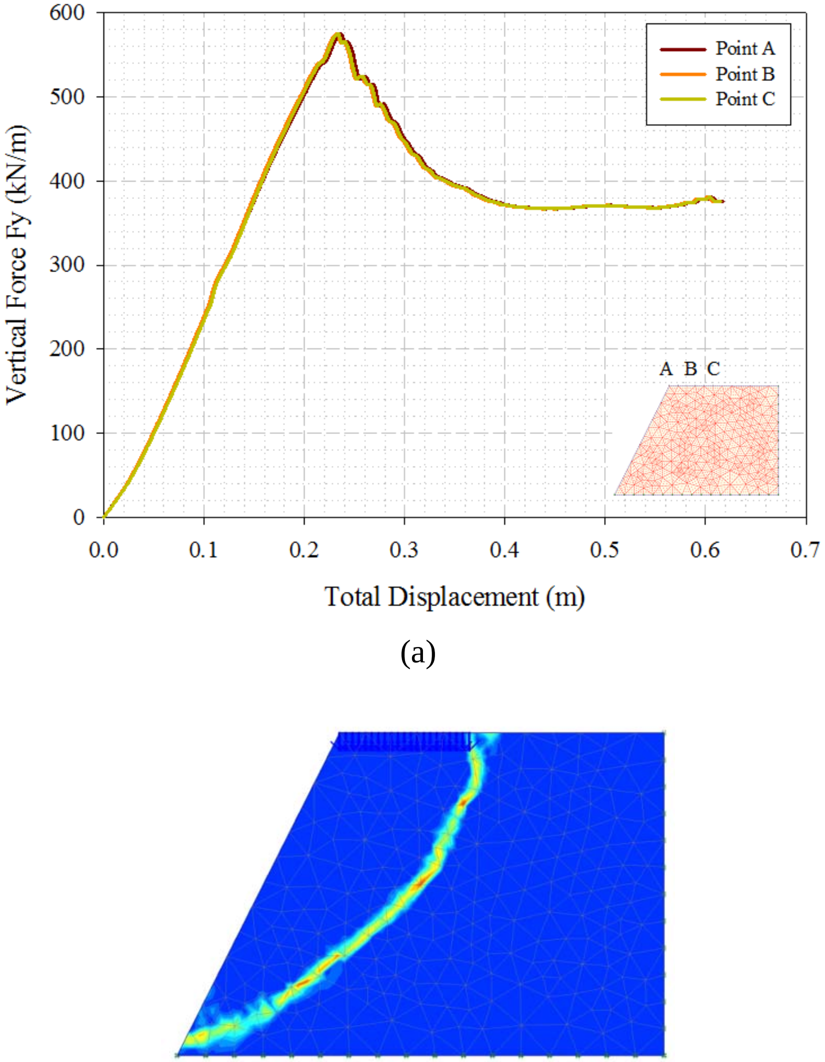

(a)

(b)

Fig. 39: Slope stability analysis with strain softening behaviour (ratio of 1.1); (a) force-displacement curve; (b) failure mechanism at residual state

Figure 40 shows similar results obtained from analysis with strain softening analysis using ratio 1.3. The peak strength is reached at the total displacement of 0.24m and residual state is reach at approximately 0.45m of total displacement. The average residual force is equal to 231.39 kN/m or 57.8 kN/m^2 (along 4m at the surface).

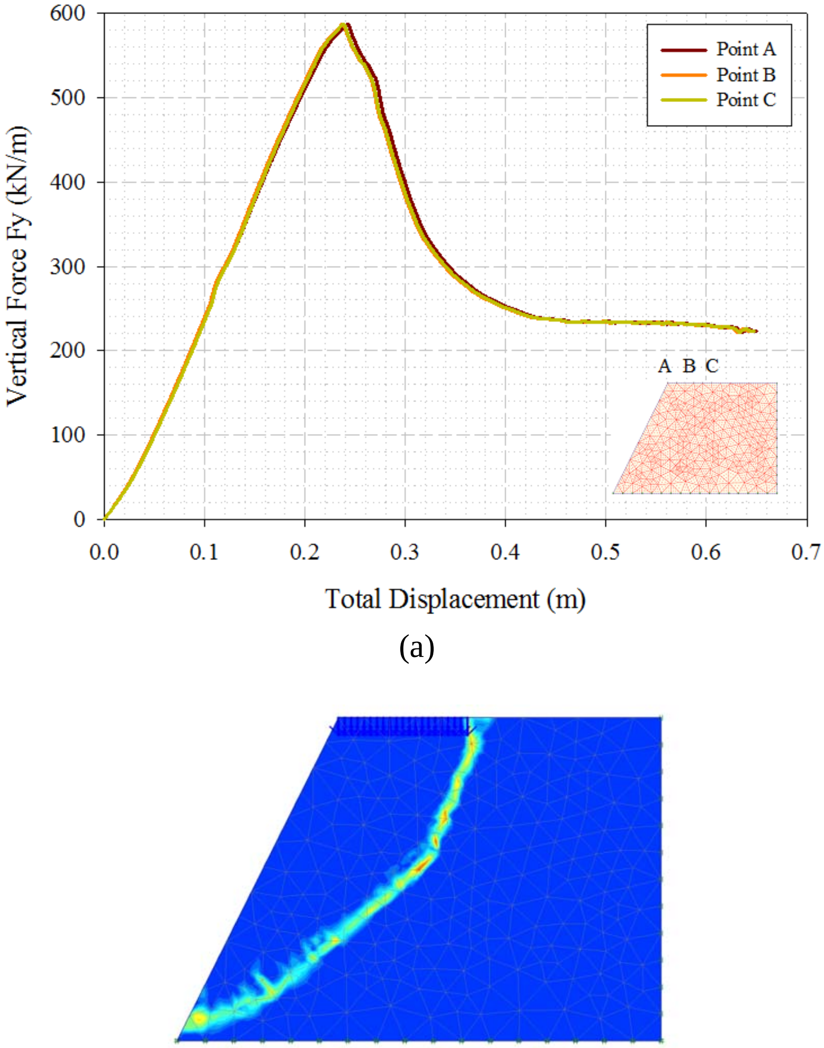

(a)

(b)

Fig. 40: Slope stability analysis with strain softening behaviour (ratio of 1.3); (a) force-displacement curve; (b) failure mechanism at residual state

Both of the above analysis used the same rate of softening, hence the total displacements are similar. The rate of softening will influence the total displacement at the peak strength and residual state.

Analysis with reduced strength

All control points (A, B, C) have a similar result in computed force-displacement curves (Figure 41). Analysis with reduced strength using ratio 1.1 illustrates that the residual state is reached at approximately 0.2m of total displacement with an average residual force of 380 kN/m.

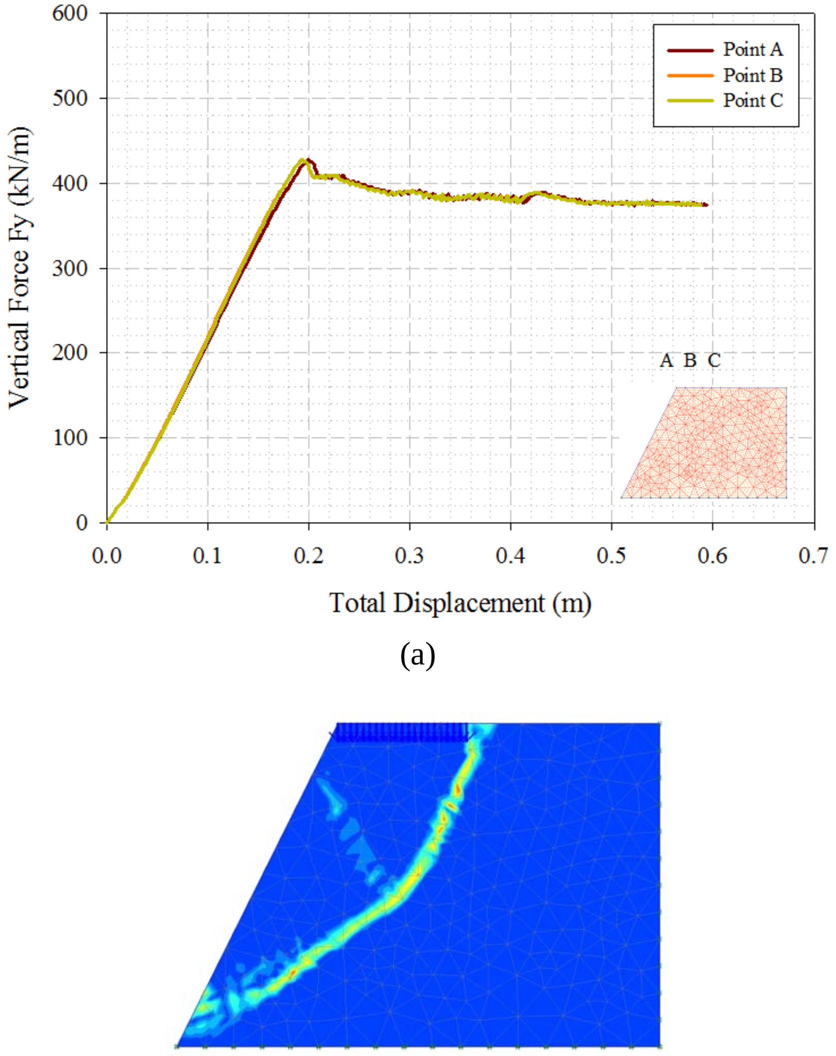

(a)

(b)

Fig. 41: Slope stability analysis with reduced strength (ratio of 1.1); (a) force-displacement curve; (b) failure mechanism at residual state

Figure 42 illustrates the force-displacement curve for the analysis with reduced strength using ratio 1.3. The residual state is reached at 0.15m of total displacement with average residual force of 205 kN/m.

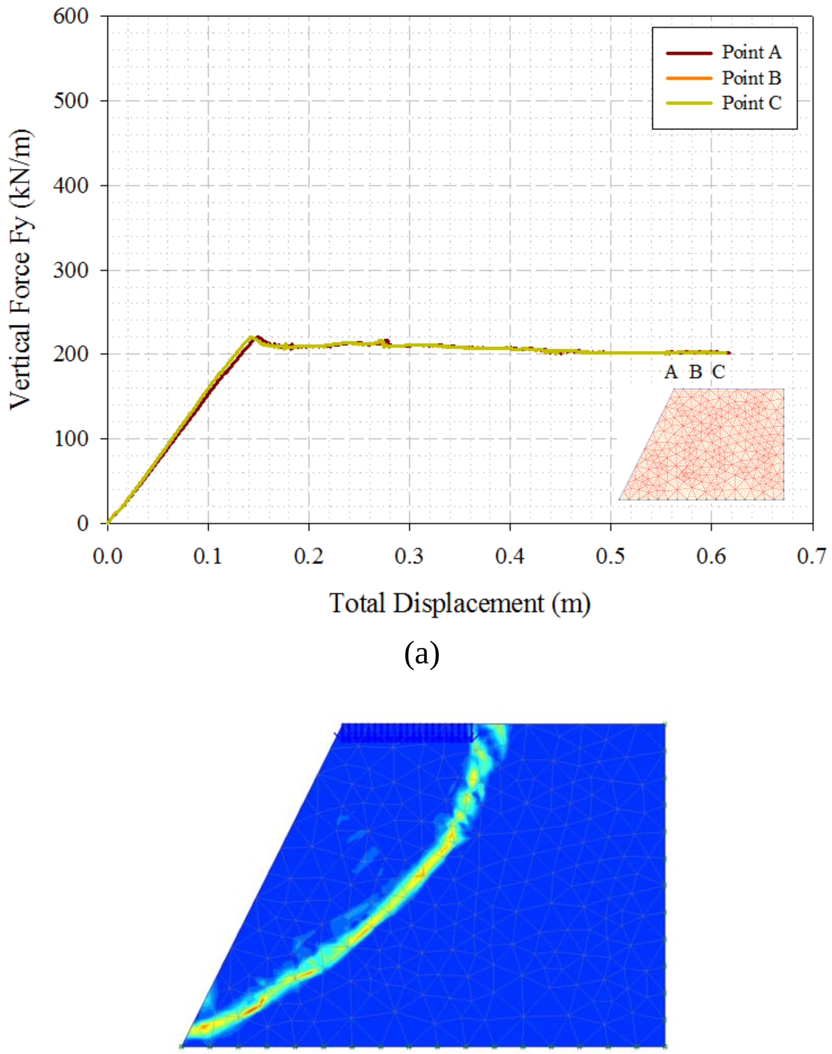

(a)

(b)

Fig. 42: Slope stability analysis with reduced strength (ratio of 1.3); (a) force-displacement curve; (b) failure mechanism at residual state

Analysis with strength reduction in a single step to residual

Figure 43 shows the force-displacement curve from the analysis with strength reduction in a single step to residual with a ratio of 1.1. It illustrates that at 0.23m of total displacement, the peak strength is reached and decreases rapidly to residual state with an average residual force of 382 kN/m.

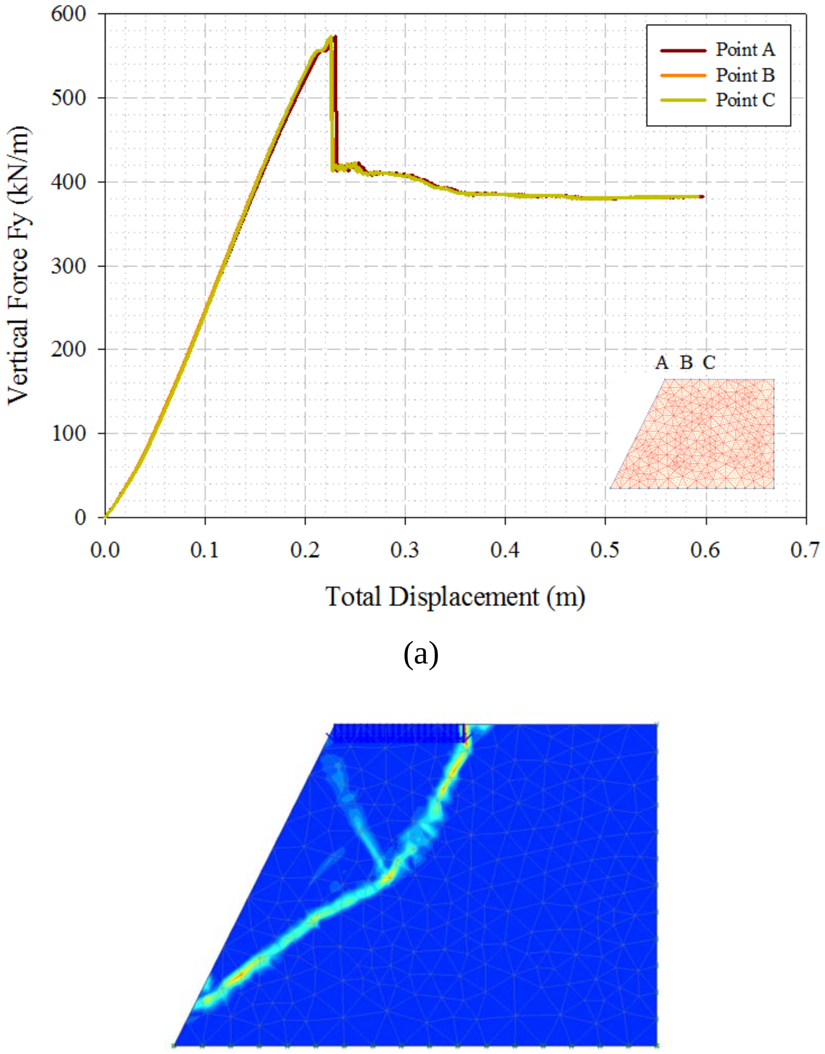

(a)

(b)

Fig. 43: Slope stability analysis with strength reduction in a single step to residual (ratio of 1.1); (a) force-displacement curve; (b) failure mechanism at residual state

Figure 44 illustrates similar results obtained from the analysis with strength reduction in a single step to residual with a ratio of 1.3. The peak strength is reached at 0.23m of total displacement and rapidly reduced to residual state with an average residual force of 205 kN/m.

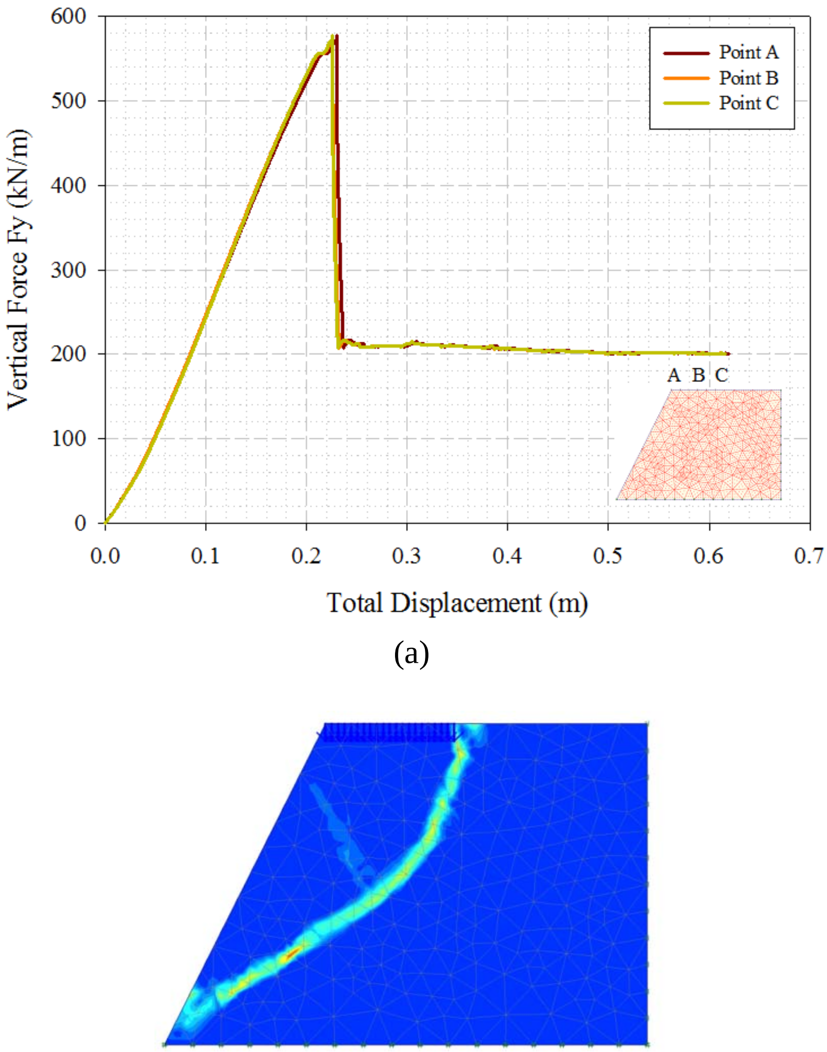

(a)

(b)

Fig. 44: Slope stability analysis with strength reduction in a single step to residual (ratio of 1.3); (a) force-displacement curve; (b) failure mechanism at residual state

Analysis with “standard” strength reduction technique

In the analysis with strain softening using the Multilaminate model with a ratio equal to 1.1, the residual vertical force at the surface of the slope is equal to 370.4 kN/m or 92.6 kN/m2 (load along 4m at the surface). This value is applied as a load in the Mohr Coulomb model and gives a FOS of 1.08. When the ratio is increased to 1.3, the residual vertical force at the surface of the slope is equal to 231.30 kN/m or 57.8 kN/m2 (load along 4m at the surface). If this value is applied as a load in the Mohr Coulomb model, a FOS of 1.21 is obtained. The failure mechanism of the slopes in this analysis is illustrated in Figure 45. It should be mentioned that due to the formulation of the Multilaminate model, the strength is slightly higher as compared to the Mohr Coulomb model (with the some value for φ’) and therefore some differences have to be expected.

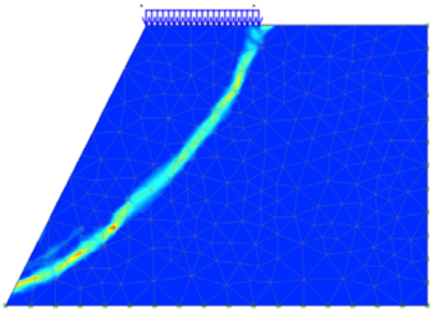

(a)

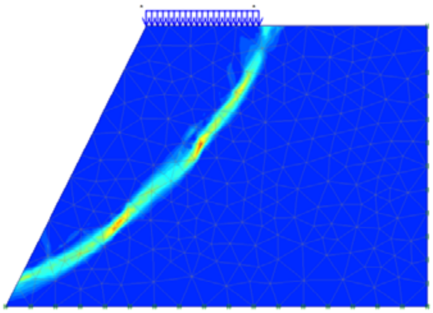

(b)

Fig. 45: Analysis with “standard” strength reduction technique; (a) failure mechanism of the slope with load 82.2 kN/m^2; (b) failure mechanism of the slope with load 57.8 kN/m^2

4.3 Summary

By applying the same ratio between peak and reduced strength (R) using the Multilaminate Model, almost identical residual vertical forces are obtained whatever method is used (strain softening, reduced strength and change of strength in one step). The difference is only 2.5% with ratio of 1.1 and 11% with ratio of 1.3.

All four different methods of calculation of the safety factor investigated (Multilaminate model with strain softening, Multilaminate model with reduced strength, Multilaminate model with change of strength in one step and Mohr Coulomb with strength reduction technique) seem to convergence to similar failure mechanisms and factors of safety. Figures 46 and 47 show that force displacement curve for the analysis using the Multilaminate model with ratios of 1.1 and 1.3, respectively.

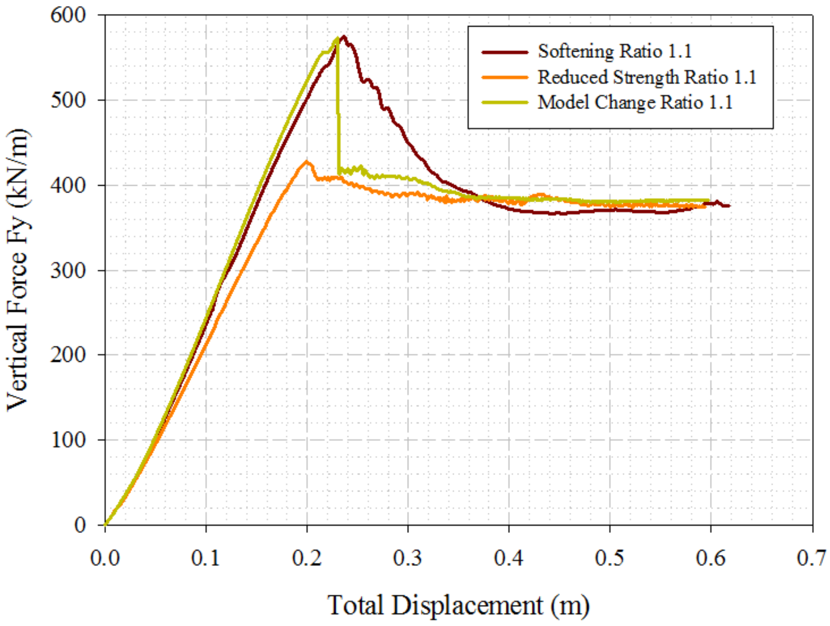

Fig. 46: Summary of analysis using Multilaminate model with ratio 1.1

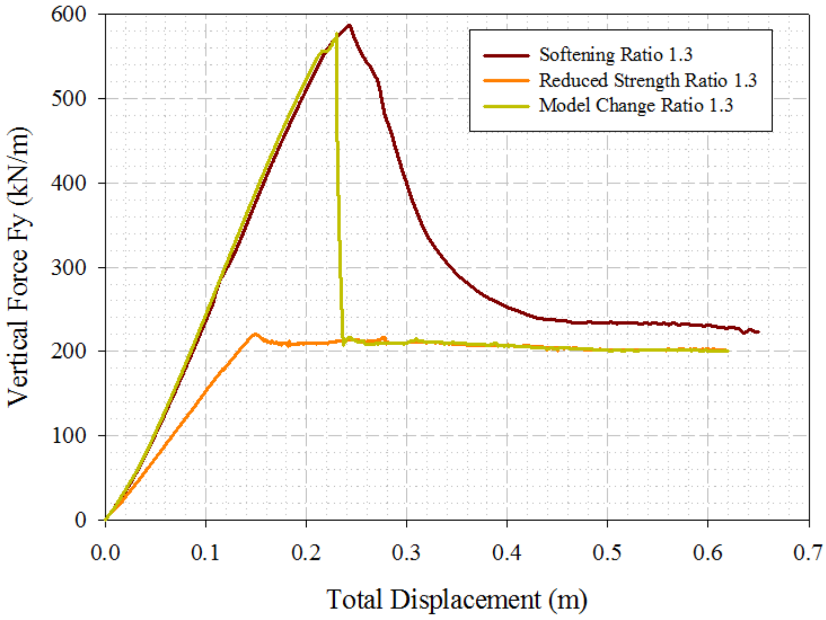

Fig. 47: Summary of analysis using Multilaminate model with ratio 1.3

The safety factor obtained with the strength reduction technique obtained from the Mohr-Coulomb failure criterion is close to the ratio between peak and residual strength in the Multilaminate model with strain softening behaviour. Based on these studies it could be concluded (at least for such simple cases as considered here) that the stress paths followed are not crucial for calculating failure mechanisms and factors of safety. However, it is pointed out that only drained conditions and Mohr Coulomb type failure criteria have been considered in this study.

5 Slope stability analysis considering unsaturated soil behaviour

Rainfall is one of the main factors causing slope failures. Rainfall induced slope failures are common problems in steep residual soil slopes in the tropics. The characteristics of water flow, change of pore-water pressure, and shear strength of soils are the main parameters associated with slope stability analysis involving unsaturated soils which are directly affected by the flux boundary condition (infiltration, evaporation) at the soil-atmosphere interface. Residual soils frequently exist in an unsaturated state. Generally, unsaturated residual soil slope failures happen most frequently during rain periods. The infiltration of rainfall will increase the groundwater level and water pressure and decrease matric suction of unsaturated soils.

In slope stability analysis, the effect of negative pore water pressure or suction is usually not taken into account because suction will reduce with rainfall infiltration and therefore it can be assumed that matric suction does not influence the long term stability of the slope. However, to reduce matric suction from the soil, the rainfall needs to be sustained over a significant time period and also the rainfall intensity needs to approximate the saturated coefficient of permeability of the soil at the ground surface. Hydraulic characteristics such as saturated coefficient of permeability and initial degree of saturation, intensity and duration of rainfall (Rahardjo *et al.*, 2001, 2007) are parameters which are important in the analysis of slope stability considering rain infiltration. The location of the groundwater table also influences the stability of unsaturated slope as illustrated by Rahardjo *et al*. (2010).

The main objective of this chapter is to evaluate the effects of hydraulic characteristics of soils (hydraulic conductivity and initial degree of saturation) and rainfall in slope stability calculations performed with the finite element method, simultaneously computing deformation and ground-water flow with time dependent boundary conditions (fully coupled flow-deformation analysis). The factor of safety is calculated by means of the shear strength reduction technique. As only ultimate limit states are concerned here, the linear elastic-perfectly plastic Mohr Coulomb constitutive model is employed.

5.1 A brief review on unsaturated soil slopes

Ng and Shi (1998) investigated the effect of numerous rainfall events, initial ground water table and boundary conditions on transient seepage and thus slope stability in unsaturated soils using the finite element method. Infiltration of rainfall caused a decrease of matric suction and an increase in moisture content and hydraulic conductivity in the unsaturated soil. The intensity and duration of rainfall, initial ground water table and hydraulic conductivity are the parameters that significantly influence in slope stability analysis.

Gasmo et al. (2000) used numerical models to illustrate the influence of infiltration on the slope stability through the combined use of seepage and slope stability analysis. The numerical models showed that the matric suction increased over time due to the applied evaporation, and then decreased over time due to the applied infiltration. In slope stability analysis, the factor of safety increases slowly due to evaporation and decreases rapidly due to infiltration. Better description of the soil parameters such as the hydraulic characteristic are required to improve the accuracy of unsaturated slope stability analysis.

Cho and Lee (2001) used the finite element method with flow-deformation coupled analysis to improve the understanding of actual mechanism of the slope failures within a soil mass during rainfall infiltration. The pore water pressure distribution that affected the stress fields is controlled by the spatial variation of hydraulic conductivity during rainfall infiltration. Even though the soil slope was homogeneous, the actual hydraulic conductivity showed inhomogeneous distribution, because the hydraulic conductivity is a function of the water content or the matric suction of an unsaturated soil.

Cai and Ugai (2004) investigated the effect of hydraulic characteristics, initial degree of saturation, intensity and duration of rainfall on water pressure in slopes. The results show that these parameters had a significant influence on the water pressure in slopes and thus on the stability of slopes under rainfall infiltration. The factor of safety of slopes will increase if the shear strength added by the matric suction was taken into consideration, but the influence of the matric suction decreased and at last disappeared when the soil was saturated by the infiltration of rainfall.

An analytical parametric study has been carried out to investigate the effect of hydraulic properties and rainfall conditions on rainfall infiltration mechanism in single and two-layer unsaturated soil system by Zhan and Ng, 2004. The results showed that the effects of desaturation coefficient and saturated permeability on pore-water pressure response are more significant than the effect of water storage capacity.

Zhang et al. (2004) illustrated that under certain conditions soil suction can be taken into account in slope stability analysis. The analysis shows that under steady state conditions, the intensity of rainfall expressed as a proportion of saturated hydraulic conductivity is the main parameter that influences the matric suction near the ground surface. However, under transient conditions, the intensity of rainfall, the saturated hydraulic conductivity and the water storage function are the parameters that affect the matric suction profile. When the intensity of rainfall is equal to or greater than the saturated hydraulic conductivity, the saturated hydraulic conductivity effectively turns into the upper limit of infiltration rate.

Griffiths and Lu (2005) analyzed unsaturated slope stability using elasto-plastic finite element analysis. The results showed that the suction above the ground water table will increase the factor of safety of a slope for different soil types and infiltration rate. The suction stress profile depends on three soil parameters, the saturated hydraulic conductivity, the pore size parameters, and a steady infiltration or evaporation rate.

5.2 Unsaturated groundwater flow

5.2.1 Darcy's Law

The water flow in a saturated soil is generally described using Darcy's law (1856). He assumed that the rate of water flow through a soil mass is proportional to the hydraulic gradient. The equilibrium for the groundwater flow can be expressed by the following equation:

$$\nabla p_w + \rho_w \underline{g} + \underline{\varphi} = 0 \tag{42}$$

where $\underline{g}$ is the vector of gravitational acceleration $(0, -g, 0)^T$ and $\underline{\varphi}$ is the vector of the friction force, per unit volume, between the flowing fluid and the soil skeleton. The friction force is linearly dependent on the velocity of the fluid and acts in opposite direction, which can be expressed by the following equation:

$$\underline{\varphi} = -\underline{\underline{m}}^{\text{int}} \underline{q} \tag{43}$$

where $\underline{q}$ is the velocity of the fluid (the specific discharge), and

$$\underline{\underline{m}}^{\text{int}} = \begin{vmatrix} \frac{\mu}{\kappa_x} & 0 & 0 \\ 0 & \frac{\mu}{\kappa_x} & 0 \\ 0 & 0 & \frac{\mu}{\kappa_x} \end{vmatrix} \tag{44}$$

With μ is the dynamic viscosity of the fluid and κ_x is the intrinsic permeability of the porous medium.

∇p_w is the gradient of the water pore pressure which causes groundwater flow. The term $\rho_w g$ is used as the flow is not affected by the gradient of the water pore pressure in vertical direction when hydrostatic conditions are assumed.

Substituting equation (44) to equation (42) yields:

$$\nabla p_w + \rho_w \underline{g} - \underline{\underline{m}}^{\text{int}} \underline{q} = 0 \tag{45}$$

which can be also expressed as:

$$\underline{q} = \frac{1}{\underline{\underline{m}}^{\text{int}}} \left(\nabla p_w + \rho_w \underline{g} \right) \tag{46}$$

or

$$\underline{q} = \underline{\underline{k}}^{\text{int}} \left(\nabla p_w + \rho_w \underline{g} \right) \tag{47}$$

where:

$$\underline{\underline{k}}^{\text{int}} = \begin{bmatrix} \frac{\kappa_x}{\mu} & 0 & 0 \\ 0 & \frac{\kappa_x}{\mu} & 0 \\ 0 & 0 & \frac{\kappa_x}{\mu} \end{bmatrix} \tag{48}$$

The coefficient of permeability ($\underline{\underline{k}}^{sat}$) in soil mechanics is used as a substitute of both intrinsic permeability and viscosity, which can be expressed by the following equation:

$$\underline{\underline{k}}^{sat} = \rho_w g \frac{\kappa_i}{\mu} \tag{49}$$

where $i = x, y, z$, or written alternatively as:

$$\underline{\underline{k}}^{sat} = \rho_w g \underline{\underline{k}}^{\text{int}} \tag{50}$$

with

$$\underline{\underline{k}}^{\text{int}} = \frac{\underline{\underline{k}}^{sat}}{\rho_w g} \tag{51}$$

where $\underline{\underline{k}}^{sat}$ is the saturated permeability matrix.

$$\underline{\underline{k}}^{sat} = \begin{bmatrix} k_x^{sat} & 0 & 0 \\ 0 & k_y^{sat} & 0 \\ 0 & 0 & k_z^{sat} \end{bmatrix} \tag{52}$$

Substituting equation (51) to equation (47) yields:

$$\underline{q} = \frac{\underline{\underline{k}}^{sat}}{\rho_w g}\left(\nabla p_w + \rho_w \underline{g}\right) \tag{53}$$

Equation (53) is the saturated flow in the porous medium. The coefficient of permeability in an unsaturated state depends on the saturation of soils. The relative permeability k_{rel} (S) is defined as the ratio of the permeability at a given saturation to the permeability in the saturated state. Hence, the unsaturated flow in the porous medium is:

$$\underline{q} = \frac{\underline{\underline{k}}}{\rho_w g}\left(\nabla p_w + \rho_w \underline{g}\right) \tag{54}$$

where

$$\underline{\underline{k}} = k_{rel}\,\underline{\underline{k}}^{sat} \tag{55}$$

5.2.2 Compressibility of water

The compressibility of water for unsaturated groundwater flow can be defined as follows (Bishop & Eldin, 1980; Fredlund & Rahardjo, 1993):

$$\beta = S\beta_w + \frac{1 - S + hS}{K_{air}} \tag{56}$$

where S is the degree of saturation, β_w is the compressibility of pure water (4.58×10^{-7} kPa^{-1}), h is the volumetric coefficient of air solubility (0.02), and K_{air} is the bulk modulus of air (100 kPa at atmosphere pressure).

By neglecting the air solubility, the equation can be simplified as follows (Verruijt, 2001):

$$\beta = S\beta_w + \frac{1 - S}{K_{air}} \tag{57}$$

5.2.3 Continuity equation

In the mass continuity equation of the water, the water outflow from the volume is equal to the changes in the mass concentration. The mass concentration of water in each elemental volume of the medium is equal to $\rho_w nS$. While water outflow is the divergence of the specific discharge $\nabla^T q$, consequently the continuity equation has the form (Song, 1990):

$$\nabla^T \left[\rho_w \frac{k_{rel}}{\rho_w g} \underline{\underline{k}}^{sat} \left(\nabla p_w + \rho_w \underline{g} \right) \right] = -\frac{\partial}{\partial_t} \left(\rho_w n S \right) \tag{58}$$

where n is the porosity of soil. The right hand side of Equation (58) can be written as:

$$-\frac{\partial}{\partial t} \left(\rho_w n S \right) = -\rho_w n \frac{\partial S}{\partial t} - nS \frac{\partial \rho_w}{\partial t} - \rho_w S \frac{\partial n}{\partial t} \tag{59}$$

where the first term denotes the changes in degree of saturation, the second term is the change of water density, and the last term is the change of soil porosity.

The first term of equation (59) has the form:

$$\rho_w n \frac{\partial S}{\partial t} = n \rho_w \frac{\partial S}{\partial p_w} \frac{\partial p_w}{\partial t} \tag{60}$$

Introducing the definition of water compressibility leads to:

$$\frac{1}{\rho_w} \frac{\partial \rho_w}{\partial t} = -\frac{1}{K_w} \frac{\partial p_w}{\partial t} \tag{61}$$

The second term of equation (59) can be expressed as:

$$nS \frac{\partial \rho_w}{\partial t} = nS \frac{\partial \rho_w}{\partial p_w} \frac{\partial p_w}{\partial t} = -nS \frac{\rho_w}{K_w} \frac{\partial p_w}{\partial t} \tag{62}$$

There are several factors that contribute to the term of the change of soil porosity. The first factor is the overall compression of soil structure caused by the combined action of the effective stress and the pore pressure:

$$-\frac{\partial \varepsilon_v}{\partial t} = -\underline{m}^T \frac{\partial \underline{\varepsilon}}{\partial t} \tag{63}$$

The second factor is the compression rate of the solid particles caused by the change of the pore pressure:

$$-\frac{(1-n)}{K_s}\frac{\partial p_w}{\partial t} \tag{64}$$

where K_s is the bulk modulus of the solid particles forming the soil skeleton. And the final factor is the compression of the solid particles caused by the change in effective stresses:

$$\frac{1}{3K_s}\underline{m}^T\underline{\underline{M}}\left(\frac{\partial \underline{\varepsilon}}{\partial t}-\frac{1}{3K_s}\frac{\partial p_w}{\partial t}\underline{m}\right) \tag{65}$$

Based on the equation (63), (64), and (65), the third term of equation (59) can be expressed as:

$$\rho_w S\frac{\partial n}{\partial t}=\rho_w S\left(\underline{m}^T\frac{\partial \underline{\varepsilon}}{\partial t}-\frac{(1-n)}{K_s}\frac{\partial p_w}{\partial t}-\frac{1}{3K_s}\underline{m}^T\underline{\underline{M}}\left(\frac{\partial \underline{\varepsilon}}{\partial t}-\frac{1}{3K_s}\frac{\partial p_w}{\partial t}\underline{m}\right)\right) \tag{66}$$

Substituting equation (60), (62), and (66) to equation (58) yields:

$$\nabla^T\left[\rho_w\frac{k_{rel}}{\rho_w g}\underline{\underline{k}}^{sat}\left(\nabla p_w+\rho_w\underline{g}\right)\right]+n\rho_w\frac{\partial S}{\partial p_w}\frac{\partial p_w}{\partial t}-nS\frac{\rho_w}{K_w}\frac{\partial p_w}{\partial t}+$$

$$\rho_w S\left(\underline{m}^T\frac{\partial \underline{\varepsilon}}{\partial t}-\frac{(1-n)}{K_s}\frac{\partial p_w}{\partial t}-\frac{1}{3K_s}\underline{m}^T\underline{\underline{M}}\left(\frac{\partial \underline{\varepsilon}}{\partial t}-\frac{1}{3K_s}\frac{\partial p_w}{\partial t}\underline{m}\right)\right)=0 \tag{67}$$

With neglecting the second order infinitesimal terms of the continuity equation, the equation (67) can be written as:

$$\nabla^T\left[\rho_w\frac{k_{rel}}{\rho_w g}\underline{\underline{k}}^{sat}\left(\nabla p_w+\rho_w\underline{g}\right)\right]+n\rho_w\frac{\partial S}{\partial p_w}\frac{\partial p_w}{\partial t}-$$

$$\rho_w S\left(\frac{n}{K_w}+\frac{(1-n)}{K_s}\right)\frac{\partial p_w}{\partial t}+\rho_w S\underline{m}^T\frac{\partial \underline{\varepsilon}}{\partial t}=0 \tag{68}$$

The continuity equation can be simplified by neglecting the deformations of solid particles and the gradient of water density (Boussinesq's approximation):

$$\nabla^T \left[\frac{k_{rel}}{\rho_w g} \underline{\underline{k}}^{sat} \left(\nabla p_w + \rho_w \underline{g} \right) \right] - n \left(\frac{S}{K_w} - \frac{\partial S}{\partial p_w} \right) \frac{\partial p_w}{\partial t} + S \underline{m}^T \frac{\partial \underline{\varepsilon}}{\partial t} = 0 \qquad (69)$$

where,

$\underline{m}^T$ = $(1 \ \ 1 \ \ 1 \ \ 0 \ \ 0 \ \ 0)$

K_w = the bulk modulus of water

In transient groundwater flow, the hydraulic head changes with respect to time. Changes are usually due to a change in the boundary conditions with respect to time. For transient conditions, equation (69) can be simplified by neglecting the displacement of solid particles, therefore the continuity equation is:

$$\nabla^T \left[\frac{k_{rel}}{\rho_w g} \underline{\underline{k}}^{sat} \left(\nabla p_w + \rho_w \underline{g} \right) \right] - n \left(\frac{S}{K_w} - \frac{\partial S}{\partial p_w} \right) \frac{\partial p_w}{\partial t} = 0 \qquad (70)$$

In steady state conditions the hydraulic head and the coefficient of permeability at any point in the soil mass remain constant with respect to time, that is the variation of pore pressure with respect to time is zero ($\partial p_w / \partial t = 0$). Consequently the continuity equation becomes:

$$\nabla^T \left[\frac{k_{rel}}{\rho_w g} \underline{\underline{k}}^{sat} \left(\nabla p_w + \rho_w \underline{g} \right) \right] = 0 \qquad (71)$$

5.2.4 Hydraulic models

Hydraulic parameters of the groundwater flow in unsaturated zones (above the phreatic surface) are described by the Soil Water Characteristics Curve (SWCC). The SWCC is an important hydraulic parameter for transient seepage analysis in unsaturated soils. The SWCC is a measure of the water storage capacity of the soil for a given soil suction (Ng and Pang, 2000). SWCC describes the capacity of the soil to keep water at different stresses. There are many models which describe the hydraulic behaviour of unsaturated soils. Van Genuchten (1980) presented the set of closed-form equations of hydraulic characteristics of unsaturated soils which is based on the capillary model of Mualem (1976). The Van Genuchten model introduces the relation between saturation and suction pore pressure head (ϕ_p):

$$S(\phi_p) = S_{res} + (S_{sat} - S_{res}) \left[1 + \left(g_a \left| \phi_p \right| \right)^{g_n} \right]^{g_c} \qquad (72)$$

where

$$\phi_p = -\frac{p_w}{\rho_w g} \tag{73}$$

p_w is the suction pore pressure, S_{res} is a residual saturation that describes a part of the fluid that remains in the pores even at high suction heads, S_{sat} is the saturation when the pores are filled with water, ρ_w is the density of water, and g is the gravity acceleration.

g_a, g_n, g_c are fitting parameters. g_a is a fitting parameter that is related to the air entry value of the soil and has to be measured for a specific material, g_n is a fitting parameter that is a function of the rate of water extraction from the soil once the air entry value has been exceeded and g_c is a fitting parameter which is used in the general Van Genuchten equation. It is assumed that:

$$g_c = \frac{1-g_n}{g_n} \tag{74}$$

When the Van Genuchten model is used the effective degree of saturation (S_e) is obtained as (Genuchten and Nielsen, 1985):

$$S_e = \frac{S - S_{res}}{S_{sat} - S_{res}} \tag{75}$$

The relative permeability k_{rel} (S) in relation to Mualem – Van Genuchten is:

$$k_{rel}(S) = (S_e)^{g_l}\left[1-\left(1-S_e^{\frac{g_n}{g_n-1}}\right)^{\frac{g_n-1}{g_n}}\right]^2 \tag{76}$$

where g_l is a fitting parameter that has to be measured for a specific material.

The derivative of the degree of saturation with respect to the suction pore pressure is:

$$\frac{\partial S(p_w)}{\partial p_w} = (S_{sat} - S_{res})\left[\frac{1-g_n}{g_n}\right]\left[g_n\left(\frac{g_a}{\gamma_w}\right)^{g_n} p_w^{(g_n-1)}\right]\left[1+\left(g_a\frac{p_w}{\gamma_w}\right)^{g_n}\right]^{\left(\frac{1-2g_n}{g_n}\right)} \tag{77}$$

Alternatively a model for the Soil Water Characteristic Curve (SWCC) based on adsorption, cavitation, and double porosity as presented by Frydman and Baker (2009) could be employed but this approach is not followed in this study. The Soil Water Characteristic Curve (SWCC) can be used to predict the unsaturated soil properties such as unsaturated coefficient of permeability and unsaturated shear strength as illustrated by Fredlund (1995, 2000), and Fredlund *et al.* (2011). Lu and Griffith (2004) developed the method to analyze the suction stress profiles based on the Soil Water Characteristic Curve (SWCC). Lu and Likos (2006) introduced the suction stress characteristic curve (SSCC) to describe the state of the stress in unsaturated soil.

Figures 48 and 49 illustrate the influence of the parameters g_a and g_n on the shape of the Soil Water Characteristics Curve (SWCC). The parameter g_a will influence the air entry value of the soil and the parameter g_n will influence the slope of the soil water characteristic curve.

Table 13 shows the hydraulic data of the USDA series for Van Genuchten models. The Soil Water Characteristics Curve (SWCC) and the suction-relative permeability curves of these data are illustrated in Figures 50 and 51, respectively.

Tab. 13: Hydraulic Data (USDA series with Van Genuchten Models)

Soil	k_{sat}	g_a	g_n	g_l
	[m/s]	[1/m]	[-]	[-]
Sand	8.3E-05	14.50	2.68	0.50
Loamy Sand	4.1E-05	12.40	2.28	0.50
Sandy Loam	1.2E-05	7.50	1.89	0.50
Loam	2.9E-06	3.60	1.56	0.50
Silt	6.9E-06	1.60	1.37	0.50
Silty Loam	1.3E-06	2.00	1.41	0.50
Sandy Clay Loam	3.6E-06	5.90	1.48	0.50
Clayey Loam	7.2E-06	1.90	1.31	0.50
Silty Clay Loam	1.9E-06	1.00	1.23	0.50
Sandy Clay	3.3E-06	2.70	1.23	0.50
Silty Clay	5.5E-08	0.50	1.09	0.50
Clay	5.5E-07	0.80	1.09	0.50

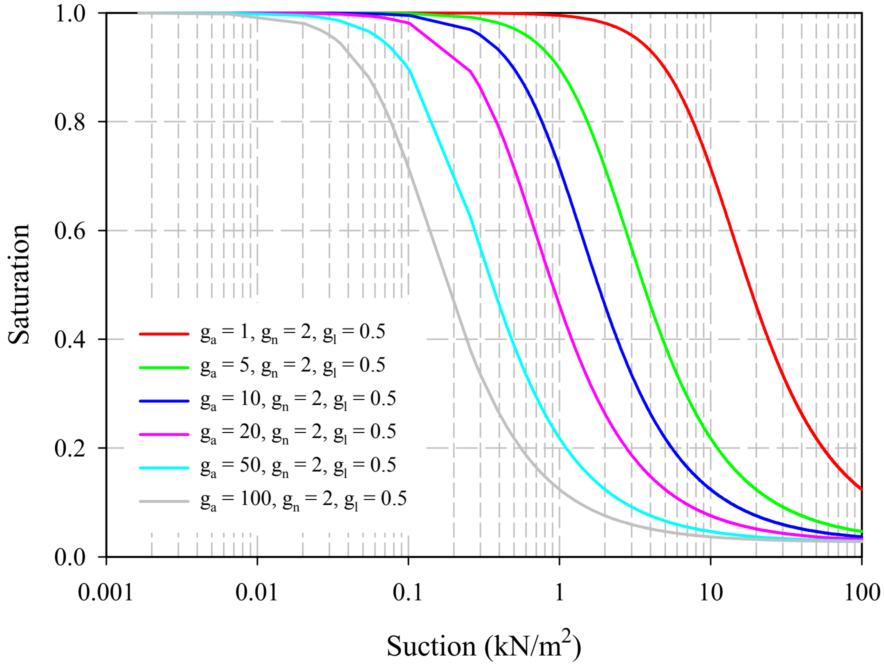

Fig. 48: Influence of the parameter g_a on the Soil Water Characteristic Curves (SWCC)

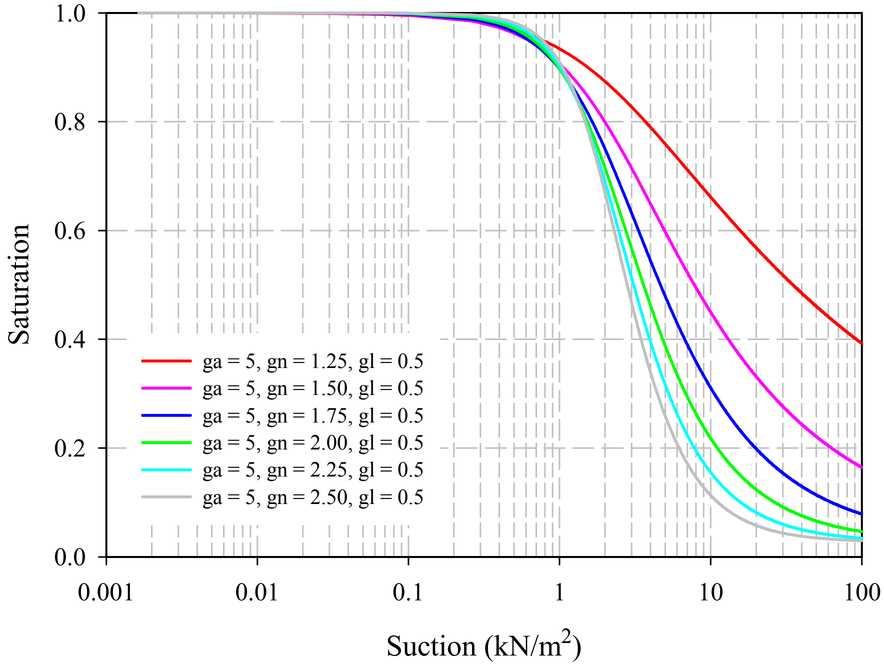

Fig. 49: Influence of the parameter g_n on the Soil Water Characteristic Curves (SWCC)

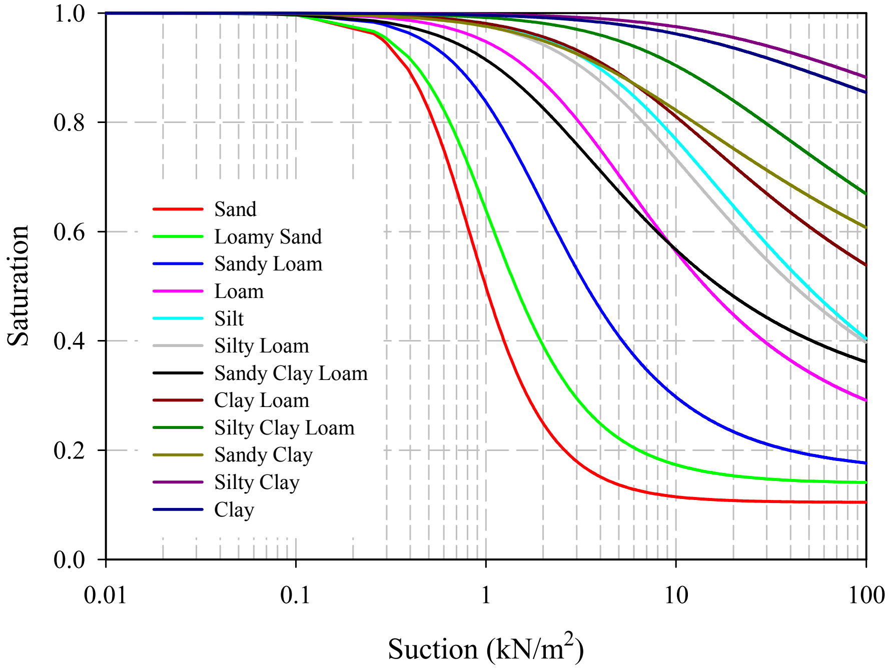

Fig. 50: Soil Water Characteristic Curves (SWCC) for USDA series with Van Genuchten Models

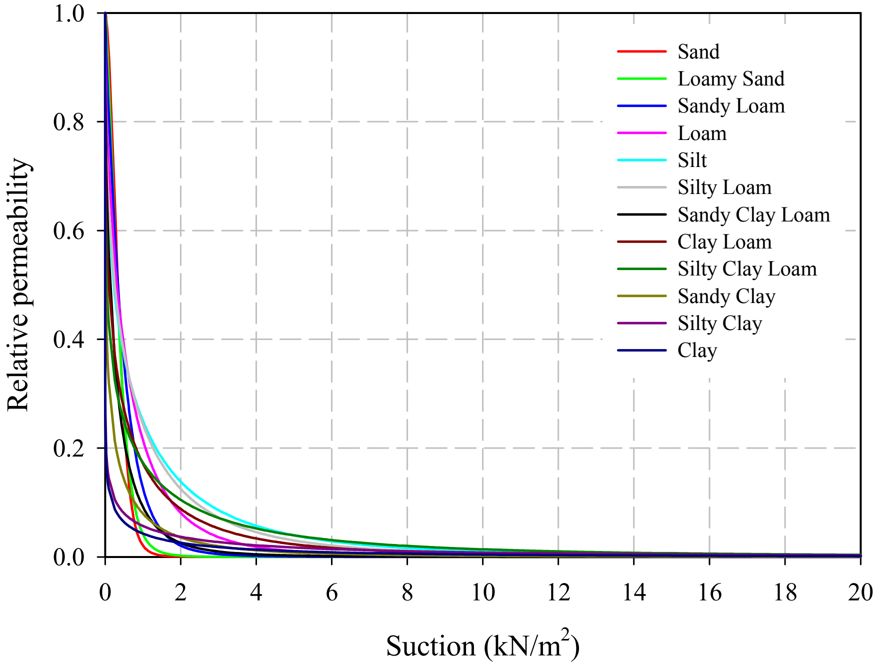

Fig. 51: Relative permeability vs suction for USDA series with Van Genuchten Models

5.3 Stability analysis

5.3.1 Shear strength of unsaturated soils

The principle of effective stress is applicable for saturated soils. For unsaturated soils, the water phase fills only parts of the pore volume, whereas the remainder is covered by air. Bishop (1959) has modified Terzaghi's classical effective stress theory and presented the matric suction coefficient (χ) for the effective stress of unsaturated soils:

$$\sigma' = (\sigma - p_a) + \chi(p_a - p_w) \tag{78}$$

Where σ' and σ are, correspondingly, the effective and total stress, p_a is the pore air pressure, and p_w is suction pore pressure. The term (p_a – p_w) is called matric suction and χ is the matric suction coefficient and varies from 0 to 1 covering the range from dry to fully saturated conditions. For fully saturated soil (χ = 1), the effective stress equation is acquired as:

$$\sigma' = (\sigma - p_w) \tag{79}$$

and for dry soil (χ = 0) the effective stress equation is:

$$\sigma' = (\sigma - p_a) \tag{80}$$

By assuming that the pore air pressure is constant and is small enough to be neglected ($p_a \approx 0$), consequently for a dry soil, effective stress and total stress are the same. The matric suction coefficient (χ) is usually obtained from laboratory tests on both saturated and unsaturated samples. Commonly, the laboratory tests on unsaturated soils are expensive, time consuming and difficult to carry out. Oberg and Sallfors (1997) and Vanapalli et al. (1996) suggested that the factor χ can approximately be replaced by the degree of saturation or the effective degree of saturation, because the shear strength of unsaturated soils is strongly related to the amount of water in voids and in turn to the matric suction. In Figure 52 examples of experimental data are plotted together with approximations suggested in the literature (Vanapalli et. al., 1996).

Consequently, the effective stress equation can be simplified to:

$$\sigma' = \sigma - S_e p_w \tag{81}$$

where S_e is the effective degree of saturation of soil that is a function of the suction pore pressure as defined by the Soil Water Characteristics Curve (SWCC). Fredlund *et al.* (1995) proposed a model to estimate the shear strength of unsaturated soil based on the saturated soil shear strength and the Soil Water Characteristic Curve (SWCC).

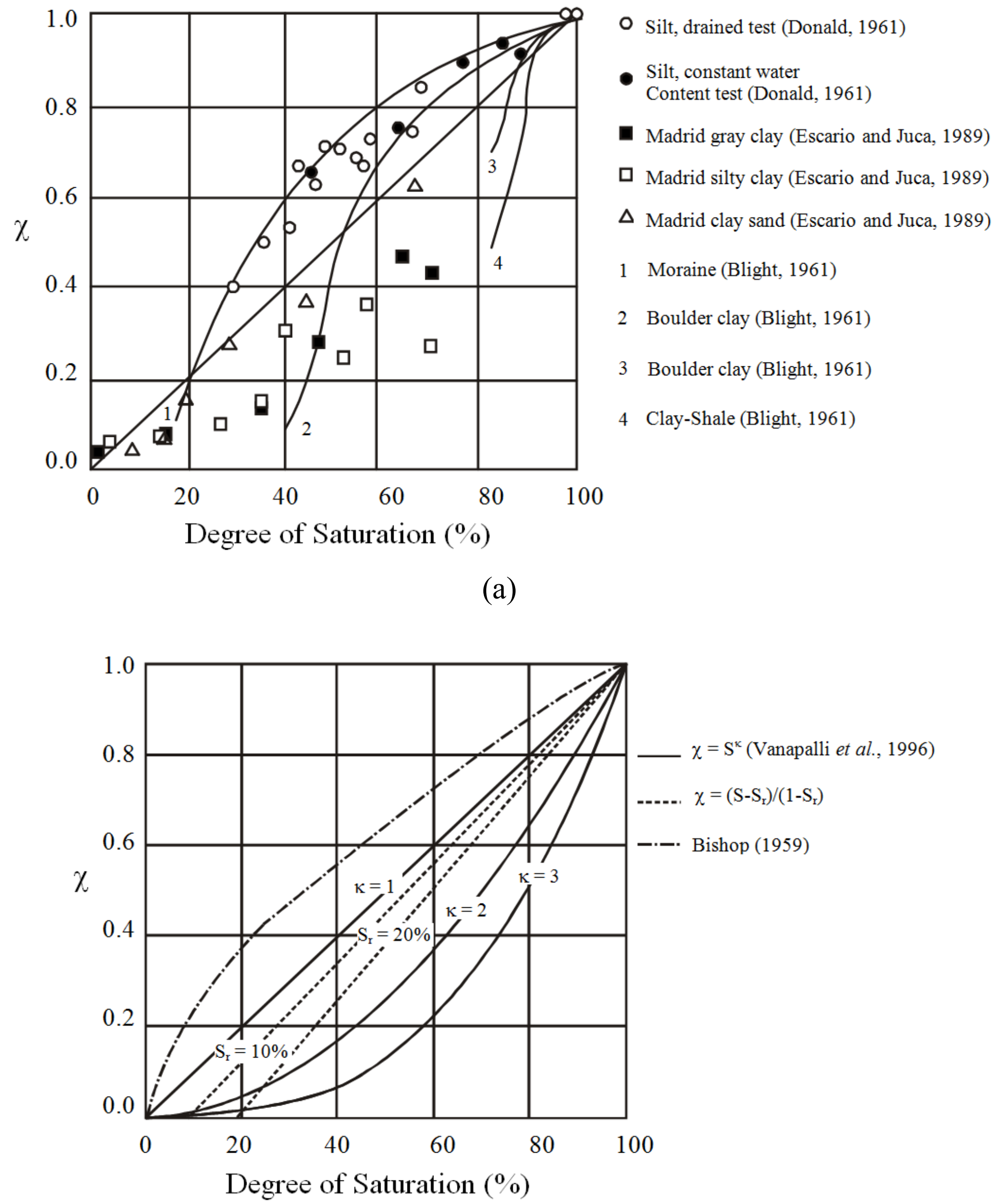

(a)

(b)

Fig. 52: Determination of matric suction coefficient; (a) χ – Sr relationship – experimental data; (b) χ – Sr relationship (Vanapalli et al., 1996)

In unsaturated soils, the weight of the soil (γ) is calculated by following formulation:

$$\gamma = (1 - S_e)\gamma_{unsat} + S_e \gamma_{sat} \tag{82}$$

where γ_{unsat} is the unsaturated soil weight above the phreatic level and γ_{sat} is the saturated soil weight below the phreatic level.

5.3.2 Matric suction profile

The profile of matric suction in a horizontally layered unsaturated soil generally depends on several factors: especially the soil properties as given by the SWCC and the soil permeability, environmental factors including infiltration due to precipitation or evaporation rates, and boundary drainage conditions including the location of groundwater level.

The matric suction profile will come to equilibrium at a hydrostatic condition when there is zero net flux from the ground surface. If moisture is extracted from the ground surface such as evaporation, the matric suction profile will be drawn to the left. If moisture enters at the groundwater surface such as infiltration, the matric suction profile will be drawn to the right (Figure 53).

Under steady state conditions, the water flux in and out of the soil reaches a balance. If the magnitude of water flux is the same as the hydraulic conductivity of the unsaturated soil, the magnitude of the pore-water pressure is constant.

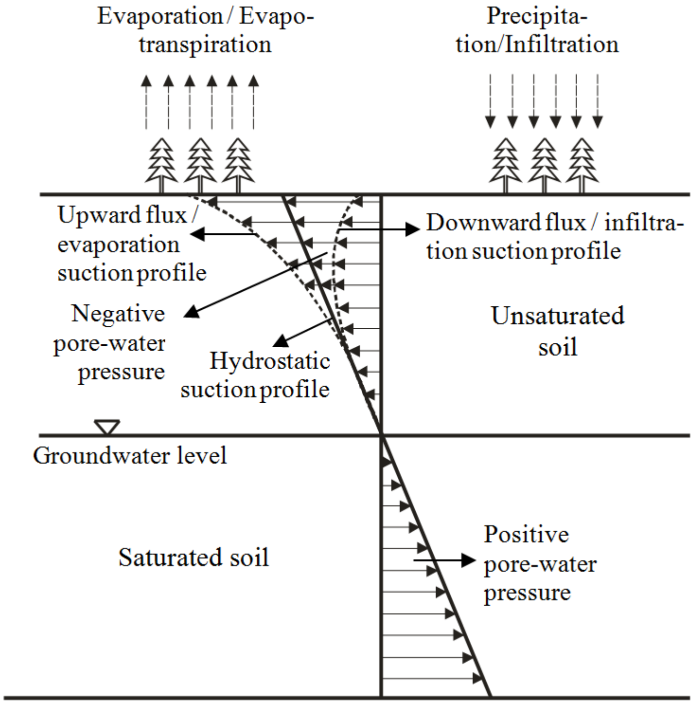

Fig. 53: Matric suction profile in horizontally layered unsaturated soil profiles under various surface flux boundary conditions (After Fredlund, 1996)

The pore water pressure during infiltration under transient seepage conditions can be considered as a transitional state between initial state and the final steady states condition. The time to reach steady state is a function of the rainfall intensity, the hydraulic conductivity of the soil, and the water storage of the soil. When the rainfall intensity (q) is less than the saturated hydraulic conductivity of soil (k_{sat}), the matric suction in the unsaturated soil can decrease but not disappear (Figure 54a). The matric suction can be eliminated only when the rainfall intensity is equal to or greater than the saturated hydraulic conductivity of soil (Figure 54b). Some methods to analyze infiltration into unsaturated soil slopes have been illustrated by Cho and Lee (2002) and Gavin and Xue (2008) with their assumptions.

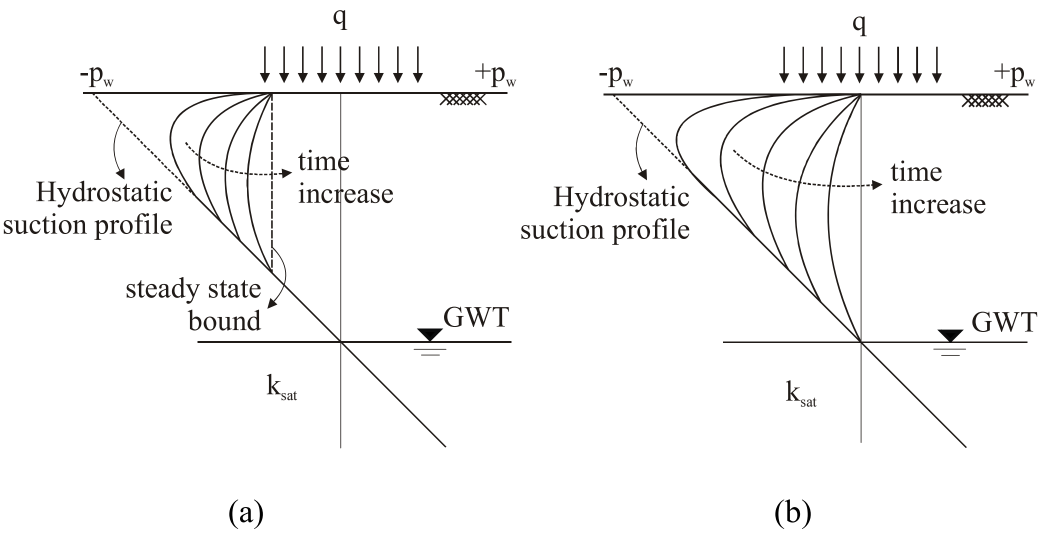

Fig. 54: Matric suction profile during infiltration under transient seepage conditions (a) $q < k_{sat}$, and (b) $q \geq k_{sat}$

Figures 55 to 58 illustrate the profile of matric suction and degree of saturation of loamy sand, silt, sandy clay, and clay column, respectively during rainfall infiltration with intensity q = 0.01 m/hour. The height of the column is 3 m with the ground water level at 1m. The hydraulic data of the USDA series with Van Genuchten model in Table 13 are used for these soils. In this case, the rainfall intensity is less than the saturated hydraulic conductivity of loamy sand, silt, and sandy clay soils, but greater than the saturated hydraulic conductivity of clay soil.

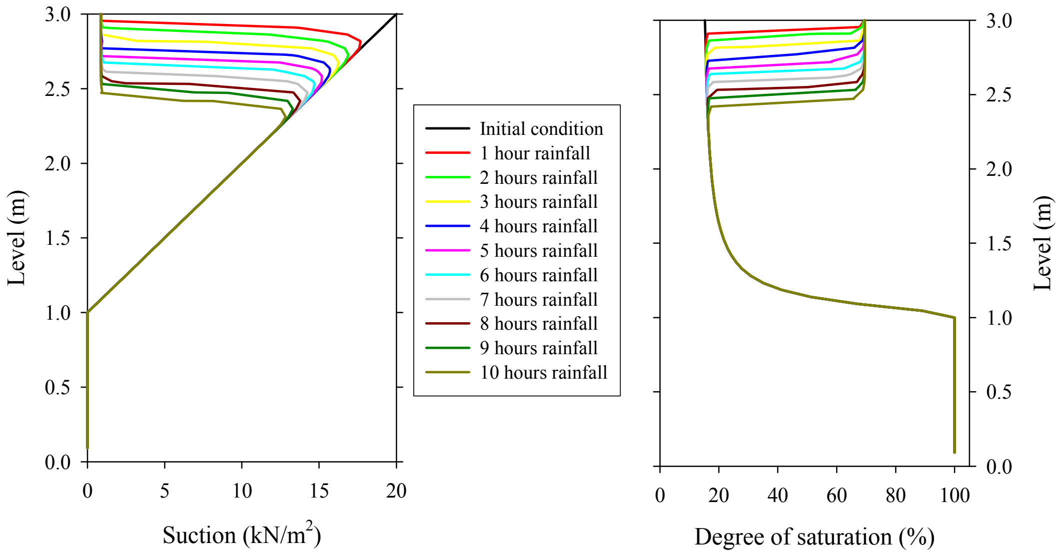

Fig. 55: Matric suction and degree of saturation profile of loamy sand column during infiltration

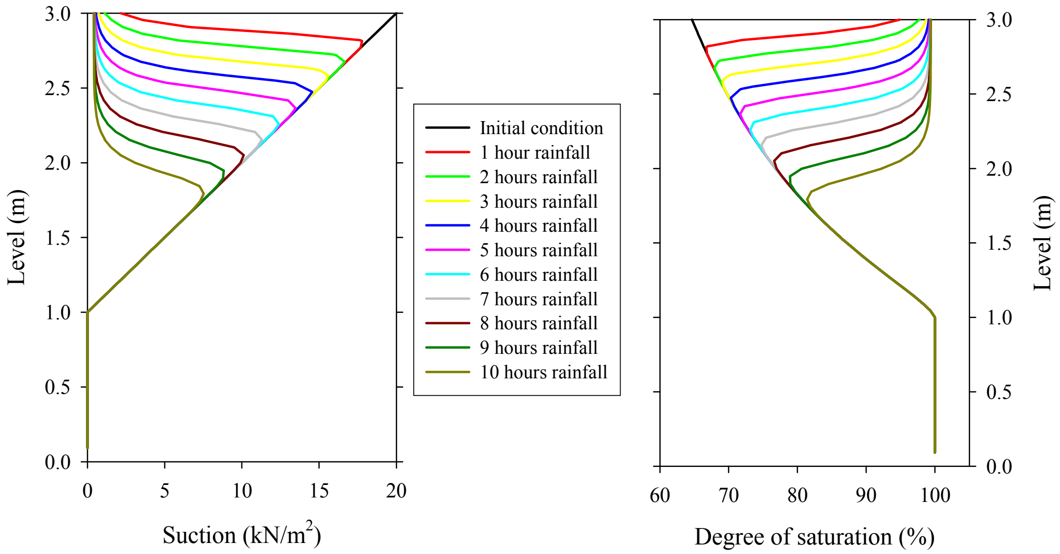

Fig. 56: Matric suction and degree of saturation profile of silt column during infiltration

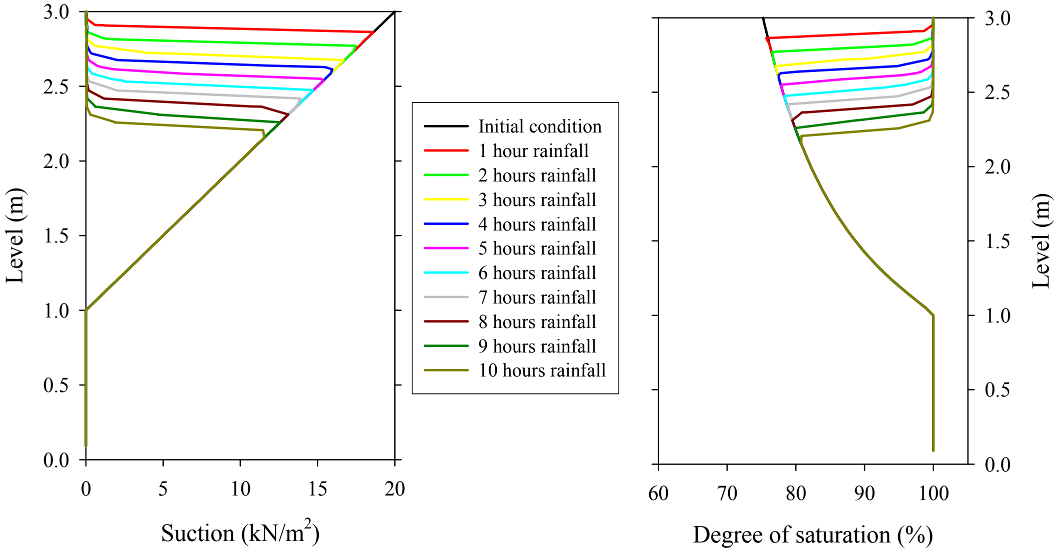

Fig. 57: Matric suction and degree of saturation profile of sandy clay column during infiltration

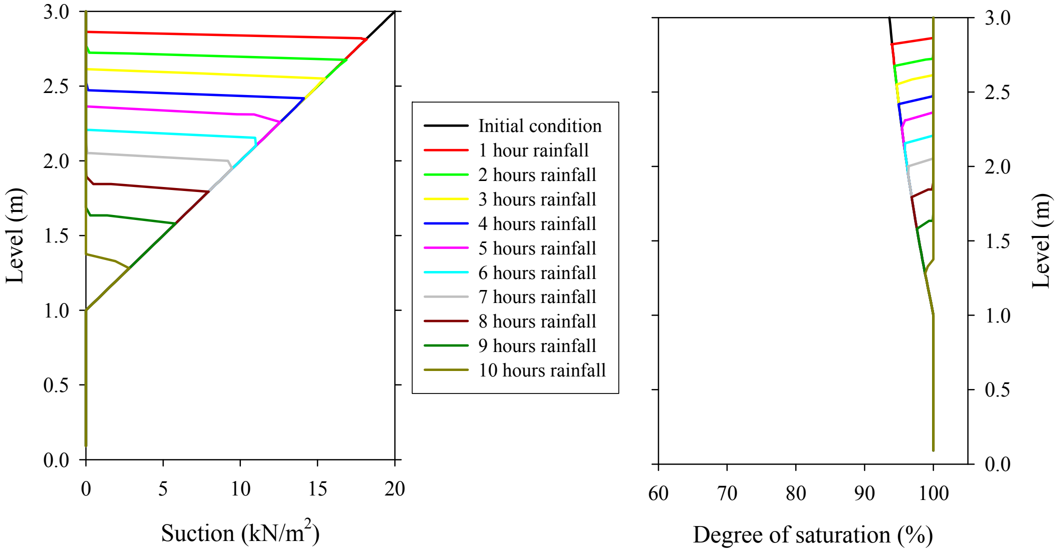

Fig. 58: Matric suction and degree of saturation profile of clay column during infiltration

5.4 Influence of horizontal water table in slope stability

In this section, slope stability analysis of unsaturated soils considering suction will be discussed. The influence of various depths of the horizontal water table on slope stability will be evaluated. A simple case of a homogeneous slope has been chosen. The international soil classification system USDA series is used for determining the hydraulic data for the analysis (see Table 13). The mechanical and hydraulic models used in the analysis are the Mohr Coulomb failure criterion and the Van Genuchten model respectively.

5.4.1 Geometry, finite element mesh and material properties

The height of the slope is 10 m and the gradient (horizontal to vertical) is 2:1. Figure 59 shows the geometry and the two dimensional finite element meshes consisting of 4800 15-noded elements.

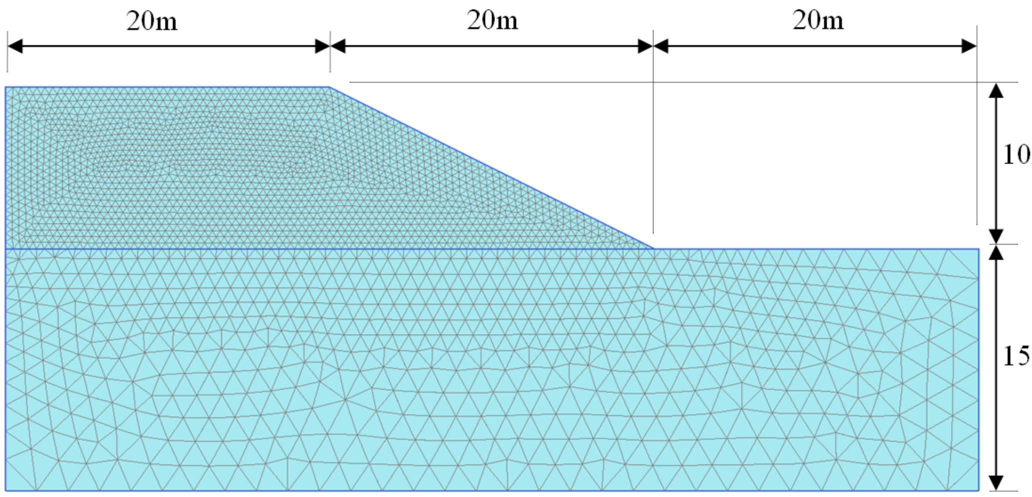

Fig. 59: Geometry and finite element mesh of the slope

Four different hydraulic parameter sets of the USDA series for the Van Genuchten Models are used to evaluate the effect of these parameters in slope stability with various depths of the horizontal water table, namely clay, sandy clay, silt and loamy sand as given in Table 13. For simplicity it is assumed that all the soils have the same shear strength and stiffness parameters. Soil parameters for the Mohr Coulomb model used in the analysis are given in Table 14.

Tab. 14: Soil Parameters for Mohr Coulomb Model

Description	Symbol	Unit	Value
Unit weight	γ	[kN/m^3]	20
Elasticity modulus	E’	[kPa]	7500
Effective poisson's ratio	ν'	[-]	0.35
Effective cohesion	c'	[kPa]	20
Effective friction angle	ϕ'	[^{o}]	20

5.4.2 Boundary conditions

The ground water table was assumed to be horizontal at a certain depth (d). The lower boundary of the model was assumed as impervious boundary (Figure 60). To evaluate the influence of various depths of horizontal water table on the slope, the analyses were performed with d/H ratios between 0.0 and 2.4.

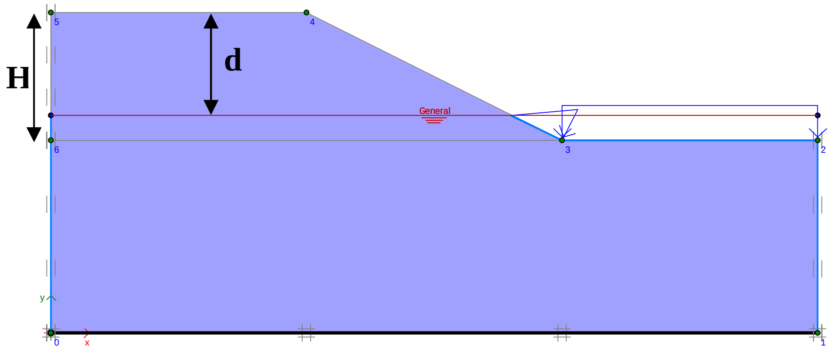

Fig. 60: Boundary conditions of the model

5.4.3 Results

Table 15 and Figure 61 show the changes in the factor of safety (FOS) with various depths of horizontal water table with and without considering suction. When fully submerged (d/H = 0), the FOS is 2.372 for all different hydraulic parameters because there is no suction. The critical level that gives the minimum factor of safety occurs at d/H ≈ 0.8 (d ≈ 8m). After passing the minimum, the increase of water table depth will increase the FOS of the unsaturated slopes. The

FOS of the unsaturated slopes with hydraulic parameters for clays (low permeability) are significantly increased. Conversely, the FOS of the unsaturated slopes with hydraulic parameters for loamy sands (high permeability) show no significant increase and when the ratio of d/H is more than 1.2, the depth of horizontal ground water table will not influence the stability.

Without considering suction, the fully submerged slope has of course the same FOS of 2.371 and the critical level that gives the minimum factor of safety occurs at d/H ≈ 0.8 (d ≈ 8m). When the ratio of d/H is more than 1.2, the depth of horizontal ground water table will not influence the stability, hence the FOS of the slope remains constant. The failure mechanisms of the slopes without considering suction are shown in Figure 62.

Figures 63 to 66 illustrate the failure mechanisms, suction and degree saturation of the slopes with various depths of horizontal water table.

Tab. 15: The factor of safety of slopes with various depths of horizontal water table

d/H	FOS				
	With suction				Without suction
	Clay	Sandy Clay	Silt	Loamy Sand	
	k_{sat} = 5.5E-07 m/s	k_{sat} = 3.3E-06 m/s	k_{sat} = 6.9E-06 m/s	k_{sat} = 4.1E-05 m/s	
0.0	2.372	2.372	2.372	2.372	2.371
0.2	2.032	2.028	2.027	2.004	2.024
0.4	1.809	1.799	1.792	1.760	1.780
0.6	1.699	1.677	1.671	1.619	1.640
0.8	1.673	1.638	1.629	1.557	1.573
1.0	1.709	1.666	1.654	1.575	1.573
1.2	1.906	1.846	1.826	1.713	1.664
1.4	2.129	2.038	2.008	1.747	1.668
1.6	2.362	2.240	2.166	1.747	1.668
1.8	2.603	2.360	2.237	1.758	1.668
2.0	2.853	2.454	2.297	1.757	1.668
2.2	3.073	2.545	2.354	1.758	1.668
2.4	3.254	2.633	2.408	1.754	1.668

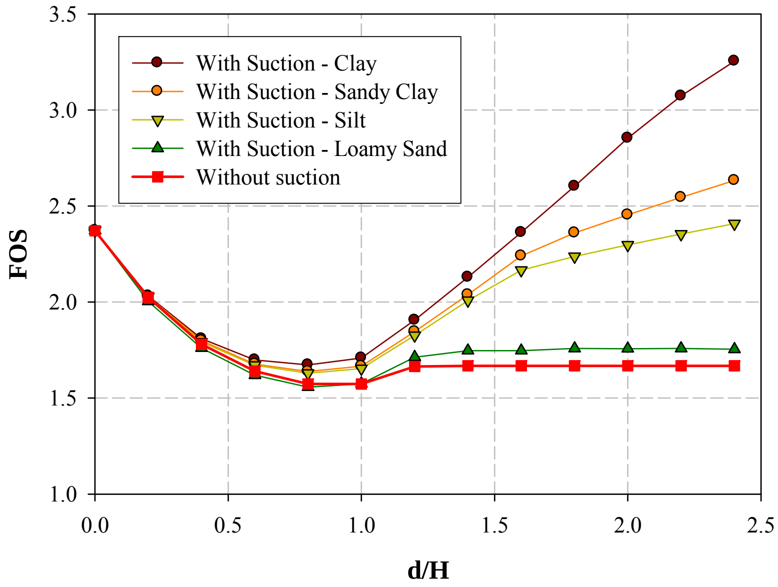

Fig. 61: Change of FOS with different d/H ratios.

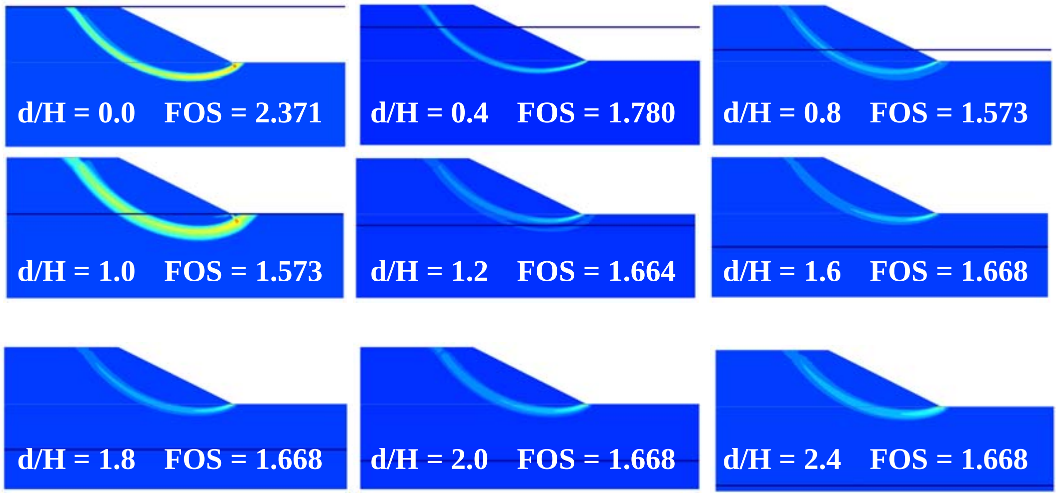

Fig. 62: Failure mechanism with various depths of horizontal water table in slopes without considering suction.

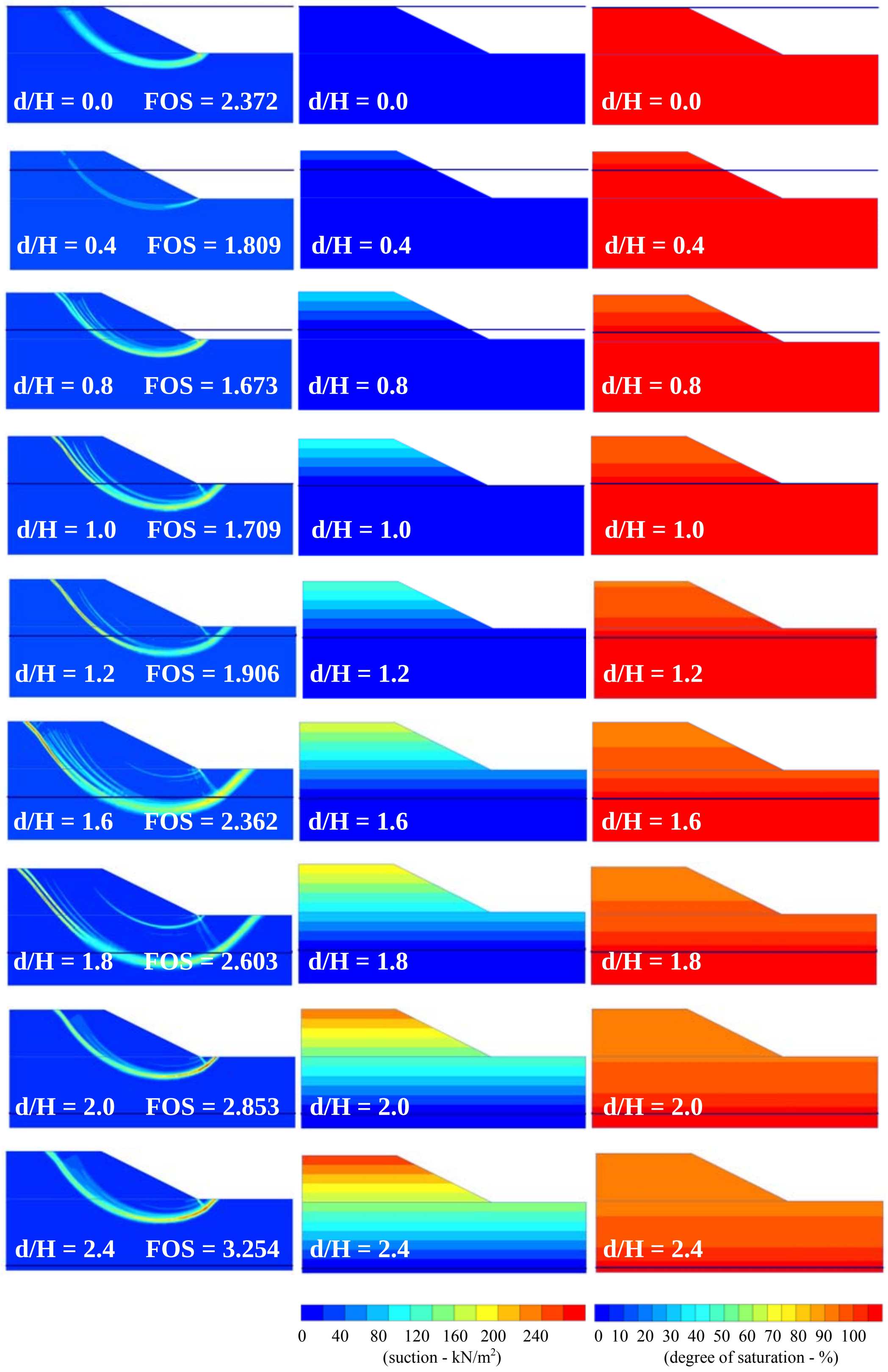

Fig. 63: Failure mechanism, suction and saturation with various depths of horizontal water table in clay slopes.

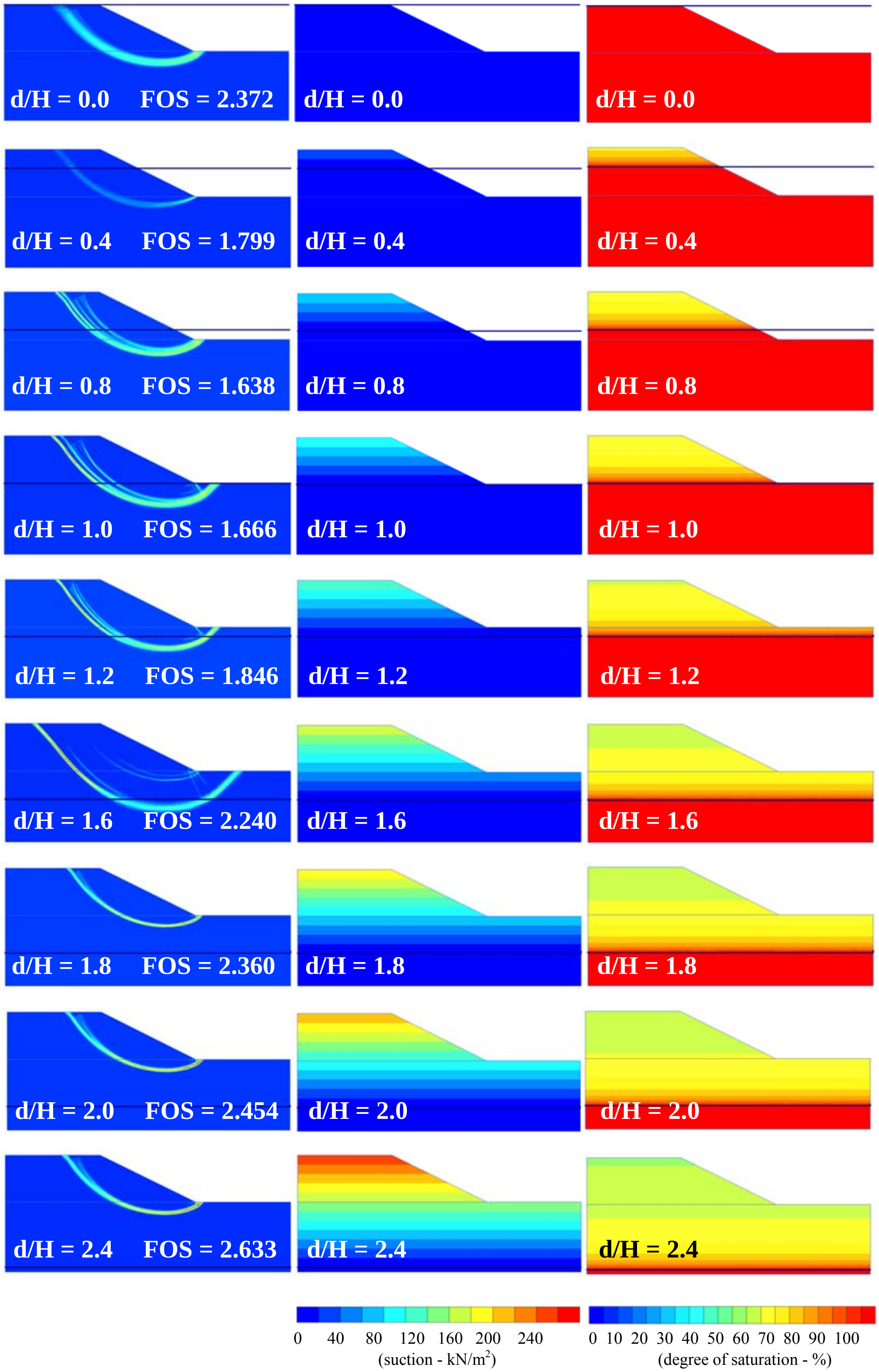

Fig. 64: Failure mechanism, suction and saturation with various depths of horizontal water table in sandy clay slopes.

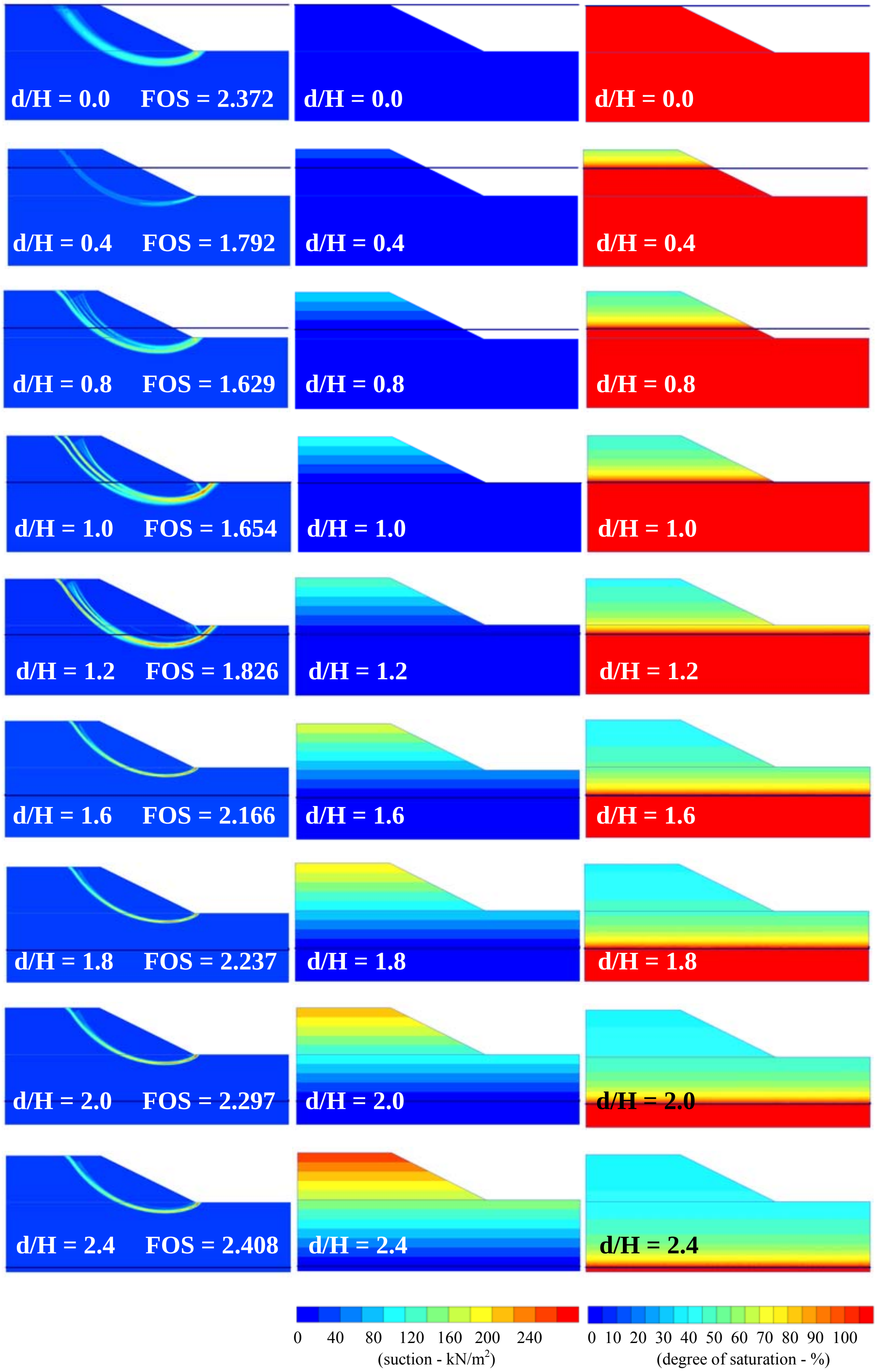

Fig. 65: Failure mechanism, suction and saturation with various depths of horizontal water table in silt slopes.

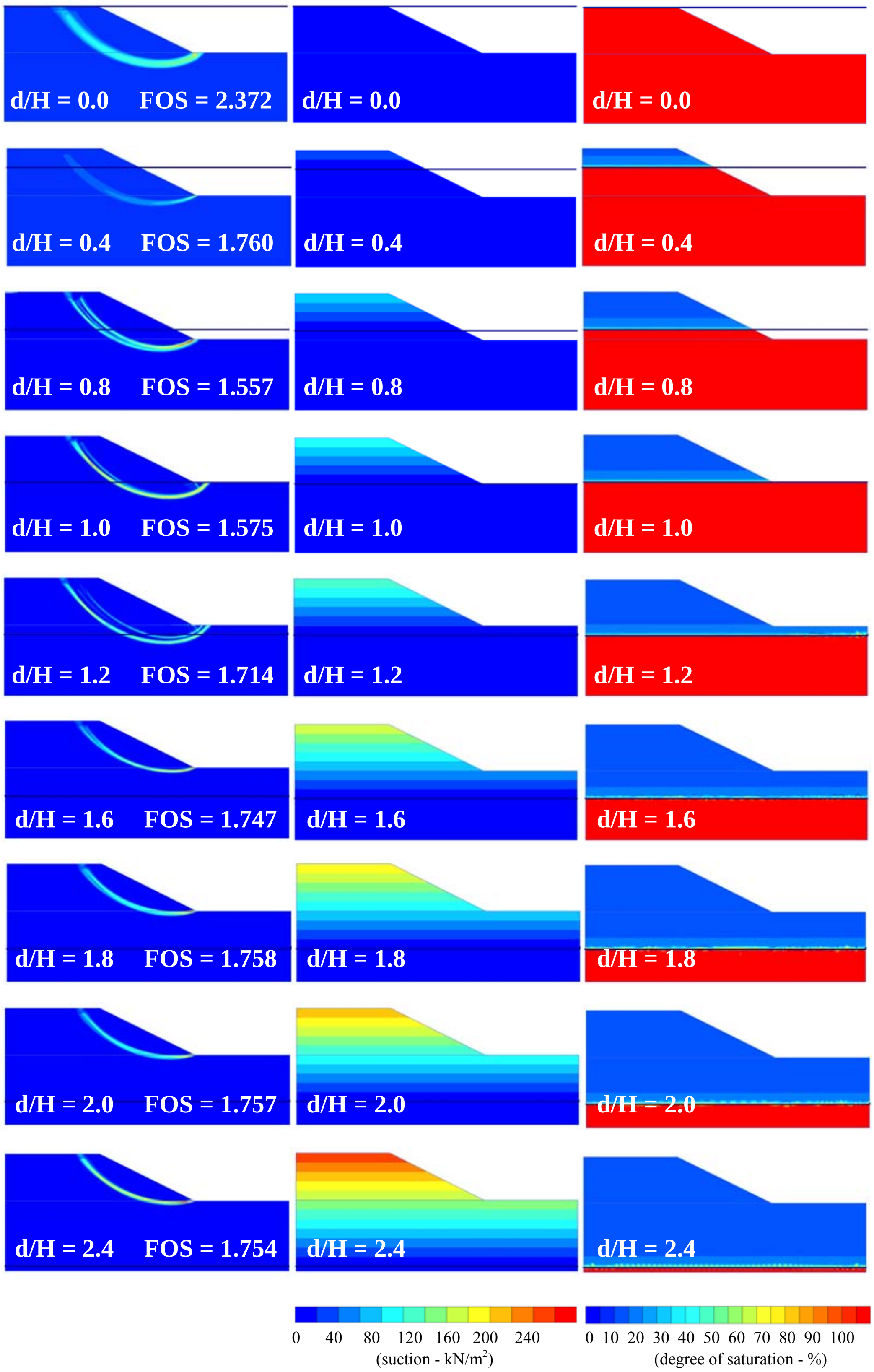

Fig. 66: Failure mechanism, suction and saturation with various depths of horizontal water table in loamy sand slopes.

5.5 Slope stability analysis with rain infiltration

In this section, slope stability analysis of unsaturated soils with rain infiltration will be discussed. The mechanical and hydraulic models used in the analysis are the Mohr Coulomb failure criterion and the Van Genuchten model respectively.

5.5.1 Geometry, finite element mesh and material properties

The geometry, finite element mesh and material properties from the previous example are used. Four different hydraulic parameter sets of the USDA series for the Van Genuchten Models are used to evaluate the effect of these parameters in slope stability during rain infiltration, namely clay, sandy clay, silt, and loamy sand as given in Table 13. For simplicity it is assumed that all the soils have the same shear strength and stiffness parameters.

5.5.2 Boundary conditions

The initial ground water level was assumed to be horizontal at the level of the toe of the slope. A rainfall with intensity of 10 mm/hour lasting 3 days (72 hours) was applied on the crest and the slope. The minimum and the maximum pore pressure head respectively are -0.1 m (Ψ_{min}) and 0.1m (Ψ_{max}). In positive precipitation, when the water level comes above the ground surface at a depth of 0.1m then the water is supposed to run-off. In negative precipitation, when the water level comes below the ground surface at a depth of 1.0m then the evaporation is supposed to stop. The left boundary, right boundary and lower boundary of the model were assumed impervious boundaries (Figure 67).

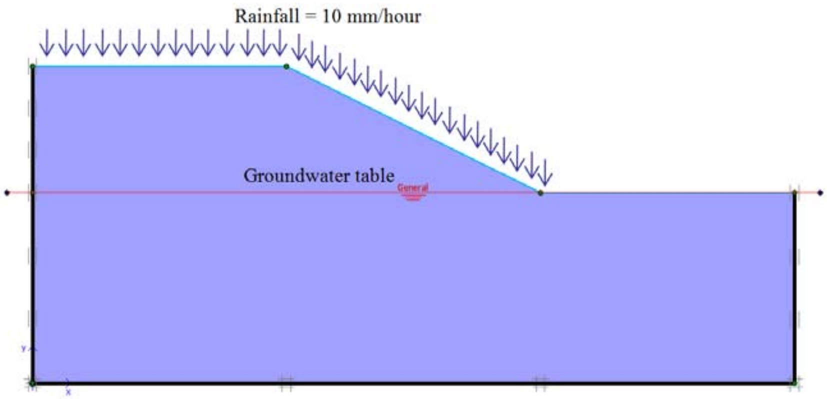

Fig. 67: Boundary conditions of the model

Figure 68 shows the initial suction in the model, which is assumed to increase linearly above ground water level until ground surface. The initial suction will come to equilibrium at a hydrostatic condition when there is zero net flux from the ground surface. Figure 69 presents the initial degree of saturation for the four different hydraulic parameters leading to different initial degree of saturation at the same suction. The minimum degree of saturation for clay, sandy clay, silt and loamy sand is 85.43%, 60.73%, 40.39% and 14.08% respectively. The value of minimum degree of saturation depends on the hydraulic parameters and the soil thickness above the ground water level.

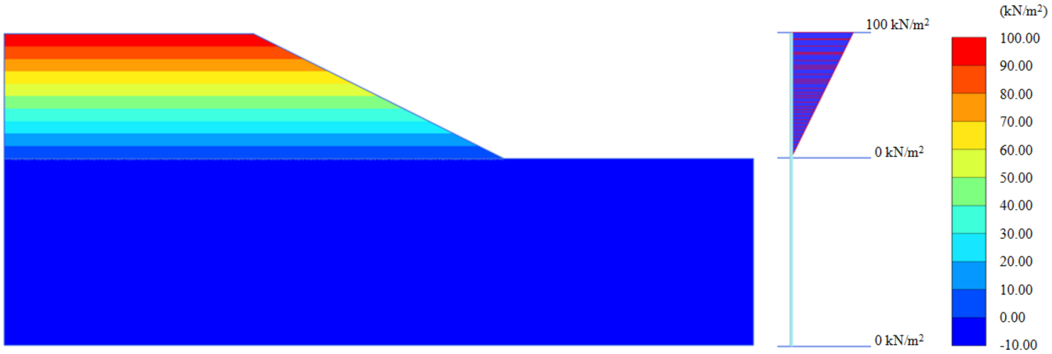

Fig. 68: Initial conditions: suction

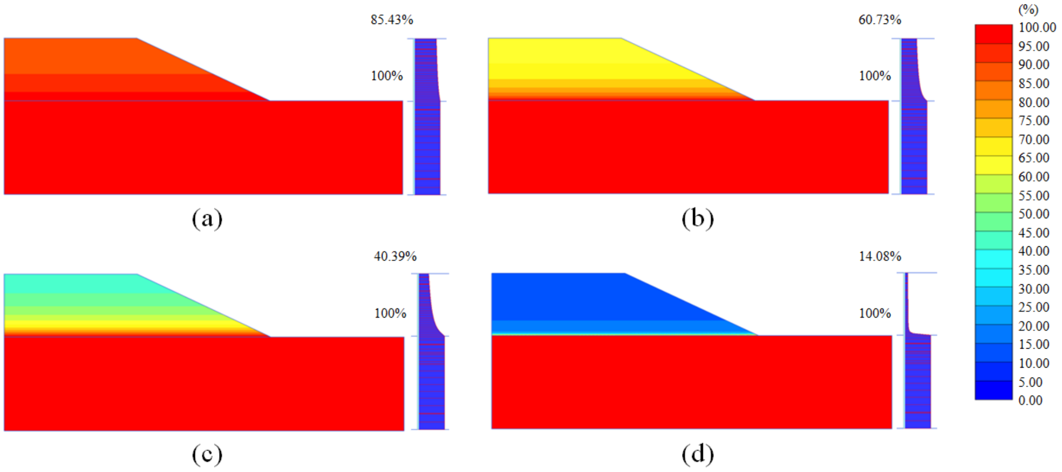

Fig. 69: Initial conditions: degree of saturation (a) Clay, (b) Sandy Clay, (c) Silt, and (d) Loamy Sand

5.5.3 Results

Table 16 and Figure 70 show the changes in the factor of safety (FOS) with time of infiltration. During rain infiltration suction decreases and therefore the FOS of the slope is reduced. As expected the suction in the soil with high permeability reduces faster than for the low permeability soil. From initial conditions until 3 days of rain infiltration, the FOS of the clay slope reduced by only 1%, for the Sandy Clay soil by 3%. However, for Silt and Loamy Sand soils with high permeability the FOS decreases by 13% and 22% respectively. Figures 71 to 74 illustrate the failure mechanisms and change of suction and saturation during the assumed rainfall period for the different soils. The scaling in these figures (change of suction and degree of saturation) correspond to Figures 78 and 79.

Tab. 16: Calculated factor of safety of the unsaturated soil slope subjected to rain infiltration

Time (hours)	FOS			
	Clay	Sandy Clay	Silt	Loamy Sand
	k_{sat} = 5.5E-07 m/s	k_{sat} = 3.3E-06 m/s	k_{sat} = 6.9E-06 m/s	k_{sat} = 4.1E-05 m/s
0	1.709	1.666	1.654	1.575
3	1.708	1.666	1.649	1.572
6	1.708	1.663	1.642	1.570
9	1.707	1.662	1.636	1.568
12	1.706	1.660	1.631	1.565
18	1.704	1.656	1.618	1.561
24	1.702	1.653	1.606	1.556
36	1.702	1.643	1.573	1.532
48	1.698	1.631	1.537	1.479
60	1.694	1.623	1.498	1.352
72	1.690	1.611	1.436	1.229

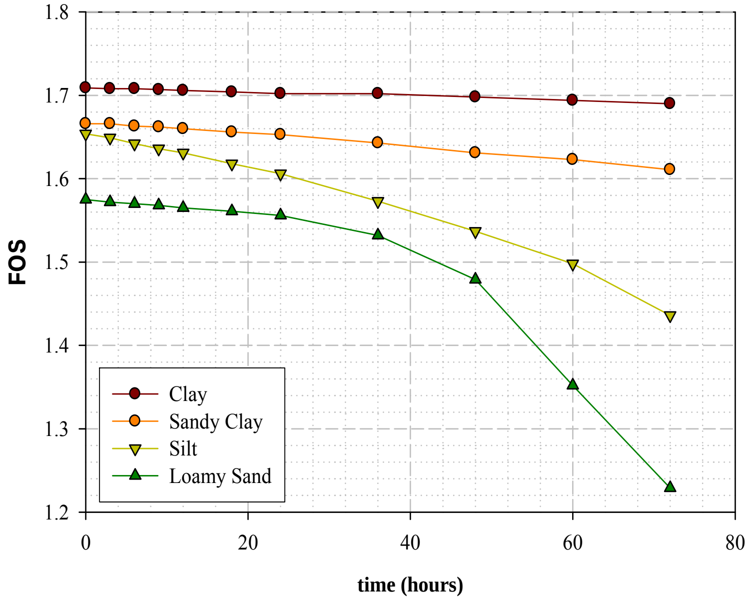

Fig. 70: Change of FOS with time for unsaturated soil slope subjected to rain infiltration

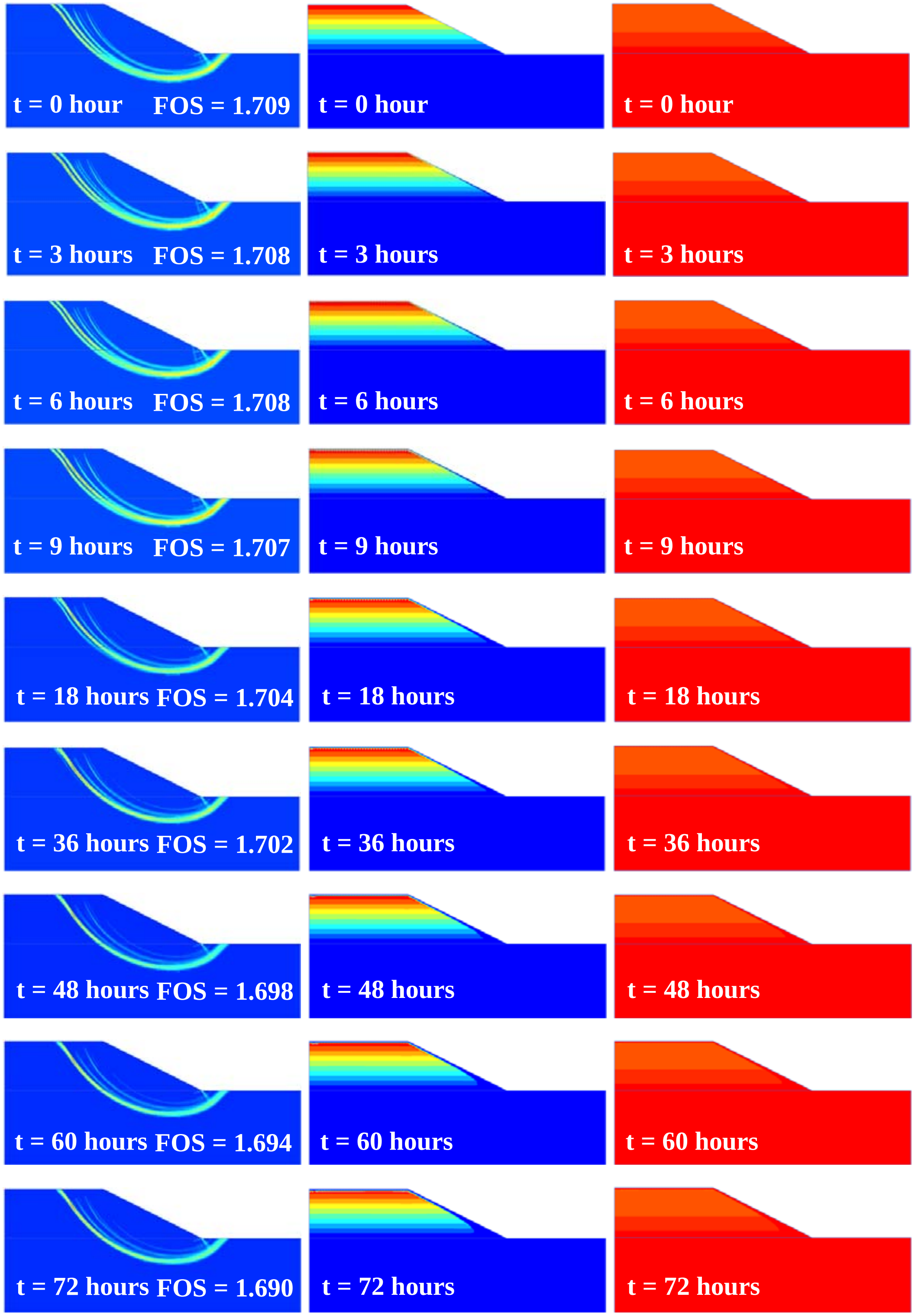

Fig. 71: Failure mechanism, change of suction and saturation during infiltration for clay slopes

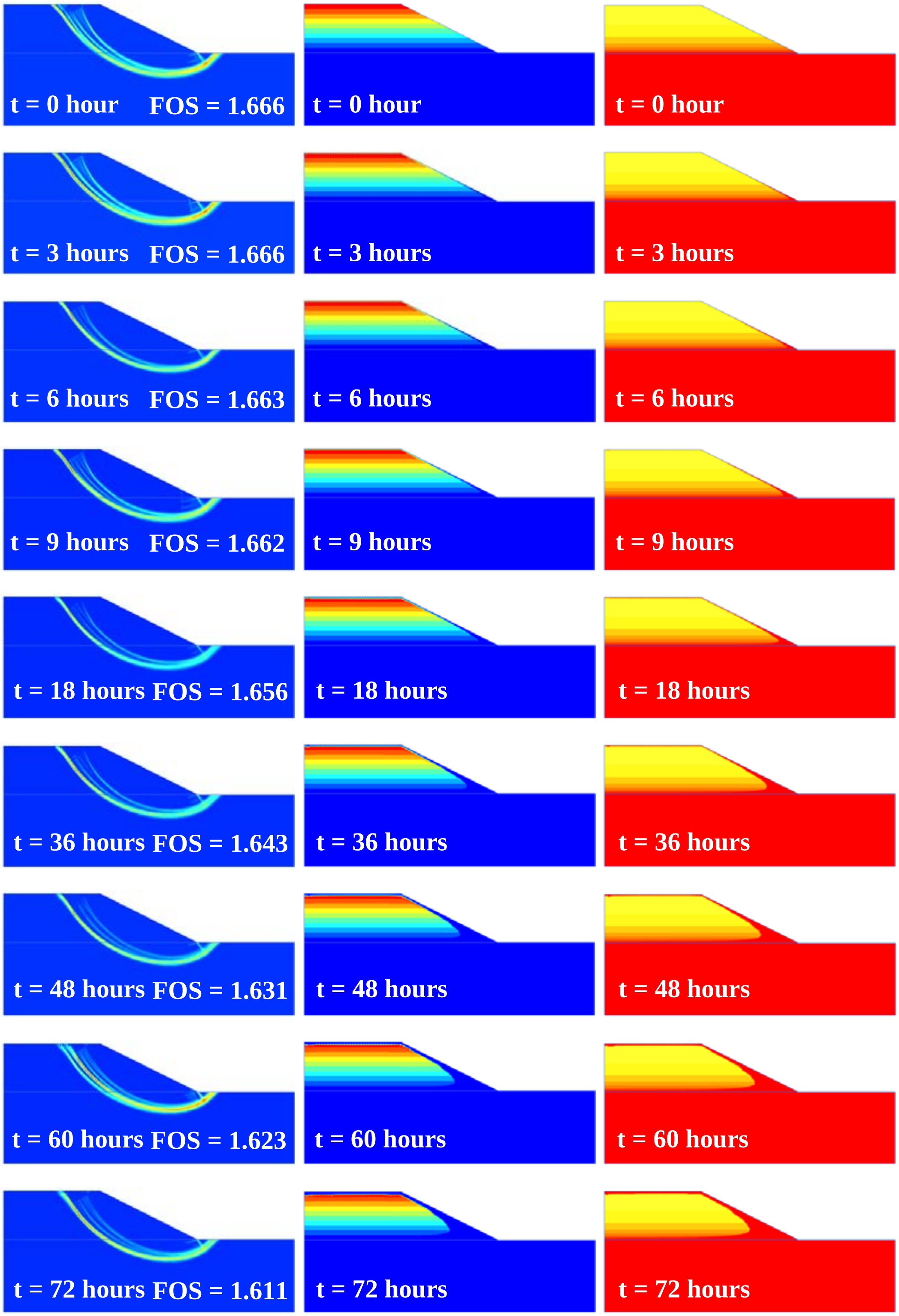

Fig. 72: Failure mechanism, change of suction and saturation during infiltration for sandy clay slopes

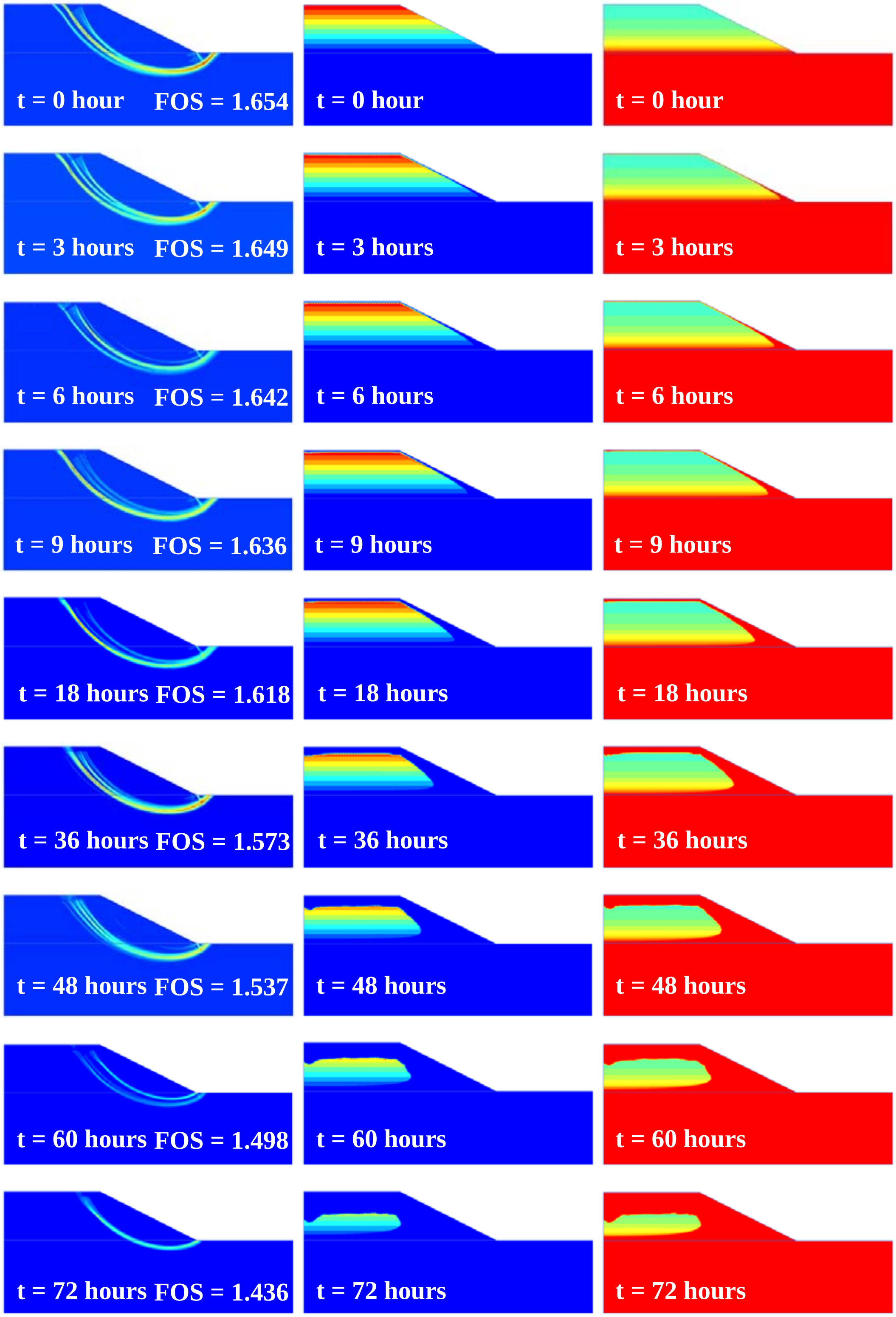

Fig. 73: Failure mechanism, change of suction and saturation during infiltration for silt slopes

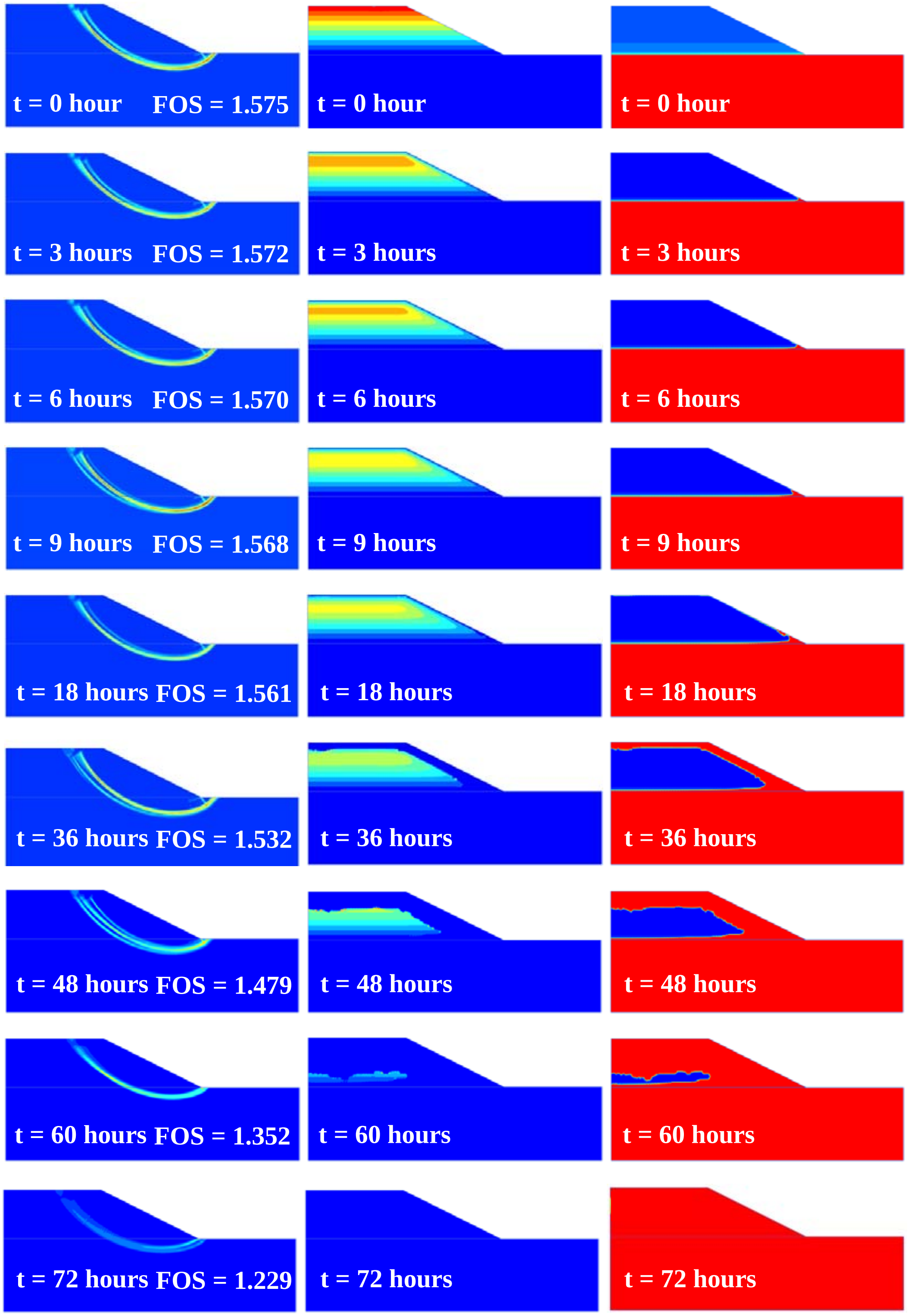

Fig. 74: Failure mechanism, change of suction and saturation during infiltration for loamy sand slopes

5.6 Summary

The finite element method has been used to evaluate the stability of unsaturated soil slopes employing a fully coupled deformation and groundwater flow analysis. The stability of an unsaturated slope will be affected by the distribution of negative pore water pressures (suction). The slope stability increases when the shear strength contributed by matric suction is taken into account. Different hydraulic parameters will generate different distributions of saturation in different soils based on the Soil Water Characteristic Curves (SWCC) for the particular soil. These parameters will effects the FOS of the slope with and without rainfall infiltration. The water table location also will influence the factor of safety of the slopes. During the time of rain infiltration, suction decreases and thus the FOS of the slope reduces, whereas the reduction is faster for soils with high permeability than for soils with low permeability.

6 Back analysis of an unsaturated soil slope subjected to rainfall infiltration

This section presents results from the back analysis of a well instrumented and monitored 11-m high cut slope in Zaoyang, Hubei, China in order to get a better understanding of the complex soil water interaction in an unsaturated soil slope subjected to rainfall infiltration

A full-scale field study was completed on an unsaturated soil slope in the Hubei province of China (Ng *et al.*, 2003, 2008, and Zhan *et al*., 2007). The artificial rainfall and in situ monitoring were conducted in this field trial. Hydraulic characteristics such as saturated coefficient of permeability and initial degree of saturation, intensity and duration of rainfall are important parameters in this kind of analysis. Unfortunately not all of these parameters have been available and therefore some assumptions had to be made based on engineering judgement. In this study, measured data are compared to results from finite element calculations based on a fully coupled flow-deformation analysis with time dependent boundary conditions.

6.1 Instrumentation and monitoring

6.1.1 The monitoring area

The monitoring area is in a semi-dry area, located in Zaoyang, Hubei, China. The average of annual rainfall is about 800 mm and 70% of rainfall is distributed from May to September. The surface of the slope was well grassed, but no trees were there (Figure 75). The area had a significant depth of typical unsaturated expansive soil.

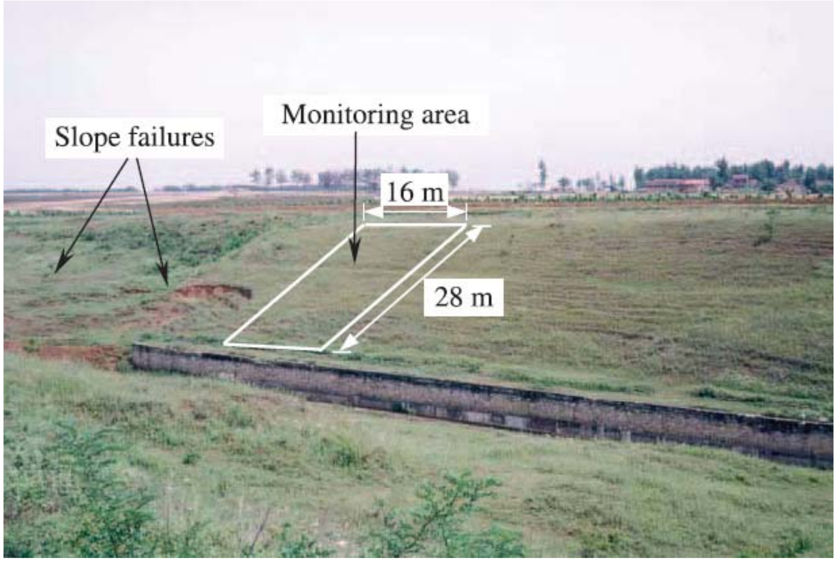

Fig. 75: Overall view of monitoring area (Zhan *et. al.*, 2007)

6.1.2 Soil profile and properties

Bore holes investigation was carried out around the monitoring area. Soil sampling, standard penetration test (SPT) and dilatometer tests (DMT) were carried out in the boreholes. Figure 76 illustrated the soil profiles and geotechnical parameters obtained from the boreholes around mid-slope (Ng *et al.*, 2003). Typical properties for the clay are summarized in Table 19.

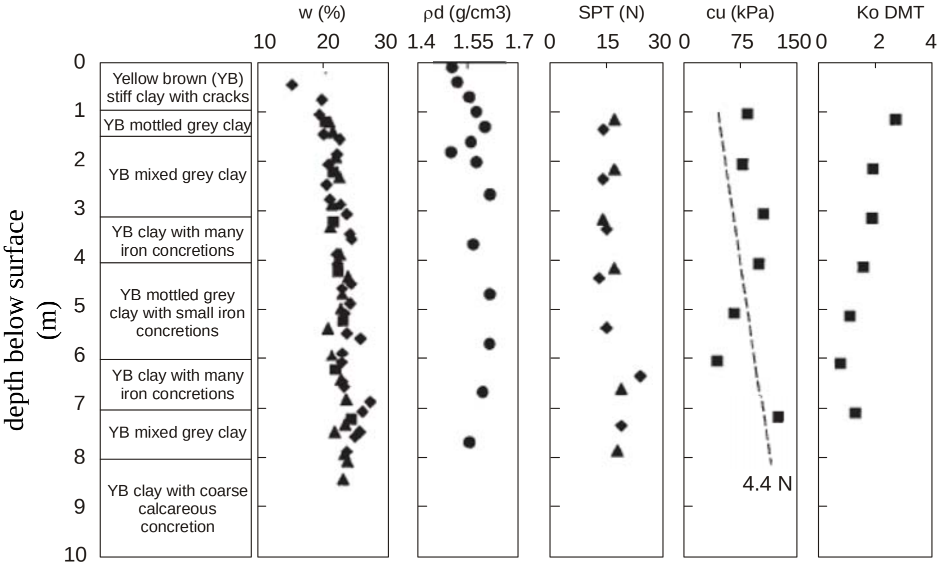

Fig. 76: Soil profile and geotechnical parameters from the borehole around mid-slope

Tab. 17: Typical Properties of the Clay (Zhan *et. al.*, 2007)

Soil Properties	Symbol	Unit	Value
Classification			
Percentage of sand, silt, clay		[%]	2, 58, 39
USCS classification		[-]	Silty Clay
Specific gravity	Gs	[-]	2.67
Dry density	γ	[kN/m^3]	15 – 16.2
Flow characteristic			
Saturated permeability	k_{sat}	[m/s]	10^{-10} to 10^{-7}
Air entry value		[kPa]	30
Natural shear strength parameters			
Effective cohesion	c'	[kPa]	16.67
Effective friction angle	ϕ'	[^{o}]	28.7

6.1.3 Field instrumentation and artificial rainfall simulation

Field instrumentation and artificial rainfall simulation tests were carried out in a monitoring area 15 m wide and 31 m long. The instrumentation included jet-fill tensiometers, thermal conductivity suction sensors, thetaprobes for determining water content, vibrating-wire earth pressure cells, inclinometer, a tipping-bucket rain gauge, a vee-notch flowmeter, and an evaporimeter (Ng *et al*., 2003, 2008 and Zhan *et al*, 2006). The layout and locations of the instruments are shown in Figure 77.

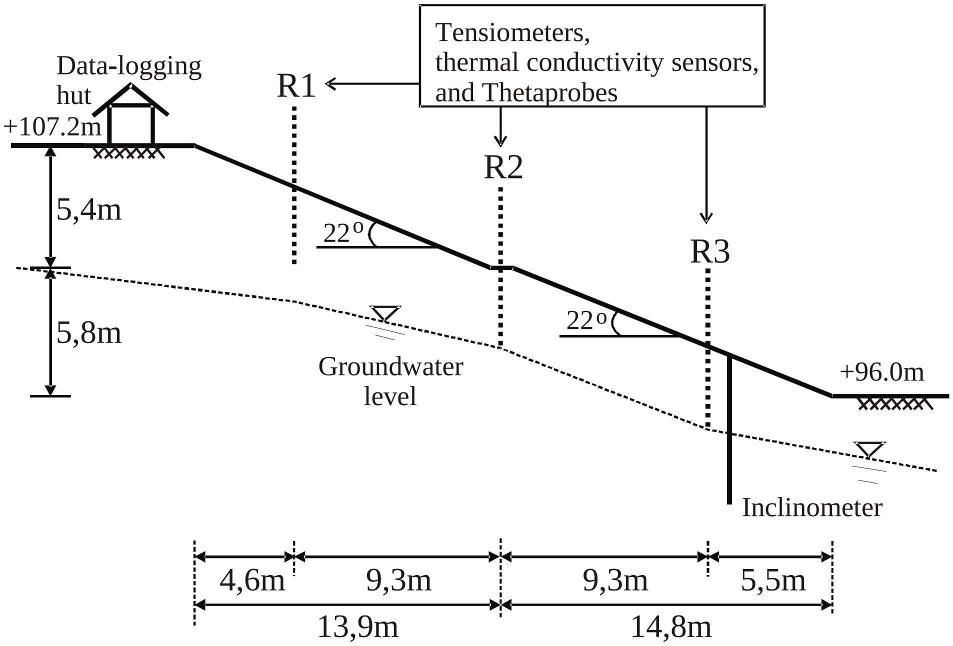

Fig. 77: Cross section of instrumented slope (Ng *et al.*, 2003, 2008 and Zhan *et al.*, 2006)

In this study, the field monitoring to be discussed are pore-water pressures (soil suction), piezometric (groundwater) level and horizontal displacements. There were three rows of instrumentation for pore water pressure and piezometer level monitoring: R1 at the upper part, R2 at the middle part, and R3 at the lower part of the slope. It followed from previous studies that recorded responses in pore-water pressure using jet-fill tensiometers and thermal conductivity suction sensors gave reasonably consistent results. Furthermore, the recorded responses in pore-water pressure from jet-fill tensiometer measurement will be used in this study. Rainfall was artificially produced using a special design sprinkler system that comprised a pump, a main water-supply pipe, five branches, and 35 sprinkler heads. This sprinkler system could produce three levels of rainfall intensity (3, 6 and 9 mm/h).

6.2 Numerical model

In this section, the results from the back analysis of an unsaturated soil slope in Zaoyang, Hubei, China subjected to rain infiltration will be discussed. The mechanical and hydraulic models used in the analysis are the Mohr Coulomb failure criterion and the Van Genuchten model respectively.

6.2.1 Geometry, finite element mesh and material properties

The height of the slope is 11.2 m with a uniform slope angle of 22° and 1 m wide berm at the mid-height of the slope. The geometry and finite element mesh used are shown in Figure 78 and 1894 15-noded elements have been used.

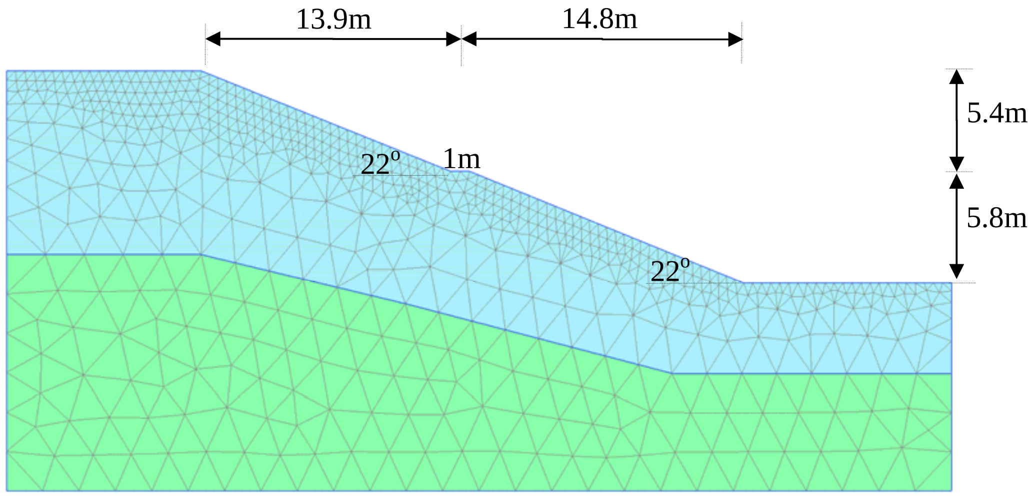

Fig. 78: Geometry and finite element mesh of the slope

The international soil classification system USDA series is used for determining the hydraulic data for the analysis as they were not directly provided by Zhan et al. (2007). Figure 79 depicts the relation between suction and gravimetric water content, known as Soil Water Characteristic Curve (SWCC). This figure also shows comparison between SWCC measured on average dry density for the soils in the monitoring area and SWCC with hydraulic data of clay soils (USDA series with Van Genuchten models).

Soil parameters for the Mohr Coulomb model and hydraulic data of clay used in the analysis are given in Table 18.

Tab. 18: Soil Parameters of upper clay layer for Mohr Coulomb Model

Soil Properties	Symbol	Unit	Value
Unit weight	γ	[kN/m^3]	15.6
Elasticity modulus	E’	[kPa]	6000
Effective poisson’s ratio	ν’	[-]	0.35
Effective cohesion	c’	[kPa]	16.67
Effective friction angle	ϕ’	[^{o}]	28.7
Saturated Permeability	k_{sat}	[m/s]	5.5E-7
Van Genuchten Parameters (USDA series)	g_a	[1/m]	0.80
	g_n	[-]	1.09
	g_l	[-]	0.50

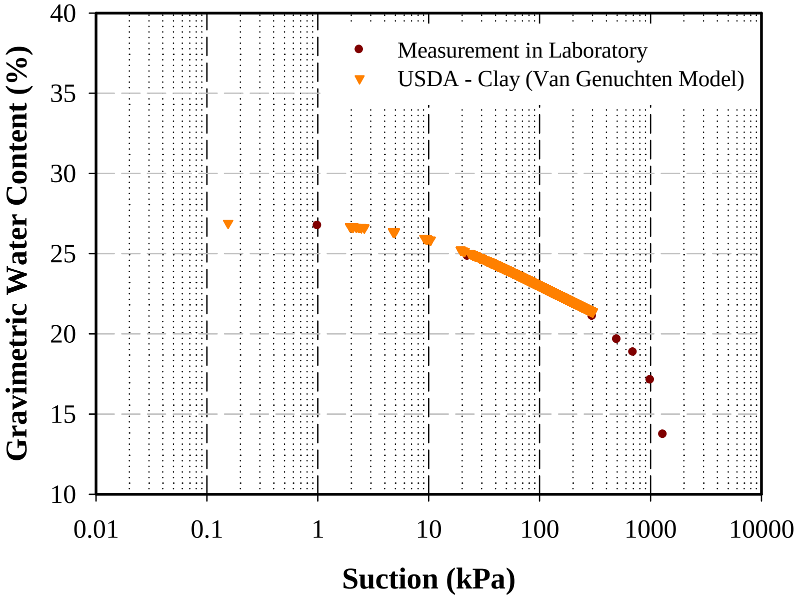

Fig. 79: Soil Water Characteristic Curves (SWCC) for Zaoyang soil

6.2.2 Boundary conditions

The initial groundwater level was defined based on field monitoring from piezometric measurements (Figure 80). A rainfall with intensity as depicted in Figure 81 was applied on the slope. The minimum and the maximum pore pressure head respectively are -0.5 m (θ_{min}) and 0.1m (θ_{max}). The lower boundary of the model was assumed as impervious.

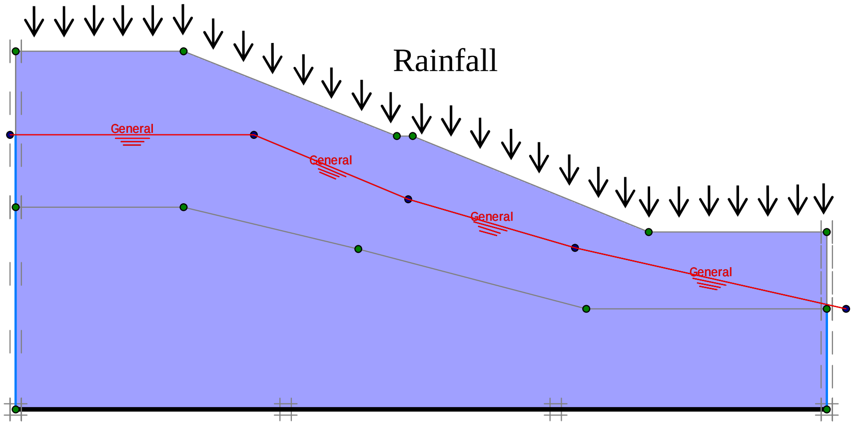

Fig. 80: Boundary conditions of the model

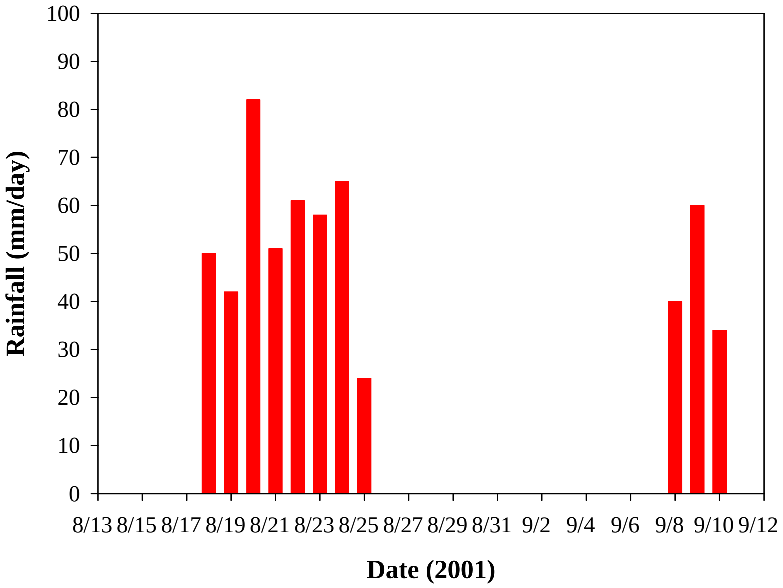

Fig. 81: Intensity of rainfall during the monitoring period

Figure 82 shows the initial suction of model, which is assumed to increase linearly above groundwater level up to the surface. Figure 83 presents the initial degree of saturation which corresponds to the chosen SWCC. R1, R2 and R3 are three rows of instrumentation for pore water pressure (soil suction) and piezometer (groundwater level) monitoring.

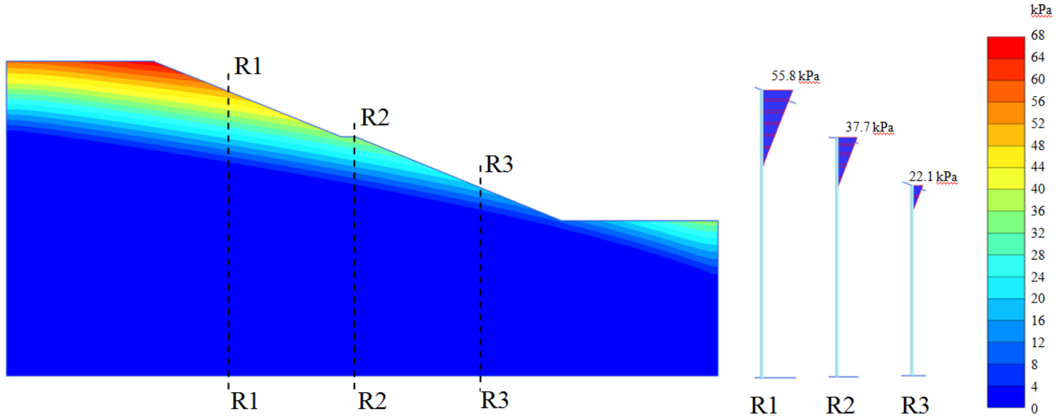

Fig. 82: Initial conditions: suction.

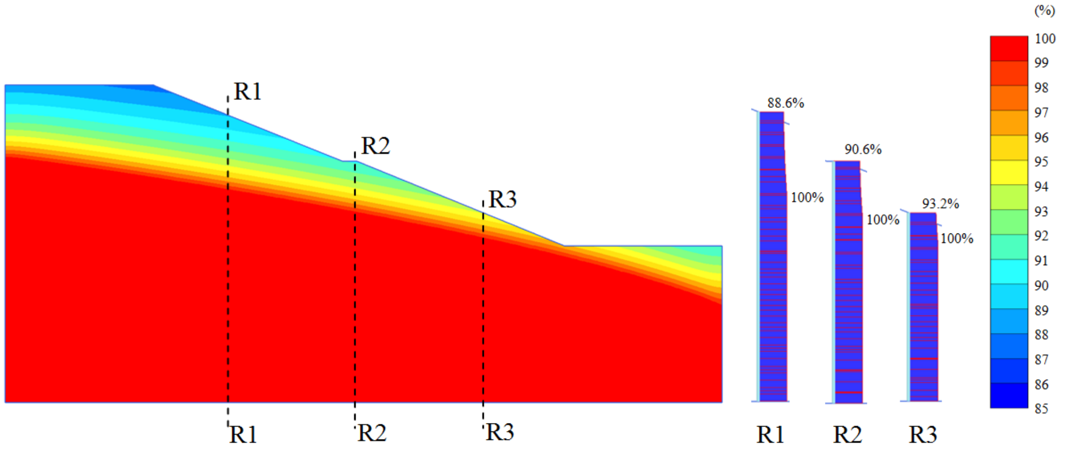

Fig. 83: Initial conditions: degree of saturation.

6.2.3 Results

Response of Pore-Water Pressure

Figures 84a and 84b show the changes in pore water pressure in response of rainfall measured by the tensiometer and calculated by back analysis in the R2 monitoring location. R2-T-0.6, R2-T-1.2, R2-T-1.4, and R2-T-1.6 are the tensiometer measurement of 0.6m, 1.2m, 1.4m, and 1.6m depth respectively. This figure shows that after several days of rainfall, the pore water pressure increases (suction decreases) until the end of the first period of rainfall, and then decreases again during the no rain period. After one day of the second period of rainfall the pore water pressure increases again until the end of the second period of rainfall, and then decreases again after the rainfall was stopped.

The comparison of the results of the back analysis and the measurement in the R2 location is illustrated in Figure 85 for pore-water pressures. The back analysis results agree very well with the observation especially at a depth more than 1 m below the ground surface. Some cracks and fissures were observed to 1 m depth below the ground surface which will influence the result but are not considered in the analysis.

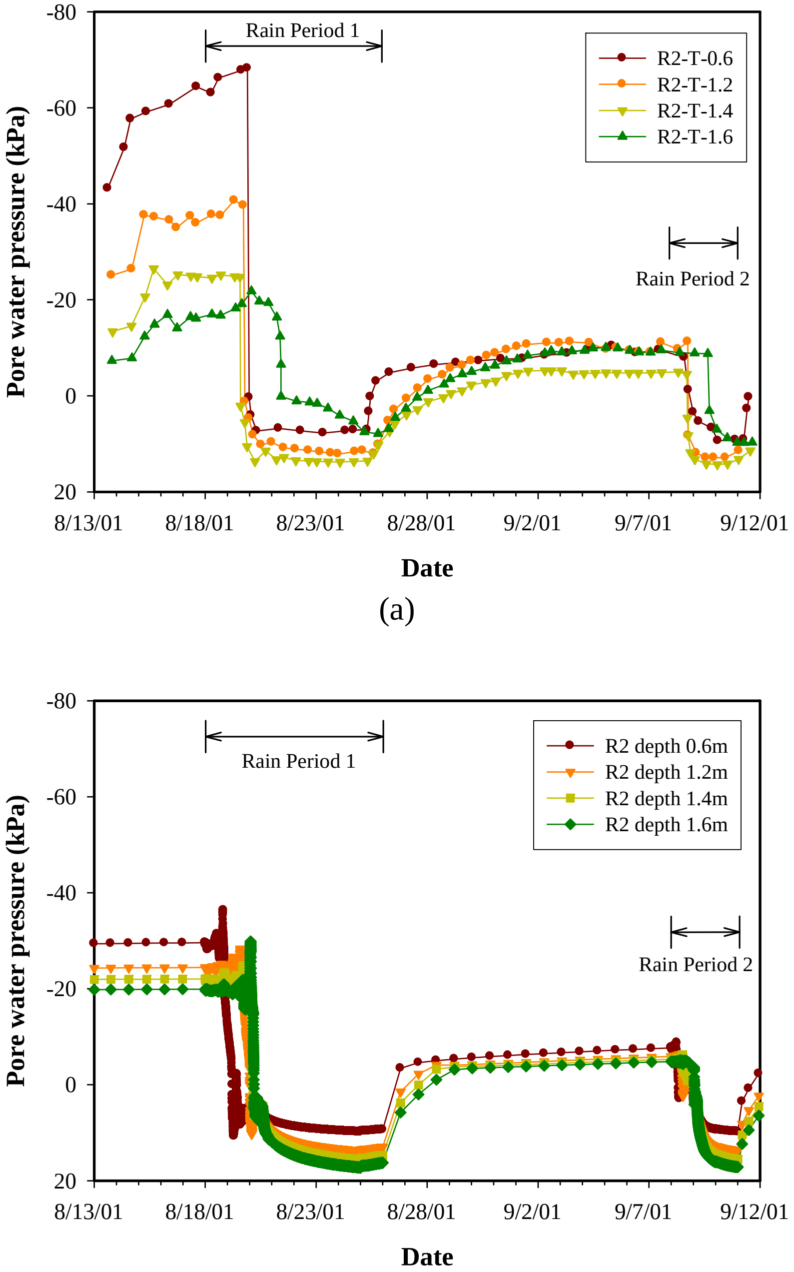

(a)

(b)

Fig. 84: Pore-water pressure changes in response to rainfall located at R2 section; (a) measured by tensiometer; (b) back analysis using FEM

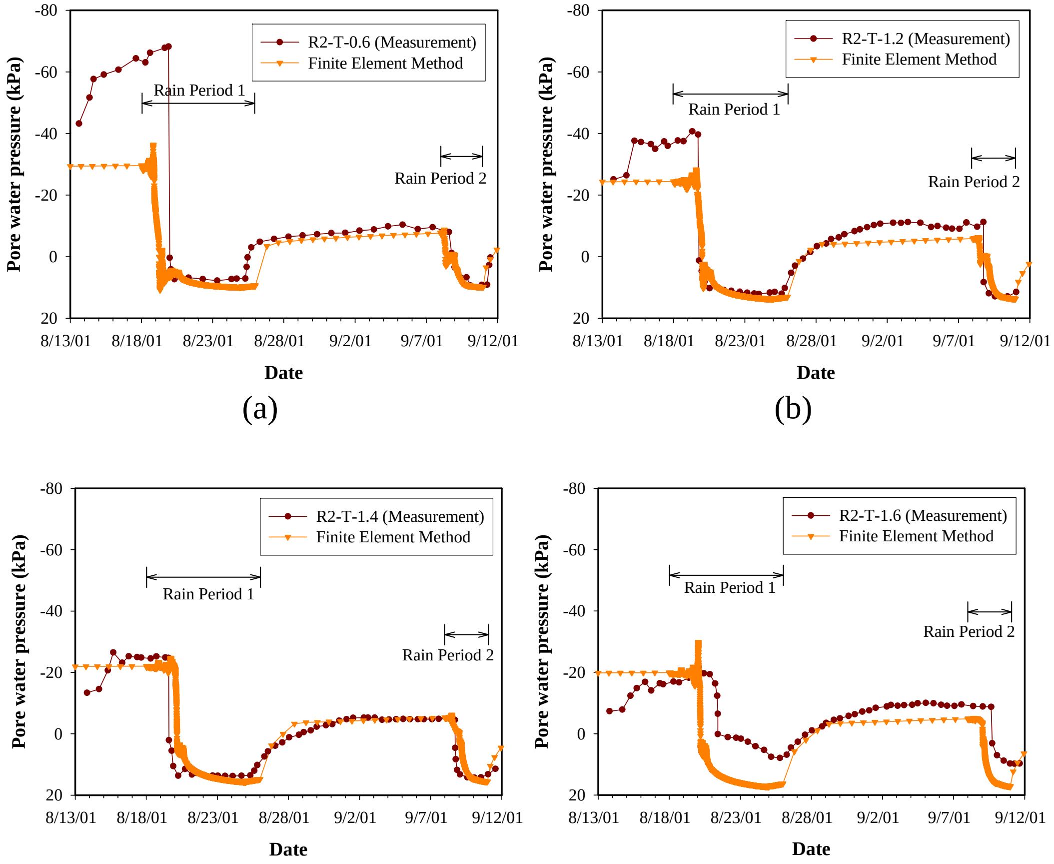

(a) (b)

(c) (d)

Fig. 85: Measured and FEM calculated pore-water pressure changes in response to rainfall, located at R2 with 4 different depths; (a) 0.6m depth; (b) 1.2m depth; (c) 1.4m depth; (d) 1.6m depth

Figure 86 shows the change in pore-water pressure in response to the rainfall in the R1 and R3 monitoring location. In the R1 monitoring location, during the first rainfall, the pore-water pressure in the lower three control points (1.2m, 1.4m, and 1.6m depth) began to increase at the fourth day of the first rainfall period. On the other hand, the upper control point (0.6m depth) showed the pore-water pressure start to increase at the third day of first rainfall period. This indicates that the combined effects of three days of rainfall only dissipate the soil suction above 1.2m depth in the R1 monitoring location. With the small rainfall intensity on the last day of the first rainfall period, the pore-water pressures decrease rapidly followed by a small decrease during the no rain period. The same tendency occurred in the second rainfall period, the pore-water pressure in the lower three control points began to increase at the first day of the second rainfall period. However the pore-water pressure in the upper control point start to increase at the second day of second rainfall period. On the last day of the second rainfall period, the pore-water pressure decrease gradually followed by a small decrease during no rainfall period.

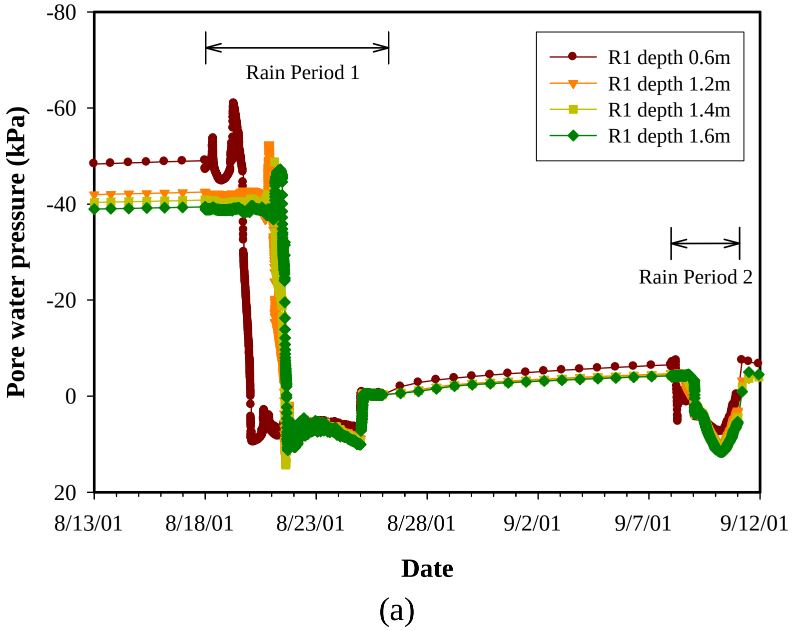

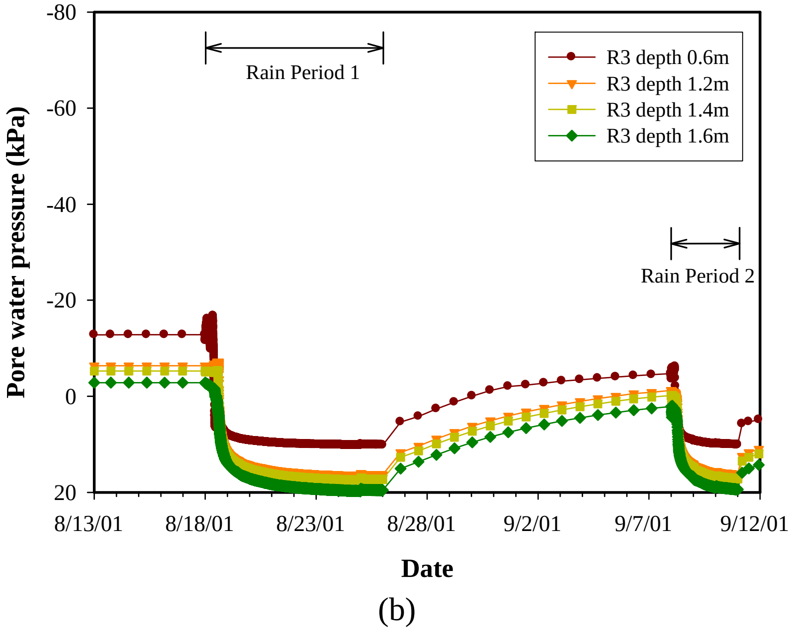

Fig. 86: Pore-water pressure changes in response to rainfall obtained from finite element analysis; (a) R1 monitoring location; (b) R3 monitoring location

In the R3 monitoring location, during the first rainfall, the pore-water pressure in all control points (0.6m, 1.2m, 1.4m, and 1.6m depth) began to increase rapidly at the first day of the first rainfall period. This is caused by the position of R3 monitoring location at the lower part of the slope with the small initial soil suction, consequently the soil suction will dissipate almost in the same time at all control points during the rainfall. The pore-water pressure in all control points start to decrease gradually after the first rainfall period was stopped. The same tendency also occurred in the second rainfall period.

Figure 87 illustrate the change of negative pore-water pressure (suction) and degree of saturation during the monitoring period as obtained from the back analysis. The scaling in these figures (change of suction and degree of saturation) correspond to Figures 82 and 83.

Response of Groundwater Level

Figures 88 and 89 show the variations of piezometric level in response of rainfall measured by tensiometers and calculated by back analysis respectively.

After the first rainfall started, the piezometric level from the observed and the back analysis at three location of monitoring R1, R2 and R3 increased due to the decrease in negative pore-water pressure. The piezometric level decreased with reduction in the elevation. This indicates a down-slope water flow. During the non-rainfall period, the amount of the difference in the groundwater level at the three monitoring location still remained the same, although there was a small recovery of negative pore-water pressures in the soil. This also indicates a down-slope water flow after the rainfall.

Figure 89 illustrates the comparison of the back analysis results and the measurement in the R1, R2 and R3 locations for piezometric (groundwater) level. The comparison is quite reasonable, although before the first rainfall period there is a significant difference in the location R3. This is probably caused by the presence of a number of opened cracks and fissures near the ground surface in this area.

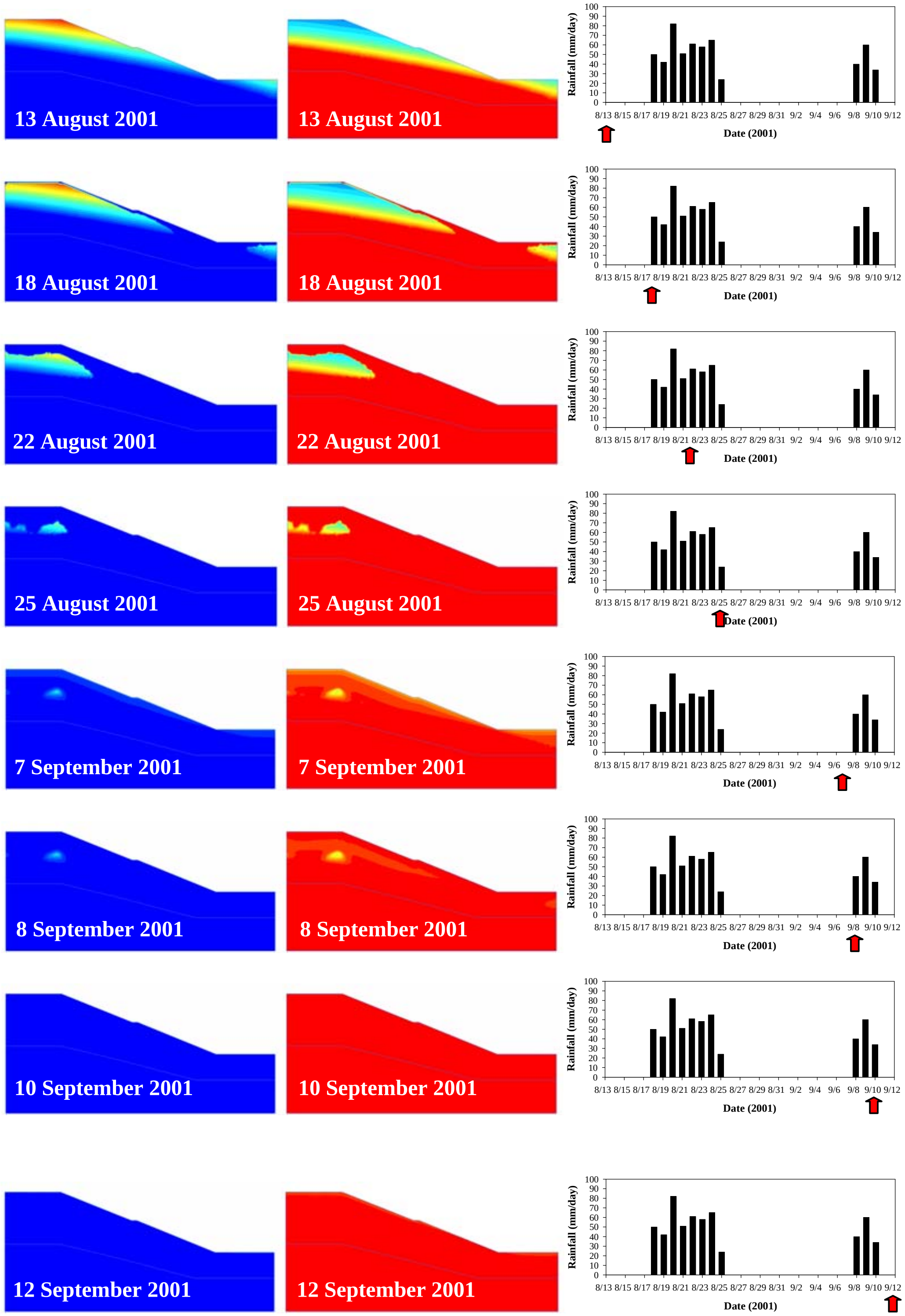

Fig. 87: Calculated change of suction and degree of saturation during monitoring period

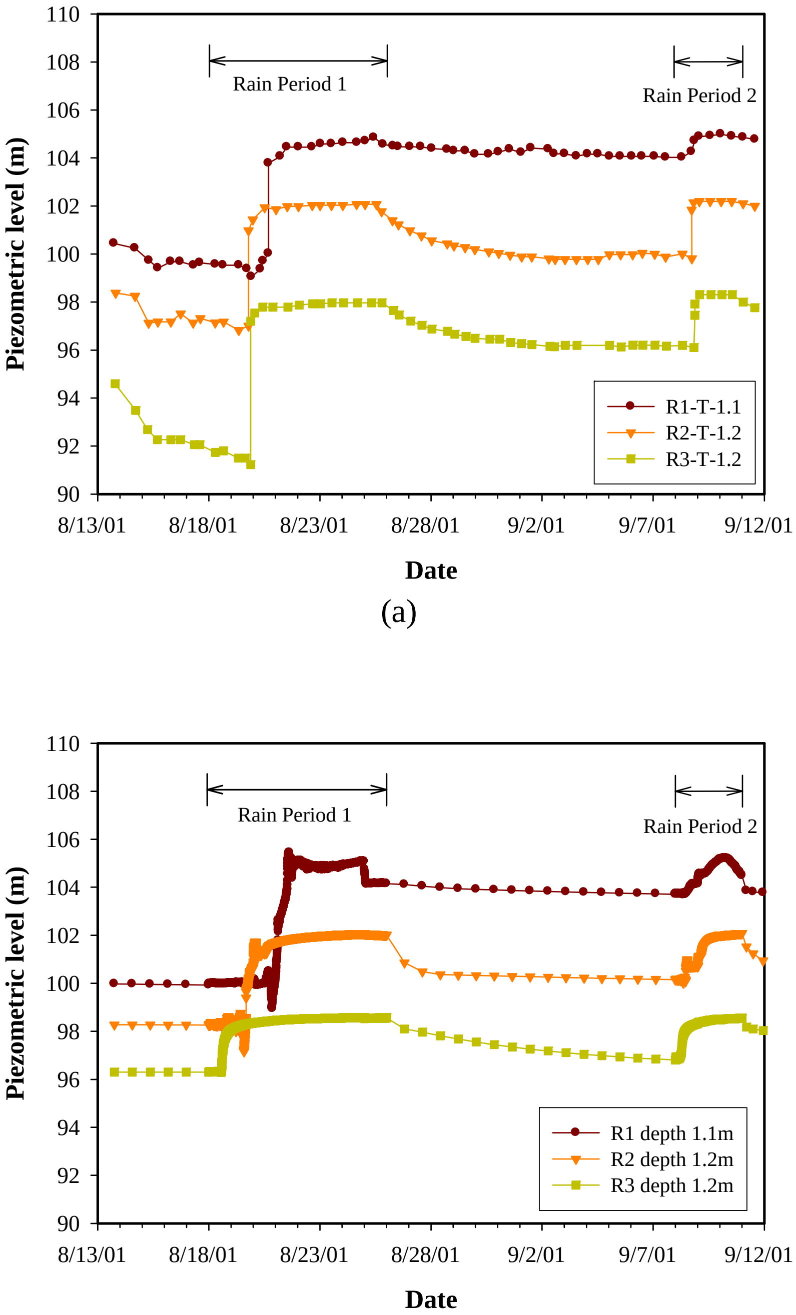

(a)

(b)

Fig. 88: Piezometer level changes in response to rainfall located at R1, R2, and R3 section; (a) measured by tensiometer; (b) back analysis using FEM

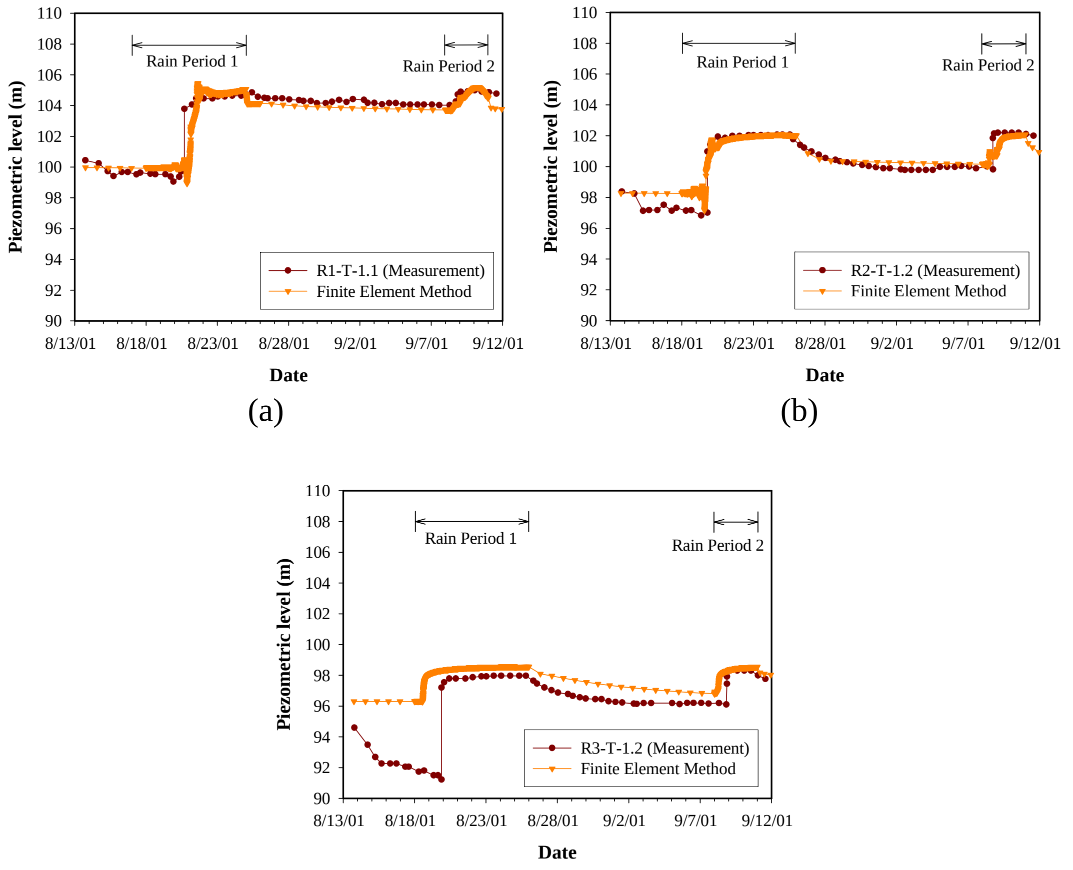

(a) (b)

(c)

Fig. 89: Measured and FEM calculated of piezometric level changes in response to rainfall at monitoring location: (a) R1 (1.1m depth); (b) R2 (1.2m depth); (c) R3 (1.2m depth)

Response of horizontal displacements

Figures 90 and 91 show the horizontal displacement in response to simulated rainfalls measured by inclinometer and calculated by back analysis respectively. Three values of the soil stiffness of the upper clay layer are used in the back analysis, they are 6000 kPa, 7500 kPa, and 10000 kPa. The results indicate that the ground moves towards the down-slope displacement. The variations of horizontal displacement profiles were consistent with changes of pore-water pressure. During the first rainfall period, there was significant increase in horizontal displacement from 19 August to 25 August. During no rainfall period, such as on 7 September, a slight recovery of the horizontal displacements was observed owing to the increase of soil suction. During the second period of rainfall, the horizontal displacement increase with the decrease of soil suction. It follows from Figure 90a that a sliding plane in a depth of approximately 5.5m developed between 21 and 25 August.

Figure 91 illustrates the comparison of horizontal displacements between the back analysis results and the inclinometer measurement. The results are not as good as the pore-water pressure and the piezometric level comparison. The tendency of the horizontal displacements are reasonable only until 21 August where the horizontal displacements increase during the rainfall period.

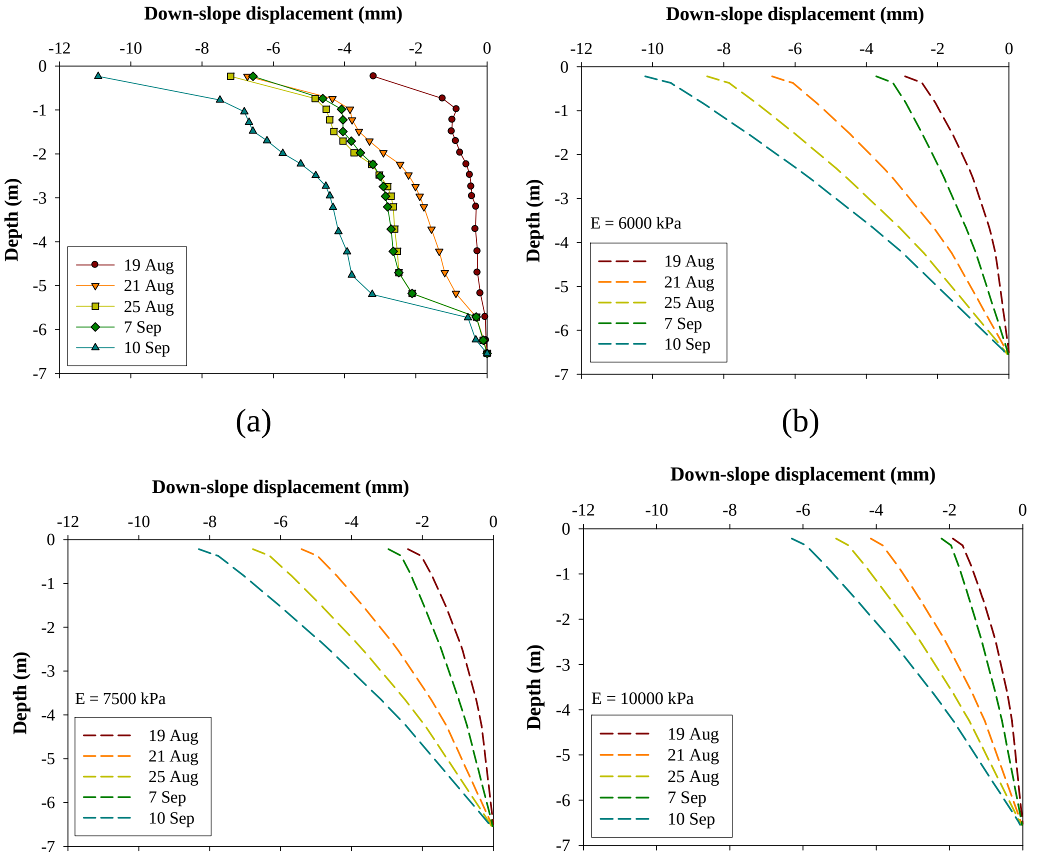

(a) (b)

(c) (d)

Fig. 90: Horizontal displacement in response to rainfall; (a) measured by inklinometer; (b) FEM with E = 6000 kPa; (c) FEM with E = 7500 kPa; (d) FEM with E = 10000 kPa

However, the distinct kink in the displacement profile shown by the measurement of 25 August could not be reproduced by the simple elastic-perfectly plastic constitutive model and therefore the displacement pattern does no longer agree with measurements. Furthermore the recovery of displacement in the dry period is unrealistic. This again emphasizes the need of applying a more advanced constitutive model in order to assess deformations during rainfall and no rainfall periods.

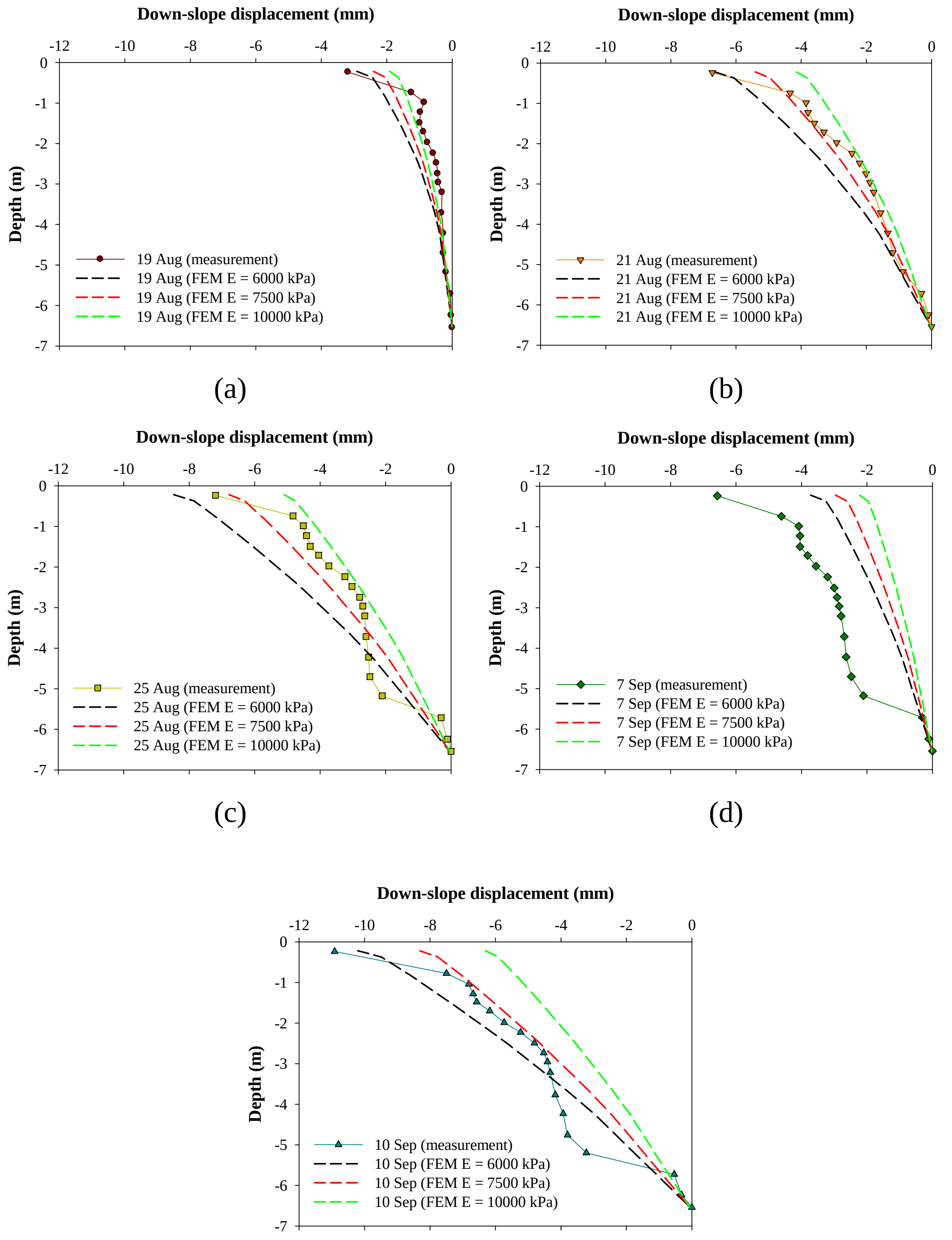

(a) (b)

(c) (d)

(e)

Fig. 91: Measured and FEM calculated horizontal displacement in response to rainfall on: (a) 19 August; (b) 21 August; (c) 25 August; (d) 7 September; (e) 10 September

Stability Analysis

Figure 92 shows the changes in the factor of safety (FOS) during the monitoring period. During the first period of rainfall, the FOS of the slope reduces by 18% from 1.99 to 1.64 and then during no rainfall period, the FOS increases by 11% to 1.84. During the second period of rainfall, the FOS of the slope decreases by 21% to 1.46 and then increases again during the no rainfall period.

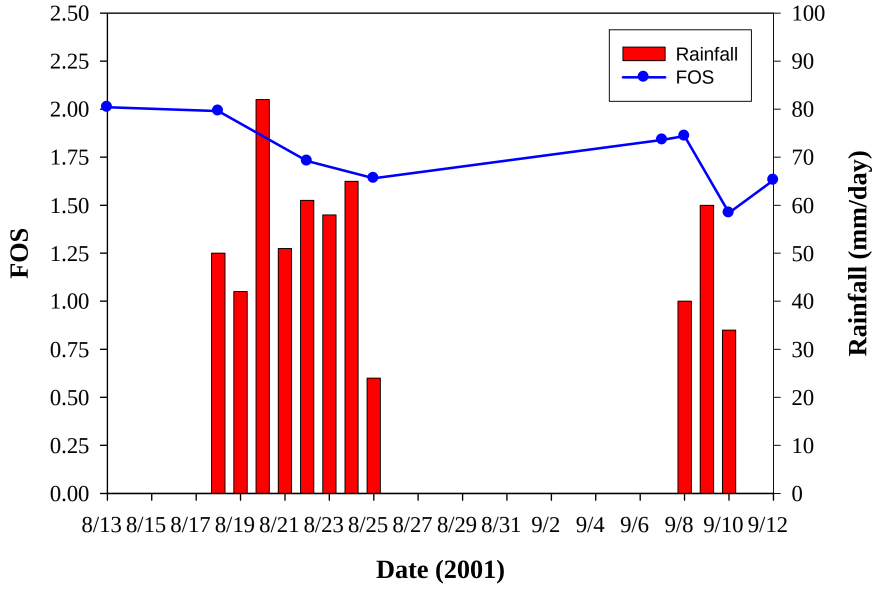

Fig. 92: Change of the FOS of slope during monitoring period

Figure 93 illustrates the calculated failure mechanisms and it follows that the changes in the suction profile due to rainfall infiltration will influences the factor of safety.

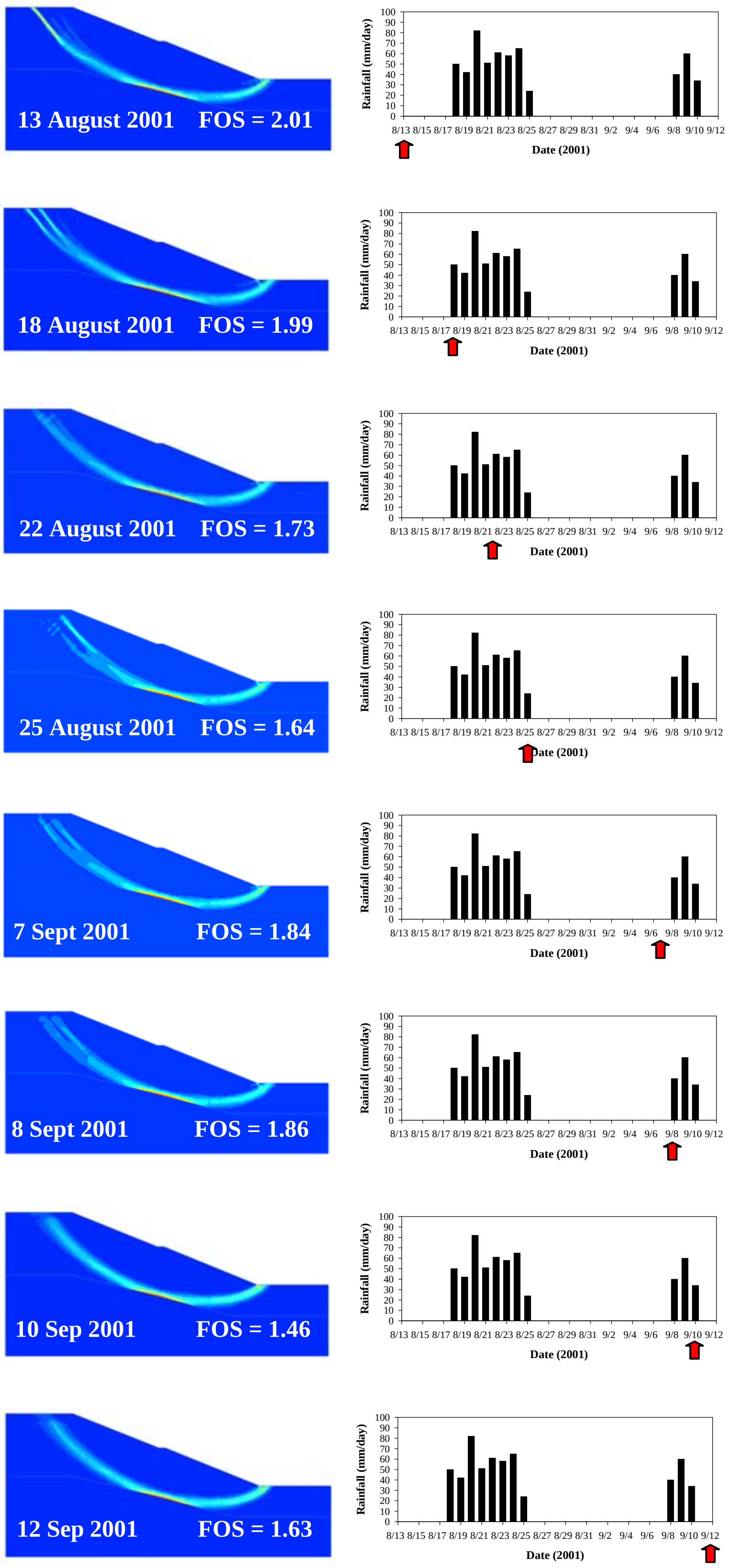

Fig. 93: Calculated failure mechanism and FOS of the slope during monitoring period

6.3 Summary

The comparison between a back analysis performed with the finite element method and in-situ measurements of a field trial investigating the effect of rainfall infiltration in a slope showed good agreement for pore-water pressures and groundwater levels. Small differences are probably caused by cracks and fissures observed in particular up to 1 m depth below the ground surface which are not considered in the back analysis.

Response in pore-water pressure from the observed and the back analysis generally showed a 1-3 delay related to the initiation of the rainfall event. The combine effects of the first 3 days of rainfall (i.e. about 180 mm) were much more significant than the effect of the ongoing rainfall or the second rainfall event. Response in groundwater level from the observed and the back analysis indicated a down-slope water flow. The groundwater level increased due to the decrease of negative pore-water pressure.

The comparison of horizontal displacement between the back analysis and the inclinometer measurement in response to simulated rainfalls showed reasonable agreement only for early stages. Results indicate that the ground moves downwards and the horizontal displacements were dependent on the changes of pore-water pressures. The horizontal displacements increase with the decrease of soil suction during rainfall period. However, measurements indicated the occurrence of a distinct sliding plane at some stage which could not be captured by the Mohr-Coulomb model applied. Also the recovery of displacements in the no rainfall period was significantly overestimated.

The stability of the slope during monitoring period showed that the FOS of the slope decreases during rainfall period and increases during no rainfall period. The variations of the FOS of the slopes were also dependent on changes of pore-water pressure.

From the results above, the finite element method with a fully coupled flow-deformation analysis can be valuable tool to analyze unsaturated soil slope stability subjected to rainfall infiltration. This method can be used to predict the pore-water pressures, the ground water level and to some extent displacements of unsaturated slopes subjected to rainfall infiltration.

7 Slope stability analysis considering drawdown conditions

Water pressure such as pore-water pressure and surface water pressure have a large influence in slope stability analysis. Pore-water pressure will act as internal force and surface water pressure will act as external force in slope stability analysis. These pressures can change as the water level changes (water drawdown conditions).

In practice, the fully slow and the fully rapid drawdown are commonly evaluated in slope analysis considering drawdown conditions. With these conditions, the computed FOS's may be under or over estimated as compared to transient drawdown conditions.

Berilgen (2006) investigated the slope stability under drawdown conditions varying different factors such as the soil permeability, drawdown rate, and drawdown ratio. The finite element method with a semi coupled saturated groundwater flow and deformation analysis were used in the analysis. Two different heights of slopes, H (7 m and 14 m), two different drawdown rates, R (1 m/day and 0.1 m/day) and two different soils permeability ($k_{sat} = 10^{-4}$ m/day and $k_{sat} = 10^{-6}$ m/day) were employed in the analysis. The results showed that the soil permeability and drawdown rate have a large influence in the slope stability when transient drawdown conditions are considered. The stress-induced pore pressure in highly permeability soils dissipate during drawdown. In low permeability soils, seepage-induced and stress-induced pore-water pressures are not likely to dissipate at the same rate with the external water level changes.

Slope stability under drawdown conditions have been investigated by Alonso and Pinyol (2009) with four calculation procedures. These procedures are instantaneous drawdown, pure flow, coupled flow-elastic, and couple flow-elastoplastic calculation. Compared with measured pressure records, the coupled analysis provided a consistent and reasonable solution for saturated and unsaturated conditions.

The main objective of this section is to evaluate the influence of hydraulic parameters on slope stability during drawdown (transient drawdown) with different factors (drawdown rate and drawdown ratio) for unsaturated conditions. The result will be compared with rapid and slow drawdown conditions. In transient drawdown conditions, the analysis is performed with the finite element method using fully coupled flow-deformation analysis. The factor of safety is calculated by means of the shear strength reduction technique.

7.1 Numerical model

In this section, slope stability analysis under drawdown conditions will be discussed. A simple case of a homogeneous slope has been chosen. The international soil classification system USDA series is used for determining the hydraulic parameters for the analysis. The mechanical and hydraulic models used in the analysis are the Mohr Coulomb failure criterion and the Van Genuchten model respectively.

7.1.1 Geometry, finite element mesh and material properties

The height of the slope is 10 m and the gradient (horizontal to vertical) is 2:1. Figure 94 shows the geometry and the two dimensional finite element mesh consisting of 2119 15-noded elements.

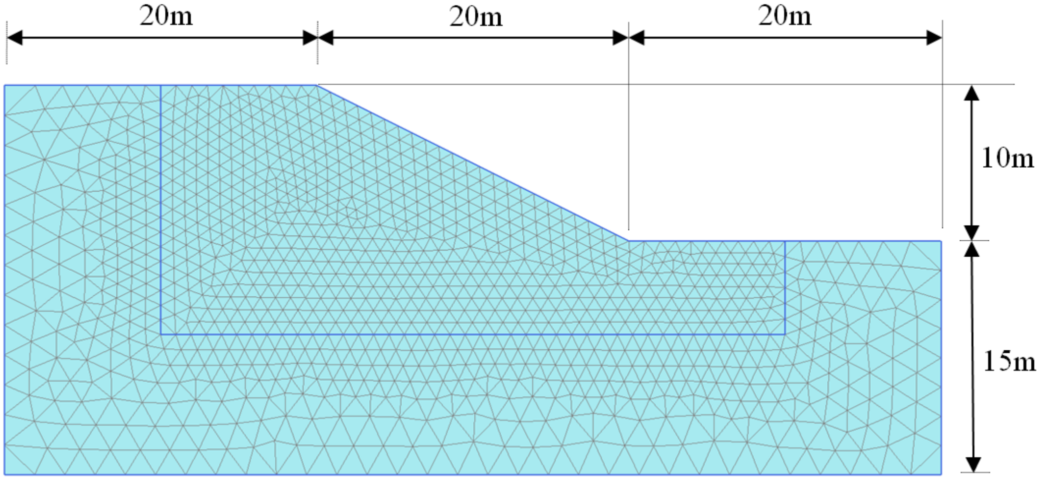

Fig. 94: Geometry and finite element mesh of the slope

In this section, two different hydraulic parameter sets of the USDA series for the Van Genuchten Models are used to evaluate the effect of these parameters in slope stability during transient drawdown conditions, namely silty clay and sandy clay as given in Table 15. The saturated hydraulic conductivity of these soils are $k_{sat} = 5.5\times10^{-8}$ m/s and $k_{sat} = 3.3\times10^{-6}$ m/s, respectively. For simplicity it is assumed that these soils have the same shear strength and stiffness parameters. Soil parameters for the Mohr Coulomb model used in the analysis are given in Table 19.

Tab. 19: Soil Parameters for Mohr Coulomb Model

Description	Symbol	Unit	Value
Unit weight	γ	[kN/m^3]	20
Elasticity modulus	E’	[kPa]	7500
Effective poisson's ratio	ν'	[-]	0.35
Effective cohesion	c'	[kPa]	20
Effective friction angle	ϕ'	[^{o}]	20

7.1.2 Boundary conditions

The initial ground water table was assumed to be horizontal at level of the crest of the slope. The left boundary, right boundary and lower boundary of the model were assumed impervious boundaries (Figure 95).

To evaluate the influence of drawdown on the slopes, FEM analysis were performed for three different conditions as shown in Fig. 95. In this analysis, a slope with two different drawdown rates R (1 m/day and 0.1 m/day) as demonstrated by Berilgen (2006) and Huang & Jia (2009) and several different values drawdown ratios L/H varying from 0.0 (slope completely submerged with water level at the crest of the slope) to 1.0 (water level at the toe of the slope) were considered.

For the first condition, illustrated in Figure 95a, the soil is considered to behave fully drained during drawdown, which is called the fully slow drawdown. For the second condition, illustrated in Figure 95b, the soil is considered to be undrained, which is called the fully rapid drawdown. These conditions represent the extreme situations. For these two cases, groundwater flow and consolidation analyses are not taken into account in the stability analysis. For the general (transient) drawdown case shown in Figure 95c, the fully coupled groundwater flow and deformation analysis were carried out.

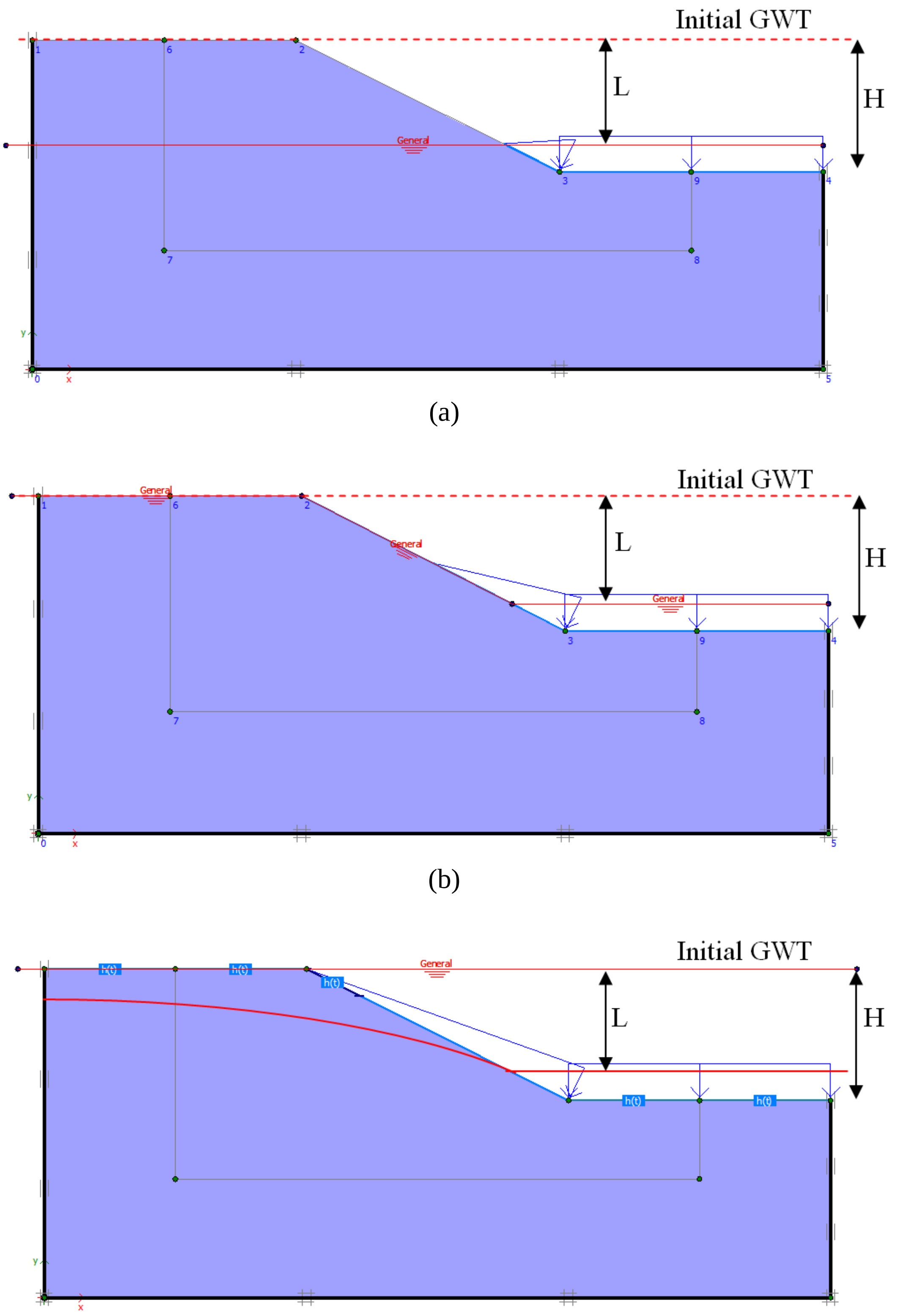

(a)

(b)

(c)

Fig. 95: Boundary conditions of the model; (a) fully slow drawdown condition; (b) fully rapid drawdown condition; (c) transient drawdown condition

7.1.3 Results

Fully slow and rapid drawdown conditions

Figure 96 and 97 illustrate the failure mechanisms of slopes for slow drawdown and rapid drawdown conditions respectively. Table 20 and Figure 98 show the variation of the factor of safety (FOS) of these conditions with different drawdown ratios.

In slow drawdown condition, the factor of safety reaches a minimum when L/H = 0.7. The fully submerged slope (L/H = 0) is more stable than the dry slope (L/H = 1) as indicated by a higher FOS. The tendency of this result is similar to the example shown in chapter 2.

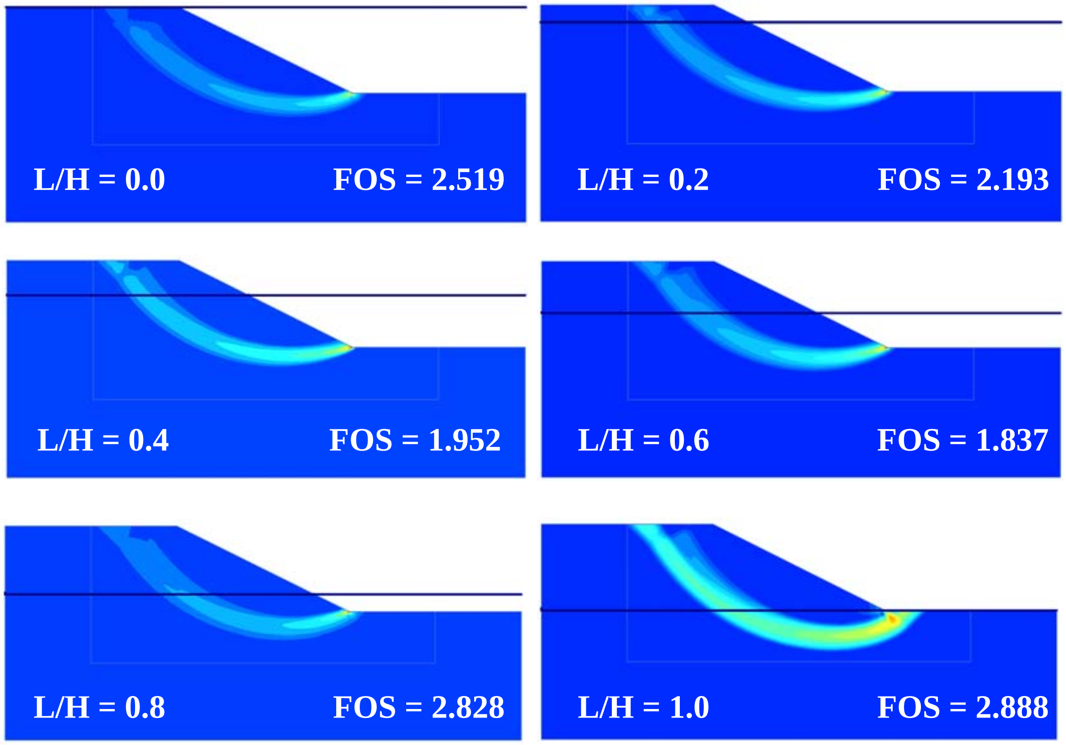

Fig. 96: Failure mechanism of the slopes for slow drawdown condition

In rapid drawdown condition, the change of hydrostatic pressure against the slope surface also generates a change in effective stress inside the slope. This stress change will generate a change in pore-water pressure. The effective stress decreases due to the decrease of hydrostatic pressure against the slope surface. Reduced of effective stress also will reduce the FOS of the slope. When the drawdown ratios (L/H) increase, the FOS will decrease.

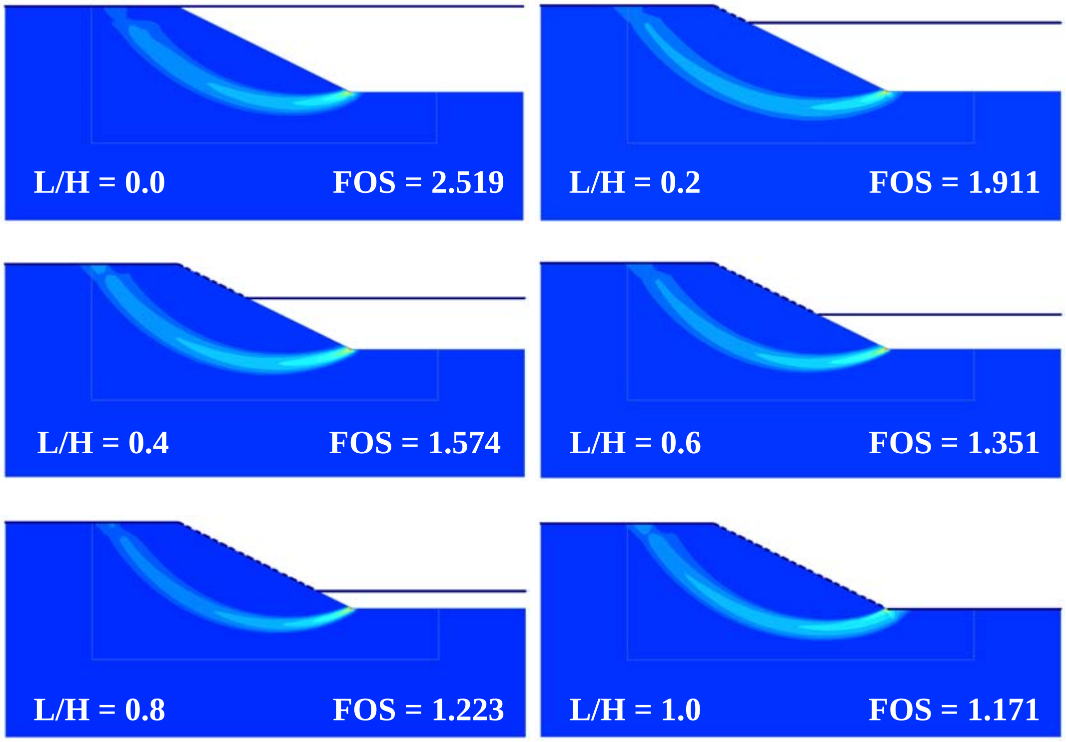

Fig. 97: Failure mechanism of the slopes for rapid drawdown condition

Tab. 20: Variation of FOS for fully slow and rapid drawdown conditions

L / H	FOS	
	Fully Slow Drawdown	Fully Rapid Drawdown
0.0	2.519	2.519
0.1	2.356	2.135
0.2	2.193	1.911
0.3	2.052	1.724
0.4	1.952	1.574
0.5	1.880	1.449
0.6	1.837	1.351
0.7	1.820	1.276
0.8	1.828	1.223
0.9	1.850	1.188
1.0	1.888	1.171

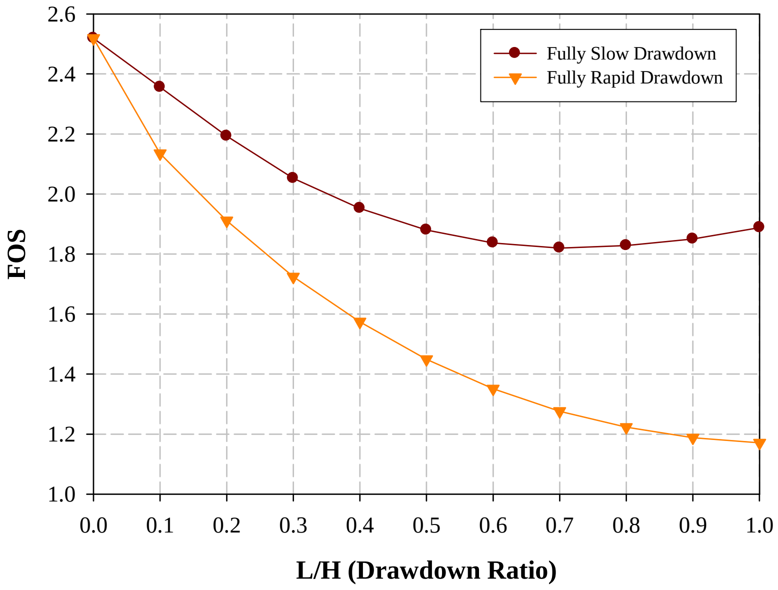

Fig. 98: Change of FOS of the slope with different drawdown ratio for fully slow and rapid drawdown conditions.

Figure 99 shows the variation of normalized changes in pore-water pressures (normalized with respect to initial pore-water pressures) $(p_{wo}-p_w)/p_{wo}$ for fully slow drawdown condition. The figure shows that the normalized changes in pore-water pressures above the water level with all drawdown ratios (L/H) are equal to 1. This illustrates fully drained conditions in the soil above the water level. The normalized changes in pore-water pressures below the water level at the same level remain the same, since the position of the phreatic surface is horizontal. This condition generates a line of variation of changes in pore-water pressures with all drawdown ratios. At the toe elevation of the slope, the normalized changes in pore-water pressures with drawdown ratio L/H = 0.2, 0.4, 0.6, 0.8 and 1.0 are 0.2, 0.4, 0.6, 0.8, and 1.0 respectively.

The different shapes of the variation of normalized changes in pore-water pressures for fully rapid drawdown condition are illustrated in Figure 100. The phreatic surface positions are assumed at the ground surface of the slope for all drawdown ratios. The normalized changes in pore-water pressures above and below the water level varies within a certain margin and this margin depends on the water level or drawdown ratio. When the drawdown ratio increases, the margin below the water level will increase as well. The margin of normalized changes in pore-water pressures for the drawdown ratio L/H = 0.2 at the elevation of toe of the slope is between 0.05 and 0.2. When the drawdown ratios increase, the margin becomes wider. The maximum margin of normalized changes in pore-water pressure at the elevation of toe of the slope with the drawdown ratios L/H = 0.4, 0.6, 0.8, and 1.0 are 0.4, 0.6, 0.8, and 1.0

respectively. These maximum margins are equal to the change in pore-water pressure at the toe of the slope for fully slow drawdown conditions.

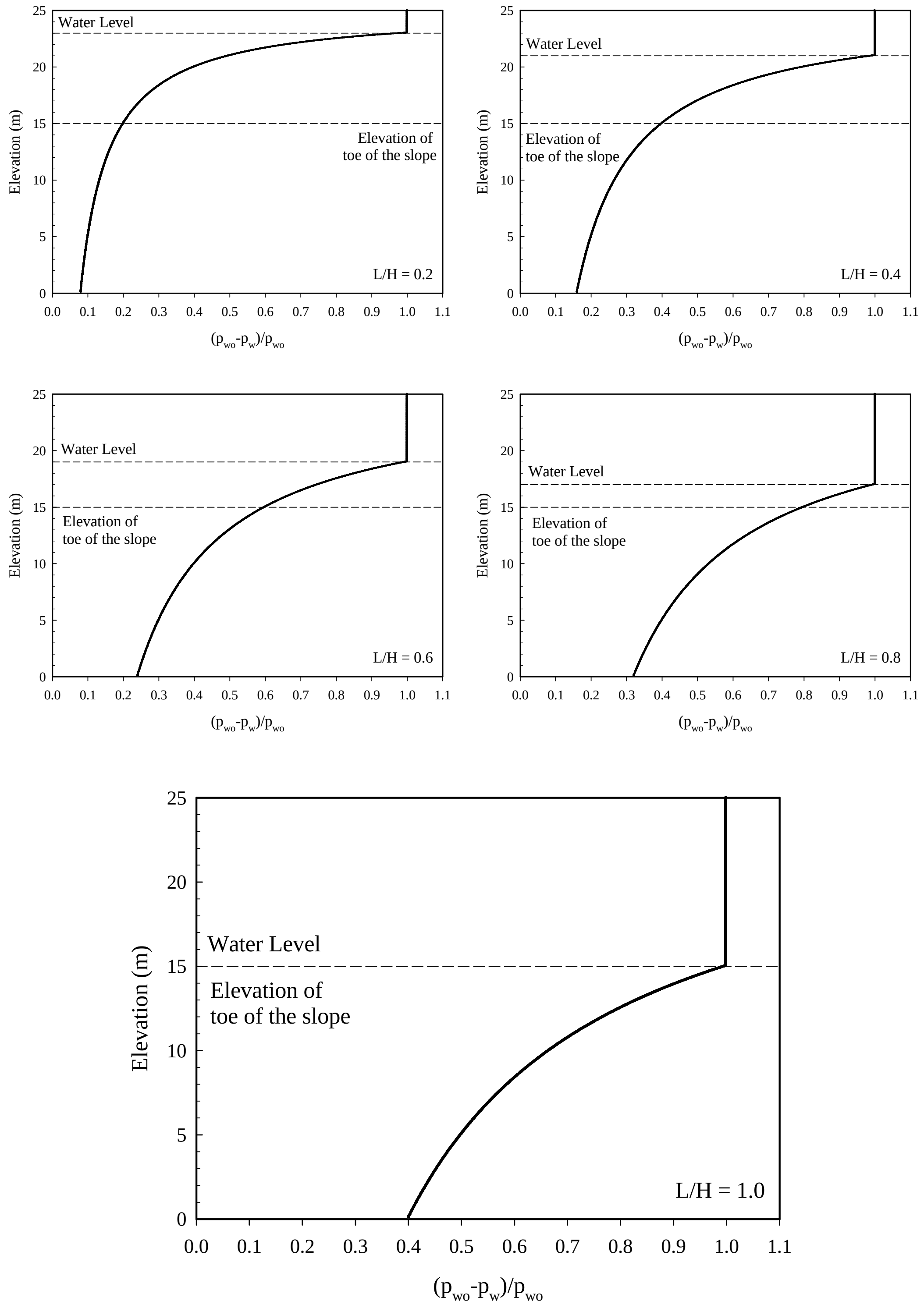

Fig. 99: Variation of normalized changes in pore-water pressures for fully slow drawdown conditions.

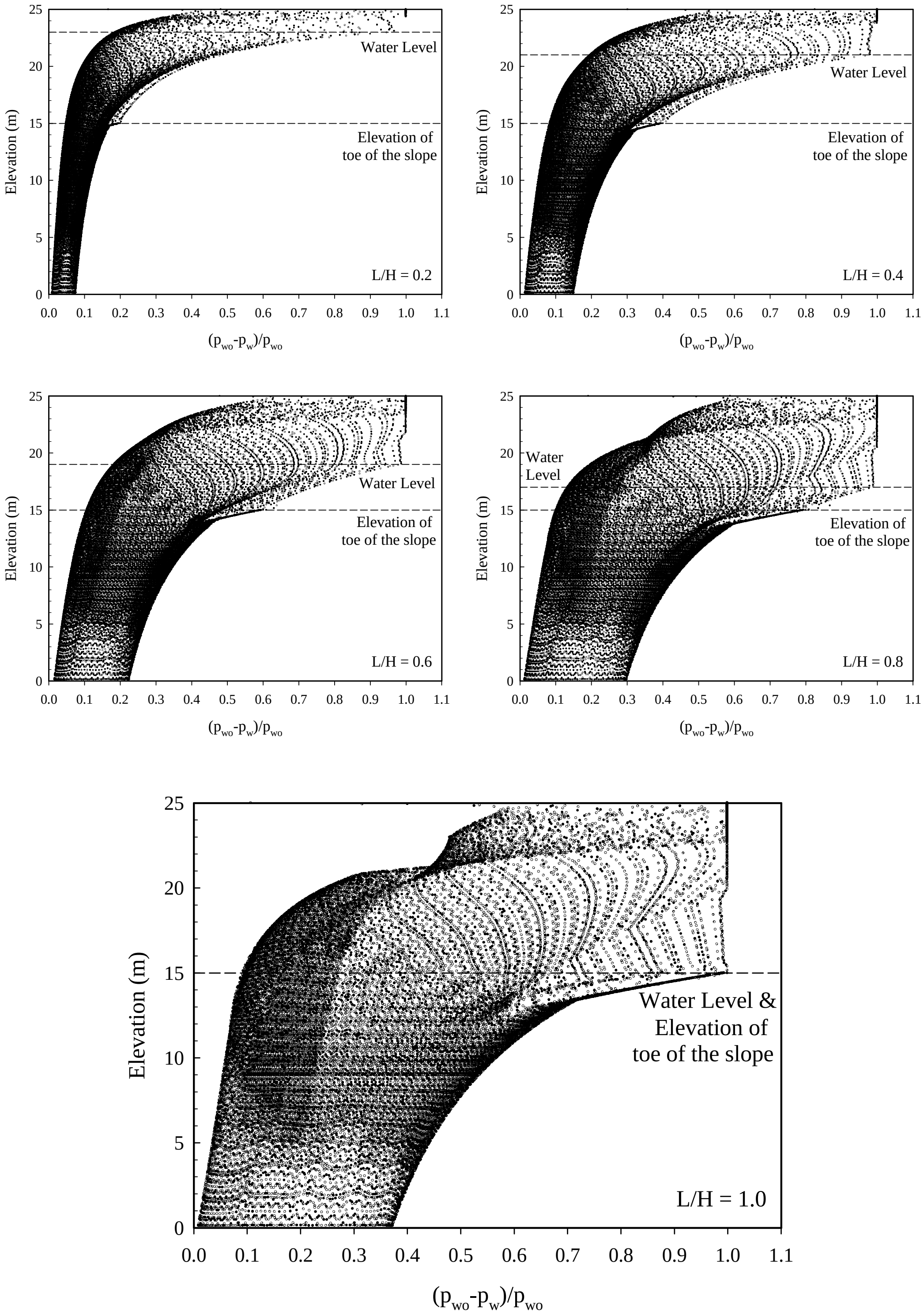

Fig. 100: Variation of normalized changes in pore-water pressures for fully rapid drawdown conditions.

Transient drawdown condition for the silty clay slopes

The failure mechanisms and the change of degree of saturation of the slopes for a transient drawdown condition with hydraulic parameters as a silty clay (k_{sat} = 5.5×10^{-8} m/s) and two different drawdown rates R = 1 and R = 0.1 m/day are illustrated in Figures 101 and 102, respectively.

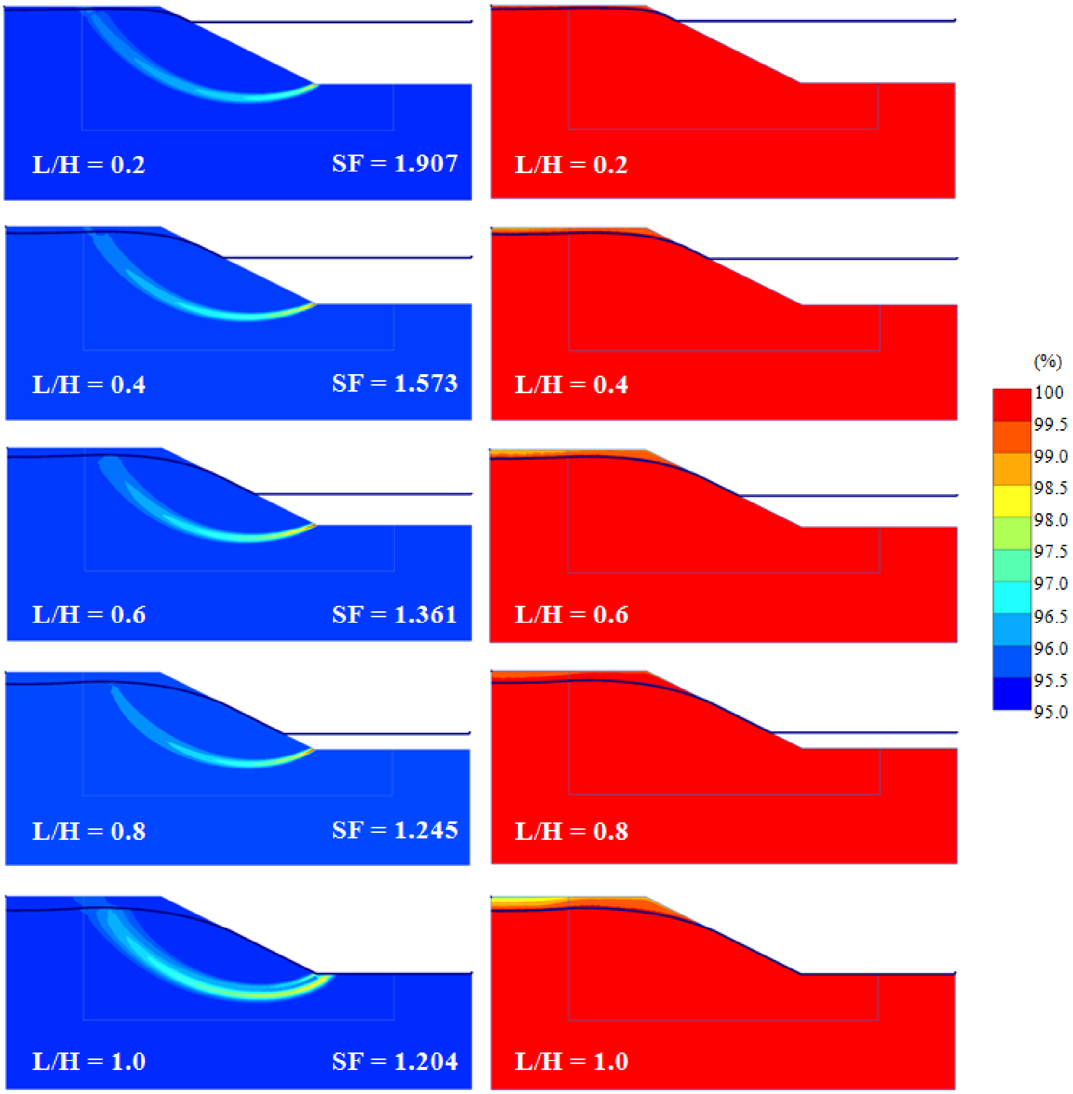

Fig. 101: Failure mechanism and change of degree saturation for silty clay slope during transient drawdown condition (R = 1 m/day)

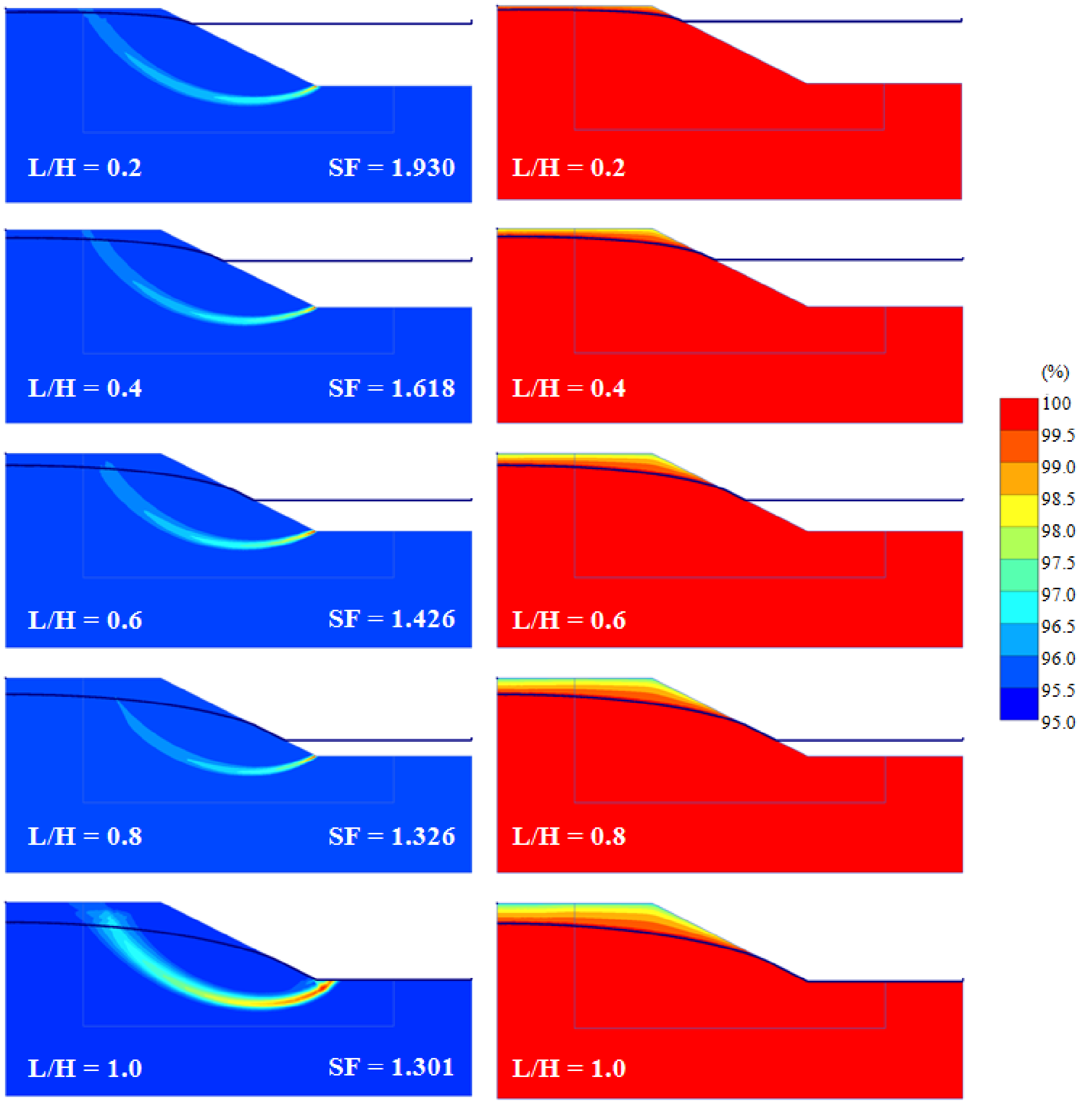

Fig. 102: Failure mechanism and change of degree saturation for silty clay slope during transient drawdown condition (R = 0.1 m/day)

The changes in pore-water pressure during transient drawdown conditions will influence the safety factor of the slopes. Figures 103 and 104 illustrate the variations of normalized changes in pore-water pressures with different drawdown ratios (L/H) and drawdown rates (R) for the silty clay slope during transient drawdown conditions.

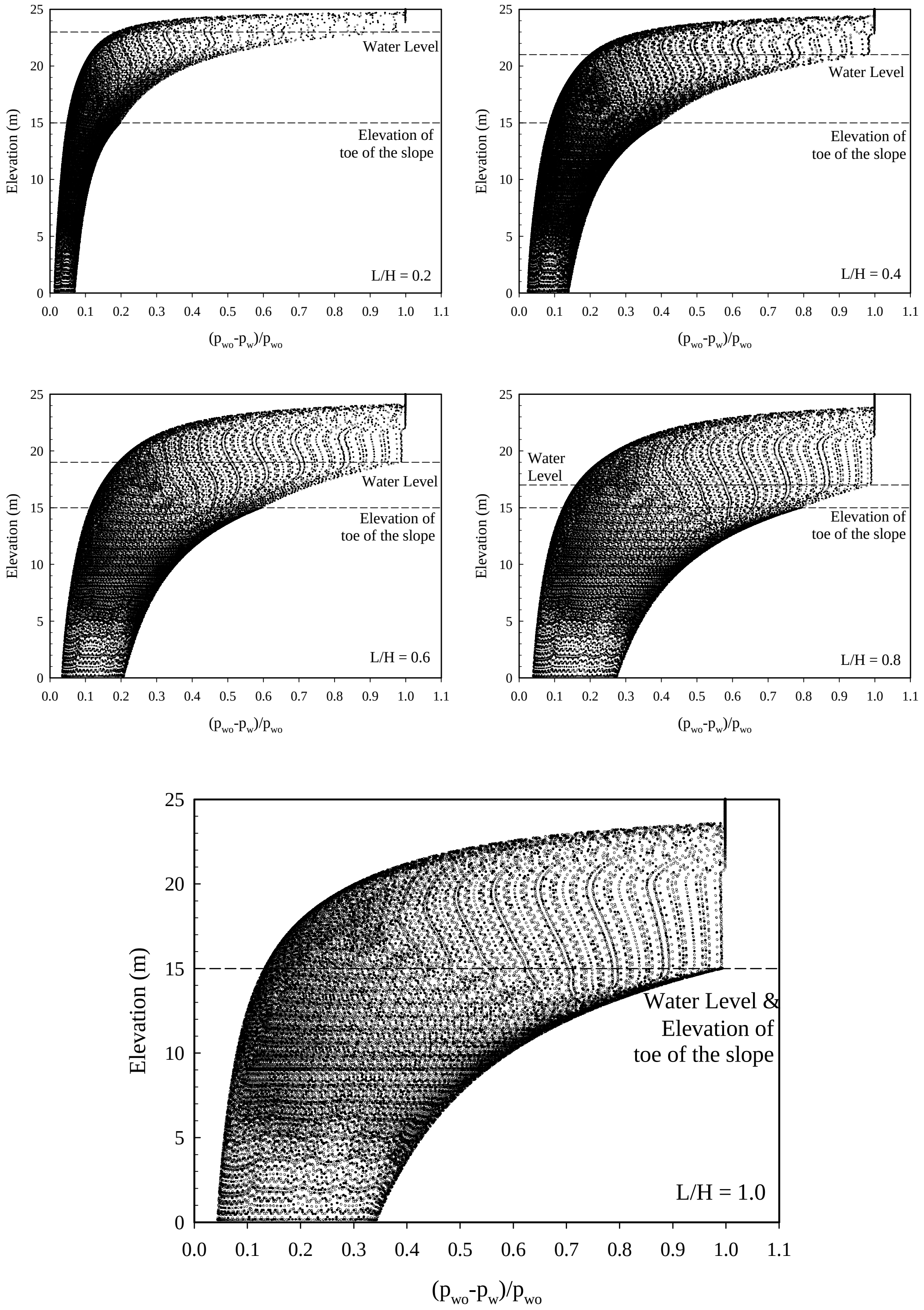

Fig. 103: Variation of normalized changes in pore-water pressures for silty clay slope with drawdown rate R = 1 m/day

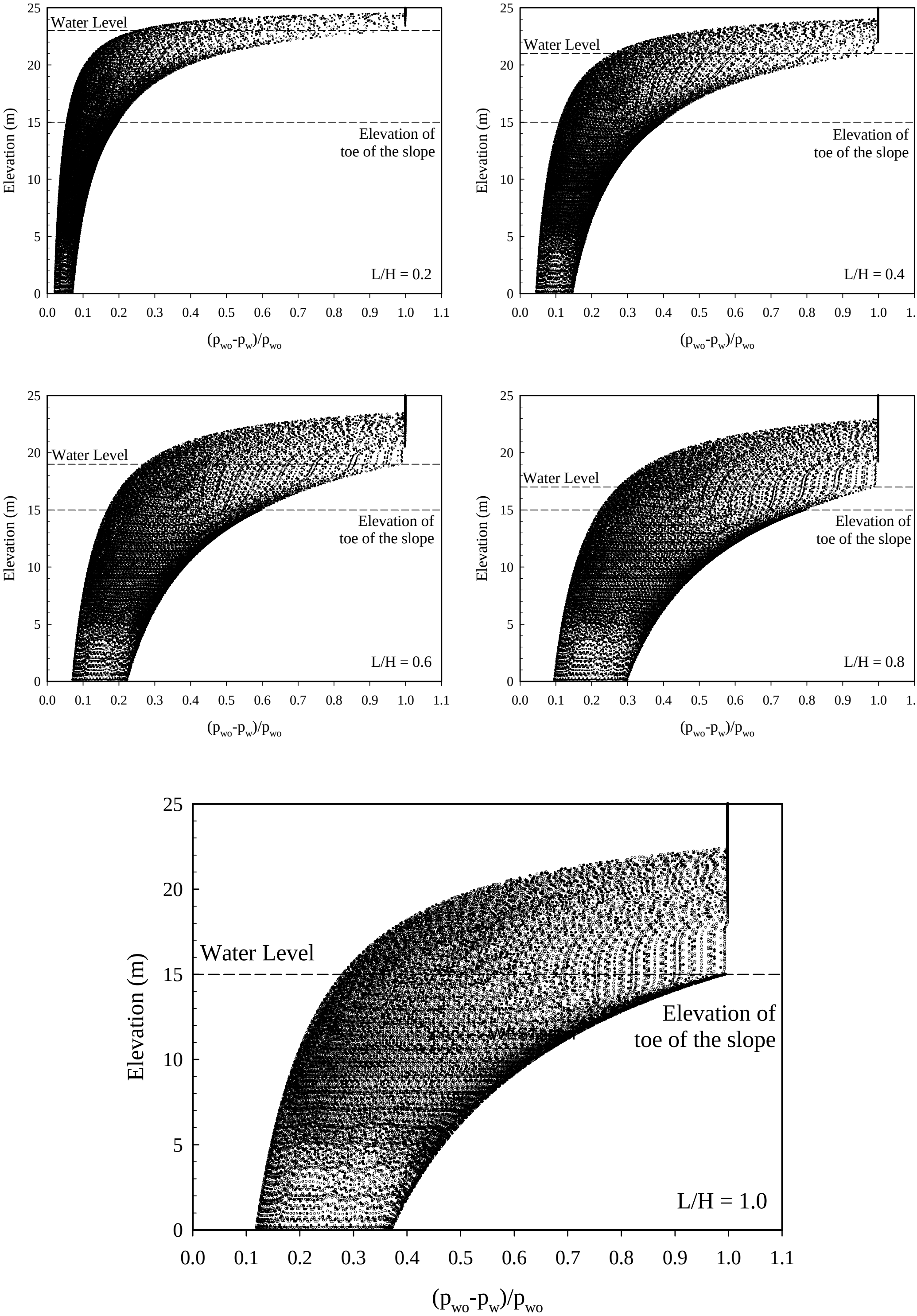

Fig. 104: Variation of normalized excess pore pressure for silty clay slope with drawdown rate R = 0.1 m/day

Figure 103 shows the variation of normalized changes in pore-water pressures for silty clay slopes with high drawdown rate of R = 1 m/day. In general, the shapes of these variations are similar with a fully rapid drawdown condition (see Figure 100) but with smaller margins of normalized changes in pore-water pressures below the water level. This illustrates that the phreatic surface at the slope is close to the ground surface for all drawdown ratios (see Figure 101). Thus only some drainage occurs in the soil slope and the condition comes close to fully rapid drawdown condition. Therefore, the FOS of the slope will be close to the value for the fully rapid drawdown. However, a small drainage will increase the effective stress on the slope, therefore the FOS of the slope will be slightly higher than the fully rapid drawdown condition.

For the silty clay slope with the low drawdown rate (R = 0.1 m/day), the shapes of the variation of normalized changes in pore-water pressure (Figure 104) are similar to the high drawdown rate conditions. However, the margins of normalized changes in pore-water pressures below the water level are slightly smaller than for the condition with the high drawdown rate. The phreatic surface at the slope is close to the ground surface for all drawdown ratios (see Figure 102). Therefore, the behaviour of silty clay slopes with a low drawdown rate is still close to the behaviour for fully rapid drawdown, but the FOS will be slightly higher because of some drainage.

Table 21 and Figure 105 show the variation of the factor of safety (FOS) of the silty clay slopes during transient drawdown conditions compared with fully slow and rapid drawdown conditions.

Tab. 21: Variation of FOS for silty clay slope ($k_{sat} = 5.5\times10^{-8}$ m/s)

L / H	FOS			
	Fully Slow Drawdown	Fully Rapid Drawdown	Transient Drawdown R = 1 m/day	Transient Drawdown R = 0.1 m/day
0.0	2.519	2.519	2.519	2.519
0.1	2.356	2.135	2.129	2.139
0.2	2.193	1.911	1.907	1.930
0.3	2.052	1.724	1.723	1.756
0.4	1.952	1.574	1.573	1.618
0.5	1.880	1.449	1.454	1.509
0.6	1.837	1.351	1.361	1.426
0.7	1.820	1.276	1.291	1.367
0.8	1.828	1.223	1.245	1.326
0.9	1.850	1.188	1.216	1.307
1.0	1.888	1.171	1.204	1.301

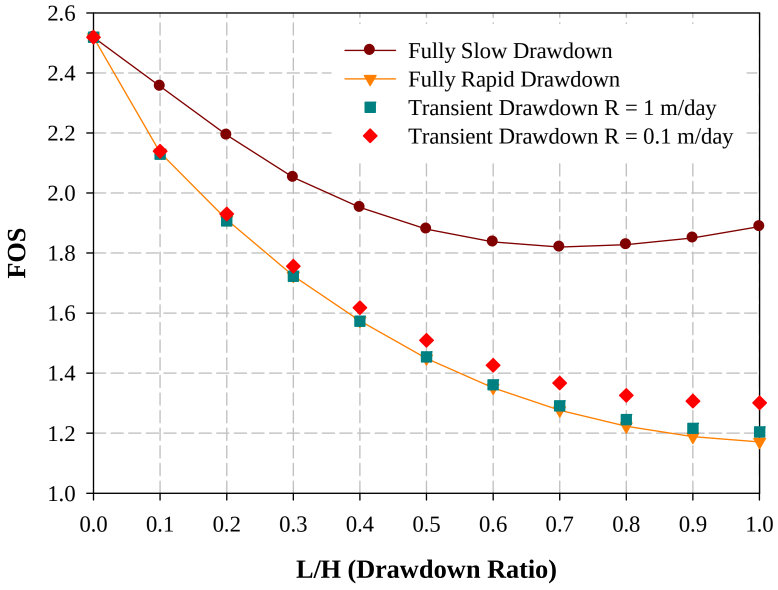

Fig. 105: Change of FOS with drawdown ratio for silty clay slopes

Transient drawdown condition for the sandy clay slopes

The failure mechanisms and the change of degree of saturation of the sandy clay slopes for transient drawdown conditions with saturated hydraulic conductivity $k_{sat} = 3.3\times10^{-6}$ m/s and two different drawdown rates R = 1 and R = 0.1 m/day are illustrated in Figures 106 and 107 respectively.

Figures 108 and 109 illustrate the variations of normalized excess pore pressures with different drawdown ratios (L/H) and drawdown rates (R) during transient drawdown conditions.

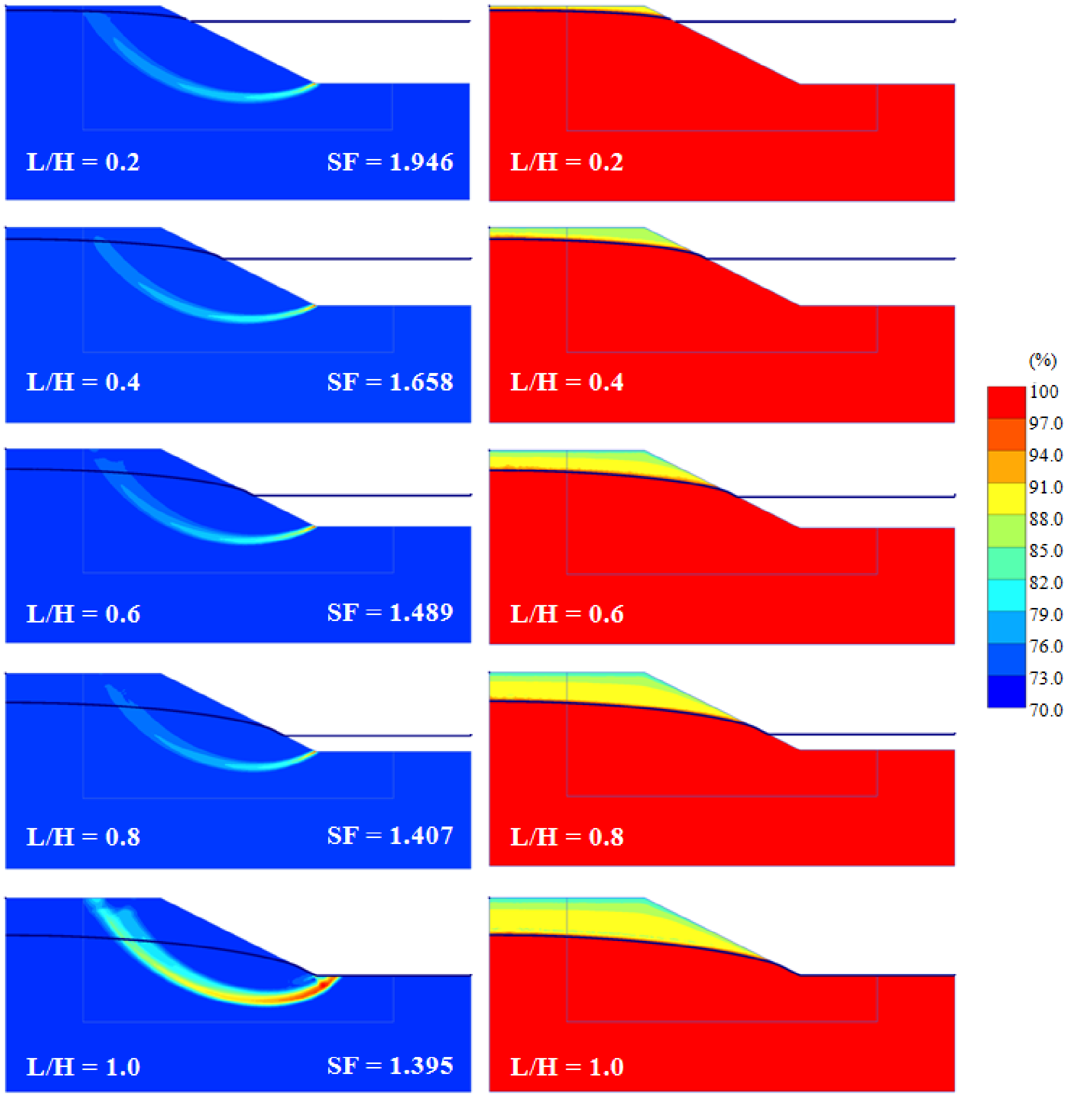

Fig. 106: Failure mechanism and change of degree saturation for sandy clay slopes during transient drawdown conditions (R = 1 m/day)

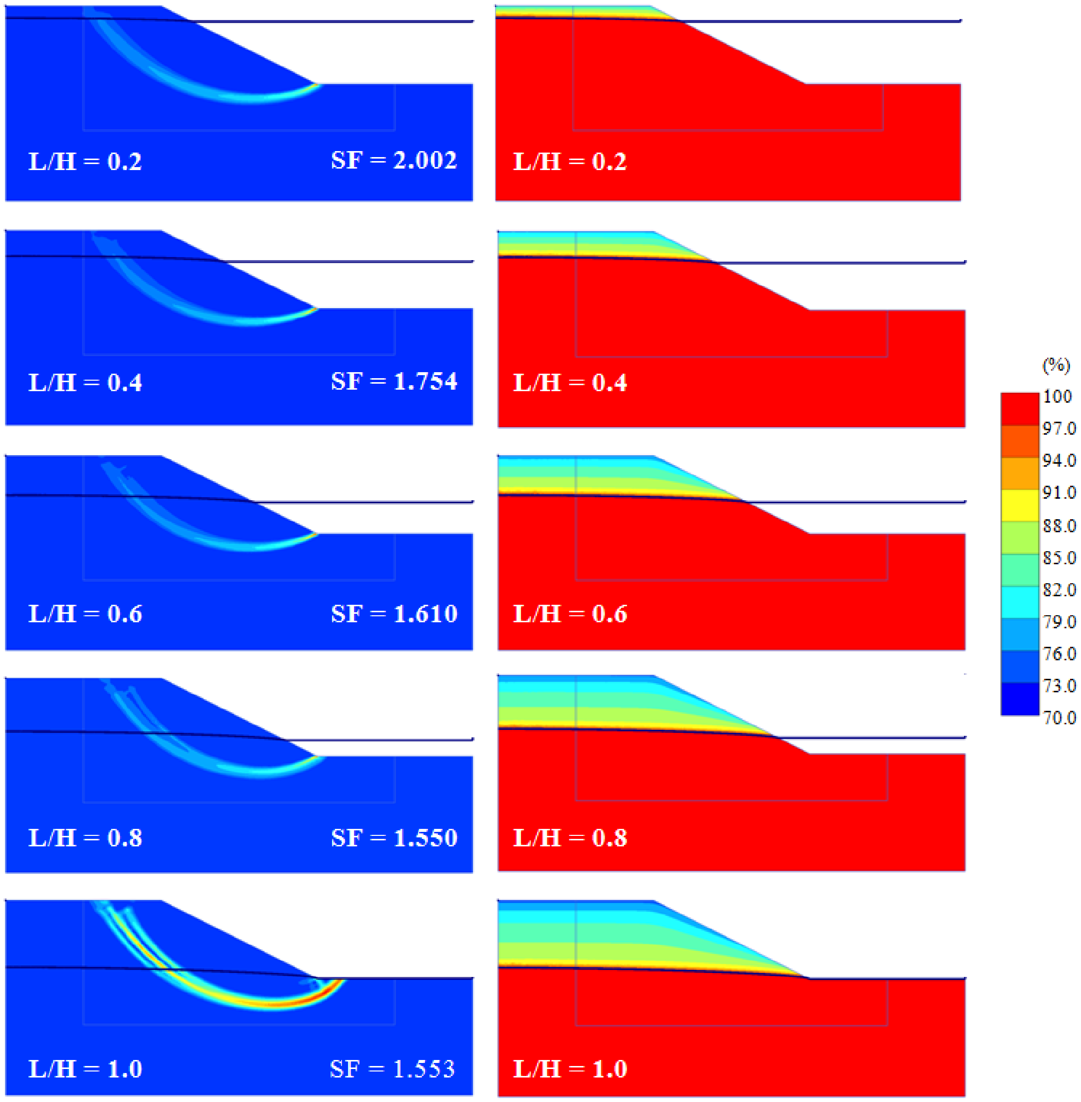

Fig. 107: Failure mechanism and change of degree saturation for sandy clay slopes during transient drawdown conditions (R = 0.1 m/day)

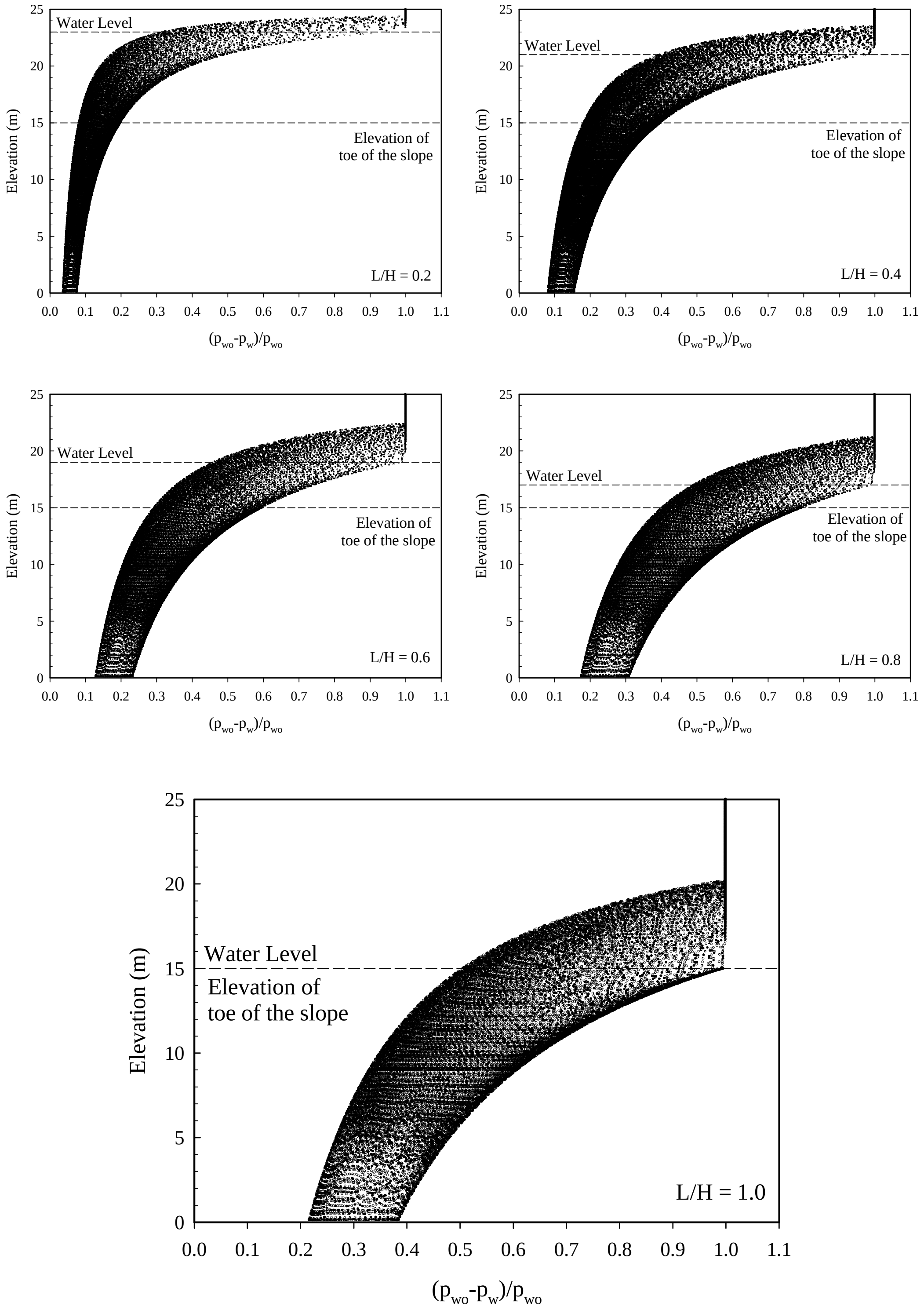

Fig. 108: Variation of normalized changes in pore-water pressure for sandy clay slopes with drawdown rate R = 1 m/day

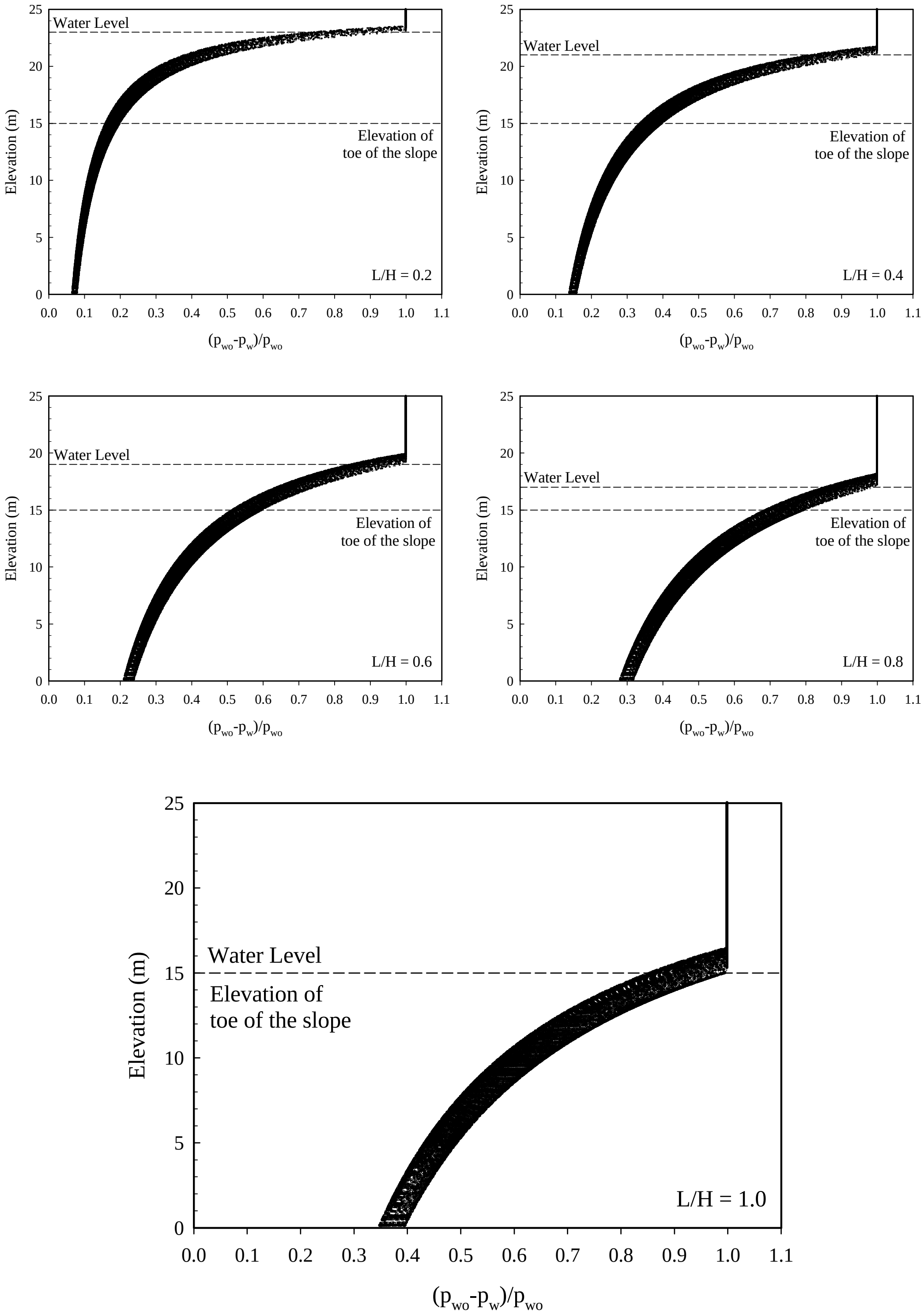

Fig. 109: Variation of normalized changes in pore-water pressure for sandy clay slopes with drawdown rate R = 0.1 m/day

Figure 108 shows the variation of normalized changes in pore-water pressures for sandy clay slopes with high drawdown rate of R = 1 m/day. By comparison with the fully rapid drawdown condition, the margin of normalized changes in pore-water pressure of the sandy clay slope with the high drawdown rate below the water level is reduced almost by half. The positions of the phreatic surface at the slope for all drawdown ratios are above the water level (see Figure 106), but not too close to the ground surface. These conditions illustrate a partial drainage of the slope but the behaviour is still close to the fully rapid drawdown condition. Because of partial drainage occurs the FOS will be higher than for the fully rapid drawdown conditions.

For the sandy clay slope with a low drawdown rate (R = 0.1 m/day), the variation of normalized changes in pore-water pressure (Figure 109) is very similar to the high drawdown rate condition. However, the margins of normalized changes in pore-water pressures are only about 25% compared to the condition with a high drawdown rate. For the low drawdown rate the position of the phreatic surfaces at the slope is almost horizontal for all drawdown ratios (see Figure 107). Consequently, the behaviour of the sandy clay slopes with a low drawdown rate is still close to the fully rapid drawdown condition, because the pore-water pressures are not fully dissipated during drawdown. Therefore, the FOS of the sandy clay slope with low drawdown rate condition will be higher than the fully rapid drawdown condition and lower than the fully slow drawdown condition.

Table 22 and Figure 110 show the variation of the factor of safety (FOS) of the sandy clay slopes during transient drawdown conditions compared with fully slow and rapid drawdown conditions.

Tab. 22: Variation of FOS for sandy clay slope (k_{sat} = 3.3 x 10^{-6} m/s)

L / H	FOS			
	Fully Slow Drawdown	Fully Rapid Drawdown	Transient Drawdown R = 1 m/day	Transient Drawdown R = 0.1 m/day
0.0	2.519	2.519	2.519	2.519
0.1	2.356	2.135	2.145	2.174
0.2	2.193	1.911	1.946	2.002
0.3	2.052	1.724	1.785	1.863
0.4	1.952	1.574	1.658	1.754
0.5	1.880	1.449	1.559	1.671
0.6	1.837	1.351	1.489	1.610
0.7	1.820	1.276	1.438	1.571
0.8	1.828	1.223	1.407	1.550
0.9	1.850	1.188	1.397	1.544
1.0	1.888	1.171	1.395	1.553

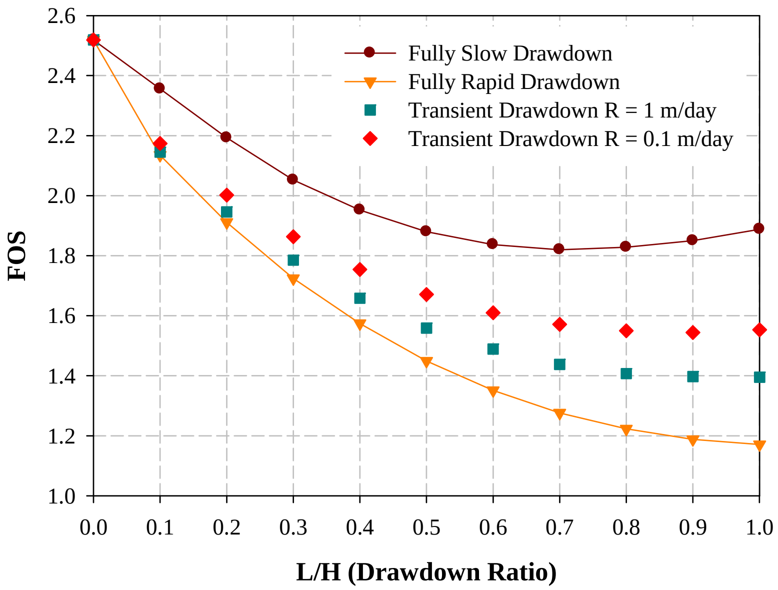

Fig. 110: Change of FOS with drawdown ratio for sandy clay slope

7.2 Summary

The general design practice solutions for two limiting conditions (fully slow and fully rapid drawdown) do not always reflect the field conditions, because they do not consider the hydraulic parameters of soils and the rate and level of drawdown.

In transient drawdown conditions, the combined effects of hydraulic parameters of the soil and the rate and level of the drawdown influence the calculated FOS, which is bound by the limiting conditions (fully slow and rapid drawdown). The finite element method with a fully coupled flow-deformation analysis can be a valuable tool to analyze transient drawdown condition in unsaturated soil slopes. With this analysis, the simultaneous generation of groundwater flow and stress-induced pore-water pressures and their changes with time can be calculated. Hence, the computed FOS are more realistic.

The analysis of the slopes in transient drawdown condition with low hydraulic conductivity such as silty clay slopes (k_{sat} = 5.5×10^{-8} m/s) showed that the drawdown rate (R) has a small influence on the changes in pore-water pressures. During drawdown condition only a small drainage occurs and the behaviour of the slopes is closes to the fully rapid drawdown condition. However the computed FOS's are slightly higher (see Figure 111).

With a rather moderate hydraulic conductivity such as a sandy clay (k_{sat} = 3.3×10^{-6} m/s) the drawdown rate has a significant influence on the changes in pore-water pressures. Although there is a partial drainage during drawdown condition, the behaviour of the slope is still closes to the fully rapid drawdown condition. The computed FOS are higher than the fully rapid drawdown condition but lower than the fully slow drawdown condition (see Figure 111).

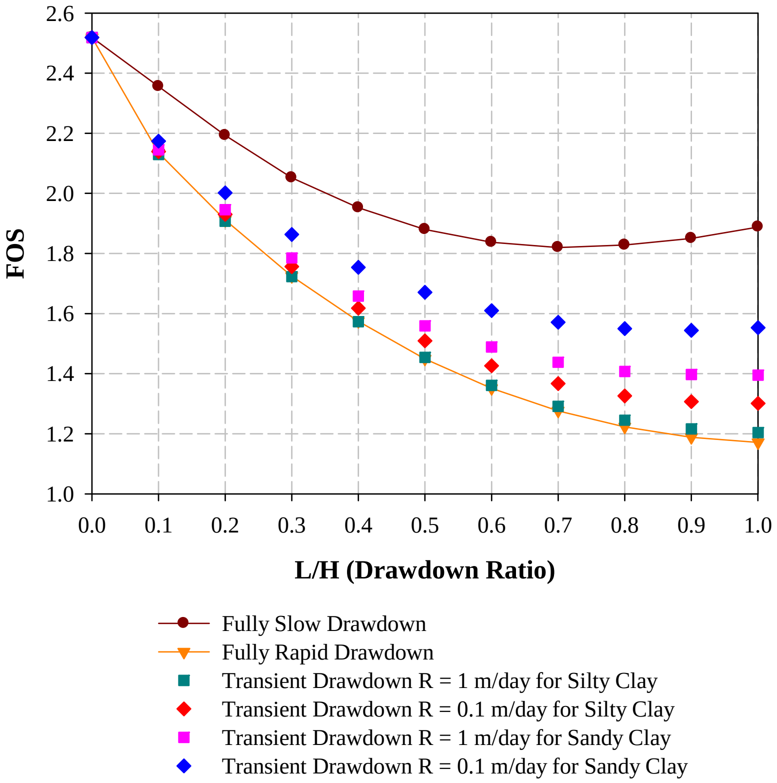

Fig. 111: Change of FOS with drawdown ratio for soil slopes with different hydraulic parameters.

8 Conclusions and further research

8.1 Conclusions

Two approaches of slope stability analyses, one based on limit equilibrium methods and the other based on the finite element method are widely used in practice. The finite element method in combination with a Mohr-Coulomb criterion has been shown to be an efficient tool for analyzing slope stability problems. In contrary to limit equilibrium methods were the shape of the failure mechanism has to be assumed, in the finite element method the failure mechanisms is a result of the analysis.

Three methods of modelling undrained behaviour (Method A, Method B and Method C) in slope stability analysis have been presented by an example of a cutting slope. Method A and B specify undrained behaviour in an effective stress analysis using effective model parameters, whereas the Method C is a total stress analysis with undrained parameters. The computed factor of safety and failure mechanisms of the slope from these methods are similar.

Slope stability analysis considering strain softening with a Multilaminate model has been evaluated by comparing results with three other methods namely reduced strength with the Multilaminate model, change of strength in one step with the Multilaminate model and strength reduction technique with a Mohr Coulomb model. All methods seem to convergence to similar failure mechanisms and factors of safety. The ratio between peak and residual strength in the Multilaminate model with strain softening behaviour is close to the safety factor obtained with the strength reduction technique applying the Mohr Coulomb failure criterion.

Slope stability analyses considering unsaturated soil behaviour have been presented by two examples of unsaturated slopes with and without rain infiltration. The stability of an unsaturated slope will be affected by the distribution of negative pore water pressures (suction). The slope stability increases when the shear strength contributed by matric suction is taken into account. Different hydraulic parameters will generate different distributions of saturation in different soils based on the Soil Water Characteristic Curves (SWCC) for the particular soil. These parameters will effect the FOS of the unsaturated slope with and without rainfall infiltration. The water table location also will influence the factor of safety of the slopes. During the time of rain infiltration suction decreases and thus the FOS of the slope reduces, whereas the reduction is faster for soils with high permeability than for soils with low permeability.

A back analysis of an unsaturated slope subjected to rain infiltration has been presented. The comparison between the back analysis performed with the finite element method and in-situ measurements of a field trial investigating the effect of rainfall infiltration showed good agreement for pore-water pressures and groundwater levels. Small differences are probably caused by cracks and fissures observed in particular up to 1.5 m depth below the ground surface which are not considered in the back analysis.

Slope stability analyses under drawdown condition have been evaluated by an example of a slope with three drawdown conditions namely fully rapid drawdown, fully slow drawdown and transient drawdown. In transient drawdown conditions, the combined effects of hydraulic parameters of the soil and the rate and level of drawdown influence the calculated FOS, which is bound by the limiting conditions (fully slow and rapid drawdown). Generally, the computed FOS in transient conditions with different hydraulic parameters and drawdown rates and level are lower than for a fully slow drawdown condition and higher than for a fully rapid drawdown.

8.2 Further research

In the following recommendations for further research on slope stability analysis employing the finite element method are suggested:

- Investigation the effect of possible stabilization techniques in unsaturated soil slopes subjected to rain infiltration.

- Slope stability analysis using Multilaminate model with strain softening behaviour should be further evaluated against measured data obtained from real slopes with softening material.

- Investigation of the effect of possible stabilization techniques in strain-softening slopes.

- Studies of 3D-slope stability showed that the factor of safety calculated using 3D analysis will always be greater than, or equal to, the factor of safety calculated using 2D analysis (Duncan, 1996). Therefore, 3D-slope analyses are recommended to compare the FOS obtained from 2D-analyses, which are generally considered providing conservative results.

9 Bibliography

Abramson, L., E.; Lee, T., S.; Sharma, S.; Boyce, G., M. (2002)
Slope stability and stabilization methods. Second Edition, John Wiley & Sons, Inc., Canada.

Alkasawneh, W.; Malkawi, A., I., H.; Nusairat, J., H.; Albataineh, N. (2008)
A comparative study of various commercially available programs in slope stability analysis. Computers and Geotechnics, Vol. 35 (3), 428-435.

Alonso, E.; Pinyol, E. (2009)
Slope stability under rapid drawdown conditions A: Italian Workshop on Landslides. "First Italian Workshop on Landslides", Napols, 11-27.

Baker, R.; Frydman, S.; Talesnick, M. (1993)
Slope stability analysis for undrained loading conditions. International Journal of Numerical and Analytical Methods in Geomechanics, Vol. 17 (1), 15-43.

Berilgen, Mehmet M. (2007)
Investigation of stability of slopes under drawdown condition. Computers and Geotechnics, Vol. 34 (2), 81-91

Brinkgreve, R.B.J.; Swolf, W. M.; and Engin, E. (2010)
Plaxis, users manual. The Netherlands.

Cai, F.; Ugai, K. (2004)
Numerical analysis of rainfall effect on slope stability. International Journal of Geomechanics, Vol. 4 (2), ASCE, 69-78.

Cheng, Y., M.; Lansivaara, T.; Wei, W., B. (2007)
Two-dimensional slope stability analysis by limit equilibrium and strength reduction method. Computers and Geotechnics, Vol. 34 (3), 137-150.

Cho, S., E.; Lee, S., R. (2000)
Instability of unsaturated soil slopes due to infiltration. Computers and Geotechnics, Vol. 28 (3), 185-208.

Cho, S., E.; Lee, S., R. (2002)
Evaluation of surficial stability for homogeneous slopes considering rainfall characteristics. Journal of Geotechnical and Geoenvironmental Engineering, Vol. 128 (9), ASCE, 756-763.

Conte, E.; Silvestri, F.; Troncone, A. (2010)
Stability analysis of slopes in soils with strain-softening behaviour. Computers and Geotechnics, Vol. 37 (5), 710-722.

Dawson, E., M.; Roth, W., H. ; Drescher, A. (1999)
Slope stability analysis by strength reduction. Geotechnique, Vol. 49 (6), 835-840.

Duncan, J., M. (1996)
State of the art: Limit equilibrium and finite element analysis of slopes. Journal of Geotechnical Engineering, Vol. 122 (7), 577-596.

Fredlund, D., G. (2000)
The 1999 R.M. Hardy Lecture: The implementation of unsaturated soil mechanics into geotechnical engineering. Canadian Geotechnical Journal, Vol. 37 (5), 963-986.

Fredlund, D., G. (1996)
The emergence of unsaturated soil mechanic. The Fourth Spencer J. Buchanan Lecturer, College Station, Texas, A & M University Press, p.39.

Fredlund, D., G.; Sheng, D.; Zhao, J. (2011)
Estimation of soil suction from the soil-water characteristic curve. Canadian Geotechnical Journal, Vol. 48 (2), 186-198.

Fredlund, D., G.; Xing, A.; Fredlund, M., D.; Barbour, S., L. (1995)
The relationship of the unsaturated soil shear strength to the soil-water characteristic curve. Canadian Geotechnical Journal, Vol. 33 (3), 440-448.

Frydman, S.; Baker, R. (2009)
Theoretical Soil-Water Characteristic Curves based on adsorption, cavitation, and a double porosity model. International Journal of Geomechanics, ASCE, Vol. 9 (6), 250-257.

Galavi, V. (2007)
A Multilaminate Model for structured clay incorporating inherent anisotropy and strain softening, Gruppe Geotechnik Graz, Graz University of Technology, Austria, Heft 32.

Galavi, V.; Schweiger, H., F. (2010)
Nonlocal multilaminate model for strain softening analysis. International Journal of Geomechanics, ASCE, Vol. 10 (1), 30-44.

Gasmo, J. M.; Rahardjo, H.; Leong, E. C. (2000)
Infiltration effects on stability of a residual soil slope. Computers and Geotechnics, Vol. 26 (2), 145-165.

Gavin, K.; Xue, J. (2008)
A simple method to analyze infiltration into unsaturated soil slopes. Computers and Geotechnics, Vol. 35 (2), 223-230.

GEO-SLOPE International (2008)
Stability modelling with Slope/W 2007, An Engineering Methodology, Fourth Edition, Canada.

Griffiths, D., V.; Fenton, G., A. (2004)
Probabilistic slope stability analysis by finite elements. Journal of Geotechnical and Geoenvironmental Engineering, Vol. 130 (5), ASCE, 507-518.

Griffiths, D., V.; Lane, P., A. (1999)
Slope stability analysis by finite elements. Geotechnique, Vol. 49 (3), 387-403.

Griffiths, D., V.; Lu, N. (2005)
Unsaturated slope stability analysis with steady infiltration or evaporation using elasto-plastic finite elements. International Journal of Numerical and Analytical Methods in Geomechanics, Vol. 29 (3), 249-267.

Hammouri, N., A.; Malkawi, A., I., H.; Yamin, M., M., A. (2008)
Stability analysis of slopes using the finite element method and limiting equilibrium approach. Bulletin of Engineering Geology and the Environment, Vol. 67 (4), 471-478.

Huang, M.; Jia, C., Q. (2009)
Strength reduction FEM in stability analysis of soil slopes subjected to transient unsaturated seepage. Computers and Geotechnics, Vol. 36 (1-2), 93-101.

Krahn, J. (2003)
The 2001 R.M. Hardy Lecture: The limits of limit equilibrium analyses. Canadian Geotechnical Journal, Vol. 40 (3), 643-660.

Lane, P., A.; Griffiths, D., V. (2000)
Assesment of stability of slopes under drawdown conditions. Journal of

Geotechnical and Geoenvironmental Engineering, Vol. 126 (5), ASCE, 443-450.

Lu, N.; Griffiths, D., V. (2004)
Profiles of steady-state suction stress in unsaturated soils. Journal of Geotechnical and Geoenvironmental Engineering, Vol. 130 (10), ASCE, 1063-1076.

Lu, N.; Likos, W., J. (2006)
Suction stress characteristic curve for unsaturated soil. Journal of Geotechnical and Geoenvironmental Engineering, Vol. 132 (2), ASCE, 131-142.

Matsui, T.; San, K., C. (1992)
Finite element slope stability analysis by shear strength reduction technique. Soils and Foundation, Vol. 32 (1), 59-70.

Ng, C., W., W.; Pang, Y., W. (2000)
Influence of stress state on soil-water characteristics and slope stability. Journal of Geotechnical and Geoenvironmental Engineering, Vol. 126 (2), ASCE, 157-166.

Ng, C., W., W.; Shi, Q. (1998)
A numerical investigation of the stability of unsaturated soil slopes subjected to transient seepage. Computers and Geotechnics, Vol. 22 (1), 1-28.

Ng, C. W. W.; Springman, S., M.; Alonso, E., E. (2008)
Monitoring the performance of unsaturated soil slopes. Geotechnical and Geological Engineering, Vol. 26 (6), 799-816.

Ng, C. W. W.; Zhan, L., T.; Bao, C., G.; Fredlund, D. G.; Gong, B. W. (2003)
Performance of an unsaturated expansive soil slope subjected to artificial rainfall infiltration. Geotechnique, Vol. 53 (2), 143-157.

Oberg, A. L.; Sällfors, G. (1997)
Determination of shear strength parameters of unsaturated silts and sands based on the water retention curve. ASTM Geotechnical Testing Journal, Vol. 20(1), 40-48.

Rahardjo, H.; Li, X., W.; Toll, D., G.; Leong, E., C. (2001)
The effect of antecedent rainfall on slope stability. Geotechnical and Geological Engineering, Vol. 19 (3-4), 371-399.

Rahardjo, H.; Nio, A., S.; Leong, E., C.; Song, N., Y. (2010)
Effects of groundwater table position and soil properties on stability of slope during rainfall. Journal of Geotechnical and Geoenvironmental Engineering, Vol. 136 (11), ASCE, 1555-1564.

Rahardjo, H.; Ong, T., H.; Rezaur, R., B.; Leong, E., C. (2007)
Factors controlling instability of homogeneous soil slopes under rainfall. Journal of Geotechnical and Geoenvironmental Engineering, Vol. 133 (12), ASCE, 1532-1543.

Troncone, A. (2005)
Numerical analysis of a landslide in soils with strain-softening behaviour. Geotechnique, Vol. 55 (8), 585–596.

US Army Corps of Engineers (2003)
Engineering and Design: Slope stability. Engineering Manual. Department of The Army, US Army Corps of Engineers, Washington DC.

Vanapalli, S. K.; Fredlund, D. G.; Pufahl, D. E.; Clifton, A. W. (1996)
Model for the prediction of shear strength with respect to soil suction. Canadian Geotechnical Journal, Vol. 33 (3), 379-392.

Van Genuchten, M., T., (1980)
A closed-form equation for predicting the hydraulic conductivity of unsaturated soils. Soil Science Society of America Journal, Vol. 44 (5), 892-898.

Van Genuchten, M., T.; Nielsen, D., R. (1985)
On describing and predicting the hydraulic properties of unsaturated soils. Annales Geophysicae, Vol. 3 (5), 615-628.

Wiltafsky Ch. (2003)
A Multilaminate Model for normally consolidated clay, Gruppe Geotechnik Graz, Graz University of Technology, Austria, Heft 18.

Zhan, T., L., T.; Ng, C., W., W. (2004)
Analytical analysis of rainfall infiltration mechanism in unsaturated soils. International Journal of Geomechanics, ASCE, Vol. 4 (4), 273-284.

Zhan, T., L., T.; Ng, C., W., W.; Fredlund, D., G. (2006)
Instrumentation of an unsaturated expansive soil slope. ASTM Geotechnical Testing Journal, Vol. 30 (2), 113-123.

Zhan, T., L., T.; Ng, C., W., W.; Fredlund, D., G. (2007)
Field study of rainfall infiltration into a grassed unsaturated expansive soil slope. Canadian Geotechnical Journal, Vol. 44 (4), 392-408.

Zhang, L., L.; Fredlund, D., G.; Zhang, L., M.; Tang, W., H. (2004)
Numerical study of soil conditions under which matric suction can be maintained. Canadian Geotechnical Journal, Vol. 41 (4), 569-582.

Zhang, G.; Zhang, G., M. (2007)
Simplified method of stability evaluation for strain-softening slopes. Mechanics Research Communications, Vol. 34 (5-6), 444-450.